Recent progress in layered transition metal carbides and/or nitrides (MXenes) and their composites : synthesis and applications

Ng, Vincent Ming Hong; Huang, Hui; Zhou, Kun; Lee, Pooi See; Que, Wenxiu; Xu, Jason Zhichuan; Kong, Ling Bing

2016

Ng, V. M. H., Huang, H., Zhou, K., Lee, P. S., Que, W., Xu, J. Z., & Kong, L. B. (2017). Recent progress in layered transition metal carbides and/or nitrides (MXenes) and their composites : synthesis and applications. Journal of Materials Chemistry A, 5(7), 3039-3068. doi:10.1039/C6TA06772G

https://hdl.handle.net/10356/138806

https://doi.org/10.1039/C6TA06772G

Journal of Materials Chemistry A

Accepted Manuscript

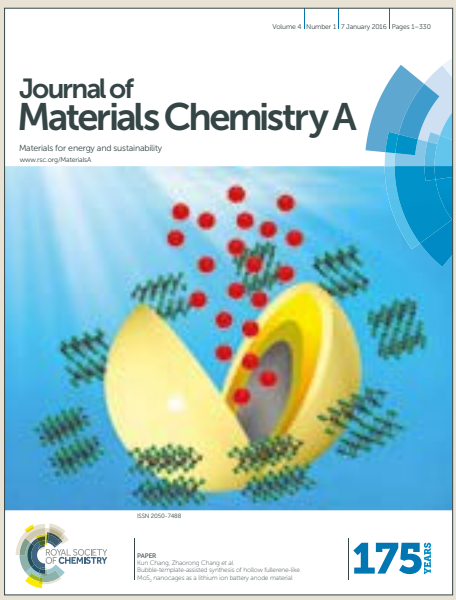

ROYAL SOCIETY OF CHEMISTRY

rsc.li/materials-a

View Article Online
DOI: 10.1039/C6TA06772G

Journal Name

REVIEW

Recent Progress in Layered Transition Metal Carbides and/or Nitrides (MXenes) and their Composites: Synthesis and Applications

Received 00th January 20xx,
Accepted 00th January 20xx

DOI: 10.1039/x0xx00000x

www.rsc.org/

Vincent Ming Hong Ng [a], Hui Huang [b], Kun Zhou [c], Pooi See Lee [a], Wenxiu Que [d,*], Jason Zhichuan Xu [a,*] and Ling Bing Kong [a,*]

Since its inception in 2011, from the inaugural synthesis of multi-layered $Ti_3C_2T_x$ by etching Ti_3AlC_2 with hydrofluoric acid (HF), novel routes with myriad of reducing agents, etchants and intercalants have been explored and added many new members to the two-dimenisonal (2D) material constellation. Despite being endowed with the rare combination of good electronic conductivity and hydrophilicity, their inherent low capacities, for instance, temper their prospect in application for electrodes in energy storage systems. MXene-based composites, however, with probable synergistic effect in agglomeration prevention, facilitating electronic conductivity, improving electrochemical stability, enhancing pseudocapacitance and minimizing the shortcomings of individual components, exceed the previously mentioned capacitance ceiling. In this review, we summarise the development and progress in synthesis of various multi-layered carbides, carbonitrides and nitrides, intercalants, as well as the subesequent processing in order to delaminate them into single- and/or few-layered and modifications to MXene-based composites, focusing on their performances and applications as transparent conductive films, environmental remediation, electromagnetic interference (EMI) absorption and shielding, electrocatalysts, Li-ion batteries (LIBs), supercapacitors and other electrochemical storage systems.

1. Introduction

In 2011, a new two-dimensional (2D) early transition metal carbide, Ti_3C_2, was first synthesized by selectively etching the Al atoms in layered hexagonal (space group $P6_3/mmc$) ternary carbide, Ti_3AlC_2, with the use of aqueous hydrofluoric acid (HF) at room temperature (RT).[1] Ti_3AlC_2 is one of the 70-plus different known ternary carbides and nitrides with general chemical composition $M_{n+1}AX_n$, where M is an early transition metal, A is primarily a group 13 or 14 (i.e. group IIIA or IVA) element, X is C and/or N, and n = 1, 2, or 3.[2] Additionally, $M_{n+1}AX_n$ can also be synthesized with solid solutions of M, A and X atoms, such as $(Mo_2Ti)AlC_2$, $Ti_3(Al_{0.5}Si_{0.5})C_2$ and $Ti_2Al(C_{0.5}N_{0.5})$, respectively, prospectively augmenting the 2D material constellation by quite a large number, when the A layers are selectively extracted, leaving the $M_{n+1}X_n$ layers intact. [3-5]

These layered hexagonal $M_{n+1}AX_n$ phases are composed of two formula units per unit cell, where M layers are nearly closed packed with X atoms filling between the octahedral sites and the $M_{n+1}X_n$ layers are interleaved with layers of A atoms.[6] These laminated structures have anisotropic properties for the M-X bond has an assortment of ionic/covalent/metallic characteristics while the M-A bond is purely metallic in nature. The strong bonds between the layers in $M_{n+1}AX_n$ phases, unlike the weak van der Waals interactions present in other layered materials such as graphite and transition metal dichalcogenides (TMDs), are unsurmountable by mere mechanical exfoliation into 2D layers.[7] However, by exploiting the varied characteristics and relative strengths between M-X and M-A bonds, the relatively weak bound and reactive A layers can be selectively etched with suitable chemical(s) leaving behind the chemically more stable closed packed $M_{n+1}X_nT_x$ layers. T_x refers to surface-terminating functional groups such as oxygen (=O), hydroxyl (–OH) or fluorine (–F) that are attached to the surface M atoms after the etching procedure. The thickness of the $M_{n+1}X_nT_x$ is dependent on the value of n. For example, when n = 1, the layer will consist of a single block of octahedral, when n =2 and 3, there will be two and three blocks, respectively. These new materials have been termed as MXenes in recognition of the loss of A element from the parent $M_{n+1}AX_n$ phase and 2D morphology reminiscent of graphene.

Cumulatively, extensive studies have indicated that there are certain constraints in the synthesis of the parent $M_{n+1}AX_n$

[a] School of Materials Science and Engineering, Nanyang Technological University, 50 Nanyang Avenue, Singapore 639798. Email: xuzc@ntu.edu.sg, elbkong@ntu.edu.sg
[b] Singapore Institute of Manufacturing Technologies (SIMTech), 71 Nanyang Drive, Singapore 638075.
[c] School of Mechanical & Aerospace Engineering, Nanyang Technological University, 50 Nanyang Avenue, Singapore 639798.
[d] Electronic Materials Research Laboratory, School of Electronic and Information Engineering, Xi'an Jiaotong University, Xi'an, P. R. China, Email: wxque@xjtu.edu.cn

Electronic Supplementary Information (ESI) available: [details of any supplementary information available should be included here]. See DOI: 10.1039/x0xx00000x

phases and selective extraction of A element from parent phase. In the synthesis of parent $M_{n+1}AX_n$ phases with Al, the M components are observed to be limited to only Ti, V, Cr, Nb, Ta, Zr and Mo. Selective removal of A element from parent $M_{n+1}AX_n$ phases at elevated temperature is possible however structural transformation and subsequent partial loss of layering are inevitable.[8] High temperature chlorination causes the removal of both M and A components and yields porous carbide derived carbons (CDC) instead.[9]

Although two existing reviews have been dedicated extensively to synthesis and potential applications of MXenes, and a few others on its energy storage applications, none covers its progress as composite materials.[10-13] In this review, the advancement of MXene and its composites, encompassing both theoretical and experimental studies of relevance to their synthesis, properties and potential applications in the field of transparent conductors, environmental remediation and energy storage, will be detailed and discussed.

2. Synthesis and characterizations

Since the pioneering synthesis of multi-layered $Ti_3C_2T_x$ through HF etching at RT, much work has been channelled towards discovering novel routes to preparing existing and new MXenes. To date, even with the myriad of synthesis conditions and reagents identified, fluoride-based compounds remain an incumbent component to effective preparation of these 2D transition metal carbides. Intuitively, the synthesis route adopted will be influential over their surface chemistries and consequential behaviour. Characterizations of these materials have shed light on some of their properties and prompted further investigations, studies, and processing to optimally exploit the advantages of MXenes, especially so in the case of composites.

2.1 Multi-layered stacked MXenes

The inaugural synthesis of multi-layered $Ti_3C_2T_x$ was reported by Naguib *et al.* Ti_3AlC_2 powders, prepared by using a typical route of heating a pre-ball milled mixture of Ti_2AlC and TiC (with a molar ratio of 1:1) at 1350 °C for 2 h in argon (Ar), was immersed and kept under stirring in a 50 % concentrated HF solution at RT for 2 h, followed by filtration to separate residue from the supernatant and repeated washing of the residue with deionized (DI) water.[1] This simple selective etching of the parent $M_{n+1}AX_n$ phases with Al was then successfully extended and yielded multi-layered Ti_2CT_x, $Ta_4C_3T_x$, $(V_{0.5}Cr_{0.5})_3C_2T_x$, $(Ti_{0.5}Nb_{0.5})_2CT_x$, $Ti_3CN_xT_x$, Nb_2CT_x, V_2CT_x, $Nb_4C_3T_x$, $Mo_2TiC_2T_x$ (Fig. 1c-g), $Mo_2Ti_2C_3T_x$, $Cr_2TiC_2T_x$ and $(Nb_{0.8}Ti_{0.2})_4C_3T_x$.[14-18] This preferential etching of the M-A bond in $M_{n+1}AX_n$ phases with Al may be summarized as:

$$M_{n+1}AlX_n + 3HF \rightarrow M_{n+1}X_n + AlF_3 + 1.5H_2 \quad (1)$$

$$M_{n+1}X_n + 2H_2O \rightarrow M_{n+1}X_n(OH)_2 + H_2 \quad (2)$$

$$M_{n+1}X_n + 2HF \rightarrow M_{n+1}X_nF_2 + H_2 \quad (3)$$

Eqs (2) and (3) indicate the surface terminations by a combination of –OH and –F as aqueous etching of Al do not result in bare M layers.[1] Meshkian *et al.* demonstrated that this selective etching by HF can be applicable beyond parent

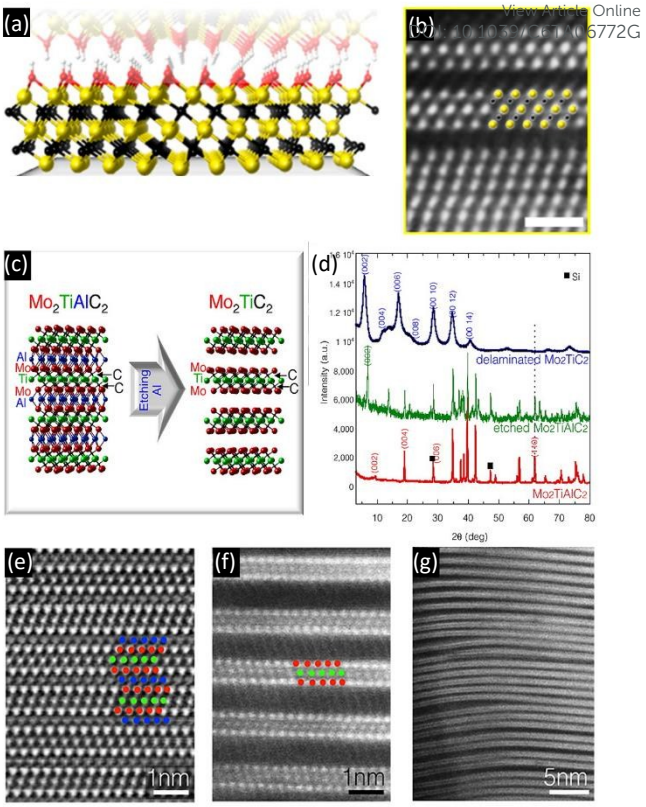

Fig. 1 (a) Schematic for the structure of –OH-terminated Ti_3C_2 after selective etching of Ti_3AlC_2; yellow, black, red and white circles represent Ti, C, O and H atoms, respectively. (b) STEM image of the first two Ti3C2Tx layers after applying Wiener filter; scale bar is equivalent to 1 nm, atoms are shown with the same colors as (a) [reprinted with permission from ref. 25. Copyright 2014 American Chemical Society]. (c) Schematic for the structures of parent Mo_2TiAlC_2 phase and exfoliated HF-etched $Mo_2TiC_2T_x$ phase, respectively; red, green, blue and black circles represent Mo, Ti, Al and C atoms, respectively. (d) XRD patterns of Mo_2TiAlC_2 (red), HF-etched $Mo_2TiC_2T_x$ (green) and delaminated HF-etched $Mo_2TiC_2T_x$ (blue). In the delaminated sample, only *c*-direction peaks, (*00l*) *peaks,* are visible, corresponding to a *c lattice parameter of 30.44 Å*; the (*110*) peak is no longer observed, indicating loss of order in non-basal directions. (e and f) HRSTEM of Mo_2TiAlC_2 and $Mo_2TiC_2T_x$, respectively. Atoms are shown with the same colors as (c). Atomic ordering is verified by EDX mapping. No Al was observed in EDX of $Mo_2TiC_2T_x$. (g) Low magnification TEM image of layered structure throughout the sample of exfoliated HF-etched $Mo_2TiC_2T_x$ [reprinted with permission from ref. 17. Copyright 2015 American Chemical Society].

$M_{n+1}AX_n$ phases with Al, as the Mo_2CT_x layers were formed by HF-etching of Ga in Mo_2Ga_2C.[19] Interestingly, Zhou *et al.* recently managed to synthesize the first layered $Zr_3C_2T_x$ by extending this HF-etching protocol to $Zr_3Al_3C_5$, an alternative layered ternary and quaternary transition metal carbide beyond the $M_{n+1}AX_n$ phases.[20]

Notably, essential etching conditions such as HF concentration, duration of immersion and temperature necessary to completely convert various parent $M_{n+1}AX_n$ phases into multi-layered $M_{n+1}X_nT_x$ expectantly vary widely.[15, 21, 22] For instance the very conditions that yield $Ti_3C_2T_x$ from Ti_3AlC_2 (50 % HF, 2 h, RT) completely dissolve Ti_2AlC. The less stable (lower n value in $M_{n+1}AlX_n$) Ti_2CT_x is instead obtained by immersing

View Article Online
DOI: 10.1039/C4TA05775E

Ti_2AlC in a 10 % concentration HF at RT for 2h. The divergences in M-A bond energies from Ti_2AlC (ca. 0.98 eV) to Nb_2AlC (ca. 1.21 eV) result in the longer etching duration (ca. 90 h) and higher HF concentration (50 % HF, RT), in order to eliminate Al from Nb_2AlC than that from Ti_2AlC.[14, 15, 23] Precariously, complete dissolution or recrystallization of $M_{n+1}X_nT_x$ layers may occur under excessive heating.[14, 24] As smaller particle sizes of the parent $M_{n+1}AX_n$ can effectively reduce the required etching duration and/or HF concentration, the as-synthesized $M_{n+1}AX_n$ powders are usually subjected to attrition or ball milling and/or sieved prior to chemical exfoliation.

Halim *et al.* introduced a less hazardous and milder etchant, i.e., 1 M ammonium bifluoride (NH_4HF_2) solution at RT albeit longer immersion duration, which could concomitantly intercalate ammonium species such as $–NH_3$ and $–NH_4^+$ and effectively etch the Al layers in epitaxial Ti_3AlC_2 films (Fig. 1a-b).[25] Such observation of spontaneous intercalation of cations (Li^+, Na^+, Mg^{2+}, K^+, NH_4^+ and Al^{3+}) in between $Ti_3C_2T_x$ layers was also reported by Mashtalir *et al.*, with implications that were far-reaching and influential in the later development of delaminating stacked MXenes (to be discussed under Section 2.2. Single/ Few-layered MXenes), preparation of various MXene composites (to be discussed under Section 2.3. MXene-based Composites) and potential applications (to be discussed under Chapter 3. Properties and Applications) .[26] Feng *et al.* detailed the influence of temperature and etching duration for the synthesis of $Ti_3C_2T_x$ in 1 M of various bifluoride solution (e.g., $NaHF_2$, KHF_2, or NH_4HF_2). The minimum etching duration for the onset of exfoliating Ti_3AlC_2 in 1 M of bifluoride solution at 60 °C

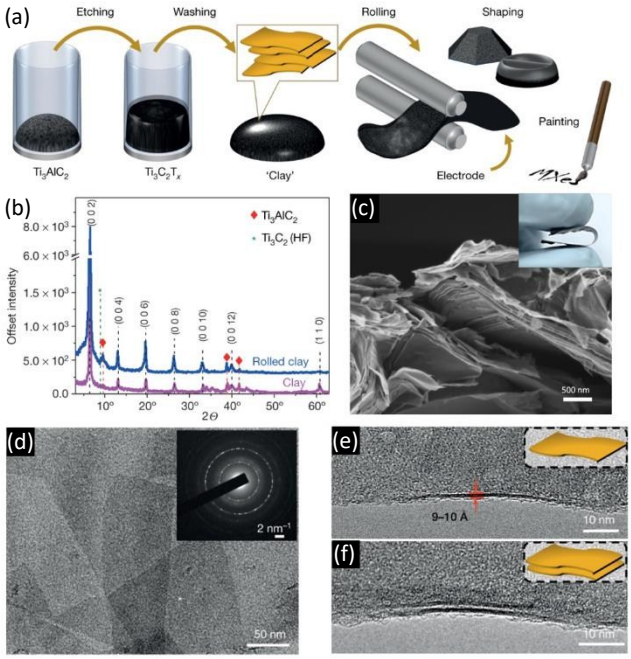

Fig. 2 (a) Schematic for $Ti_3C_2T_x$ 'clay' synthesis by HCl/LiF etching and preparation into free-standing and desired shape electrode. (b) XRD plots of Ti_3AlC_2 and $Ti_3C_2T_x$. (c) SEM image of cross-section of rolled $Ti_3C_2T_x$. TEM images of (d) several flakes of $Ti_3C_2T_x$ with lateral sizes up to a few hundred nanometres, (e) single-layered $Ti_3C_2T_x$, and (f) double-layered $Ti_3C_2T_x$ [reprinted with permission from ref. 30. Copyright 2014 Nature Publishing Group].

was observed to be 8 h. Based on the existence of corresponding by-products ($(NH_4)_3AlF_6$, NH_4AlF_4 and $AlF_3.3H_2O$ in a ratio of 10: 1: 1 for reaction with NH_4HF_2), probable reaction mechanism between Ti_3AlC_2 and bifluoride etchant solution has been proposed.[27]

Wang *et al.* reported a novel hydrothermal synthesis of multi-layered $Ti_3C_2T_x$ by using only Ti_3AlC_2 and NH_4F, where the influence of reactants' ratio, reaction duration and temperature on the yield of $Ti_3C_2T_x$ were detailed. The optimal conditions to produce multi-layered $Ti_3C_2T_x$ via this hydrothermal synthesis route was established to maintain the reaction mixture, with 5.0 g of NH_4F and 0.5 g of Ti_3AlC_2 in 60 mL of DI water, isothermally at 150 °C for 24 h.[28]

Xie *et al.* attempted a fluoride-free reaction via immersing Ti_3AlC_2 in a solution of 1 M sodium hydroxide (NaOH) at 80 °C for 100 h, followed by a hydrothermal treatment in 1 M H_2SO_4 at 80 °C for 2 h. However, it was only partially successful with merely the surface Al, but not bulk, leached from parent Ti_3AlC_2 phase.[29]

Ghidiu *et al.* then introduced another high-yield but safer alternative synthesis route to multi-layered $Ti_3C_2T_x$ by immersing Ti_3AlC_2 powders in a milder etchant solution of 6 M hydrochloric acid (HCl) with certain amount of lithium fluoride (LiF) under constant stirring at 35 °C for 24 h (Fig. 2a-f).[30] Interestingly, a clay-like paste of $Ti_3C_2T_x$ with intercalated water and ions was collected at the after repeated washing with DI water, which could be conveniently shaped to desired forms or rolled to produce flexible, free-standing films (Fig. 2c Inset) in lieu of the tedious sequence of procedures for HF-etched samples as reported elsewhere.[31] To varying degree of success, other fluoride salts, such as sodium fluoride (NaF), potassium fluoride (KF), caesium fluoride (CsF), tetrabutylammonium fluoride, calcium fluoride (CaF_2), could be added in place of LiF into either HCl or sulphuric acid (H_2SO_4) to prepare the etchant solution. It is highly conceivable that a delicate balance of etching conditions for different combinations with as mentioned acid and salt, can potentially bring about a myriad of applicable multi-layered early transition metal carbide compositions and properties, due to modified surface chemistries and diverse pre-intercalated ions. This one-step method has been successfully applied to produce multi-layered Nb_2CT_x, Ti_2CT_x, $Cr_2TiC_2T_x$, $Mo_2TiC_2T_x$, $Mo_2Ti_2C_3T_x$, Mo_2CT_x and $(Nb_{0.8}Zr_{0.2})4C_3T_x$ as well.[17, 18, 30, 32]

Although selective etching with aqueous acid solutions at RT has capably used to produce various carbide and carbonitride MXenes, nitride MXenes such as $Ti_4N_3T_x$ remain hitherto elusive as nanosheets of Ti_4AlN_3 are collected instead after immersion in HF solution at RT.[33] Two factors have been conjectured for the above phenomenon. Firstly, more energy may be necessary for extraction of the strongly-bound Al from $Ti_{n+1}AlN_n$ than from $Ti_{n+1}AlC_n$ as indicated by the higher formation energies of $Ti_{n+1}N_n$ than that of $Ti_{n+1}C_n$. Secondly, $Ti_{n+1}N_n$ is less stable as compared with $Ti_{n+1}C_n$ as suggested by the lower calculated cohesive energies of $Ti_{n+1}N_n$, so that the as-prepared $Ti_{n+1}N_n$ could have probably been dissolved in concentrated HF solution.[10, 34] Urbankowski *et al.* reported an ingenious synthesis of multi-layered $Ti_4N_3T_x$ by thermally treating a

mixture with equal mass of Ti_4AlN_3 powders (> 37 µm) and fluoride salt at 550 °C for 0.5 h in Ar at identical ramping and cooling rate at 10 °C/min.[35] In order to proceed at lower temperature, the ternary eutectic composition in this salt system, which consisted of 59 wt. % KF, 29 wt. % LiF and 12 wt. % NaF, was purposefully selected.[36]

Expectantly, some differences were observed between the different preparation routes (using HF or solution of HCl with LiF). For instance, accordion-like $Ti_3C_2T_x$ samples are obtained from HF treatment, whereas laterally larger flakes of $Ti_3C_2T_x$ with negligible nanoscale defects are yielded by using HCl plus LiF.[30]

A complete transformation from $M_{n+1}AX_n$ phases to multi-layered $M_{n+1}X_nT_x$ could be identified by the remnant (*000l*) X-ray diffraction (XRD) peaks, while all other peaks are weakened or vanish. Evidence of small quantity of unreacted Ti_3AlC_2 has been picked up by XRD, in addition to the shift in (*0002*) peak to lower angles, a consequence of the crystal structure parameter that is directly proportional to the distance between individual MXene layers, with *c* lattice parameter of ca. 25 Å, for the HCl/LiF-derived multi-layered $Ti_3C_2T_x$ as compared with the HF-etched counterpart (*c* lattice parameter of ca. 20 Å).[37] A number of caveats that concern the validity of quantifying unreacted $M_{n+1}AX_n$ phases for XRD intensities tend to fade with increased degree of exfoliation and coexistence of $M_{n+1}AX_n$ phase peaks with $M_{n+1}X_nT_x$ (*000l*) peaks.[10] Correspondingly, exfoliated $Ti_3C_2T_x$ stacks by etching Ti_3AlC_2 at 35 °C for 24 h with 6 M HCl with LiF have persistent $M_{n+1}AX_n$ phase peaks in the XRD patterns, even though they readily are delaminated upon sonication.[30]

X-ray photoelectron spectroscopy (XPS) characterizations are generally able to identify the presence of negatively-charged =O, –OH and –F terminations, indicative of $M_{n+1}X_n$ surfaces having a fixed net positive charge, as an overall neutrality has to be maintained.[31, 38] In fact, the distribution of these surface terminations (Fig. 3a) are dependent on parameters such as the number of layers, the identity of M and X element and so on. For instance, in $Ti_3C_2T_x$, Ti_2CT_x and Ti_3CNT_x, with varying number of layers, n, or X element, the proportion of –F terminations remain invariant while the –O to –OH ratio increases as n is increased. Conversely for Nb_2CT_x and $Nb_4C_3T_x$, the –O to –OH ratio decreases as n is increased.[38]

Energy-dispersive X-ray spectroscopy (EDS) experiments have been employed to quantify their proportions, although EDS is unable to differentiate –O and –OH, because various factors, such as the presence of adsorbed water and etching by-products, could complicate the signal collection.[1, 30]

Nuclear magnetic resonance (NMR) spectroscopy, with high sensitivity towards ^1H and ^{19}F nuclei, has been employed in two recent studies to determine sample compositions with increased confidence and to provide insights to surface functionalisation of V_2CT_x and $Ti_3C_2T_x$ respectively.[37, 39] In the study of HF-etched V_2CT_x, Harris *et al.* through ^1H NMR experiments distinguished that –OH groups are directly bonded to V_2CT_x, with a layer of -H (from H_2O) bonded to the –OH surface; while ^{19}F NMR experiments evidently indicated that the –F groups are indeed directly bonded to V_2CT_x surfaces.[39] Hope *et al.* reaffirmed direct connection of both the –OH and –F

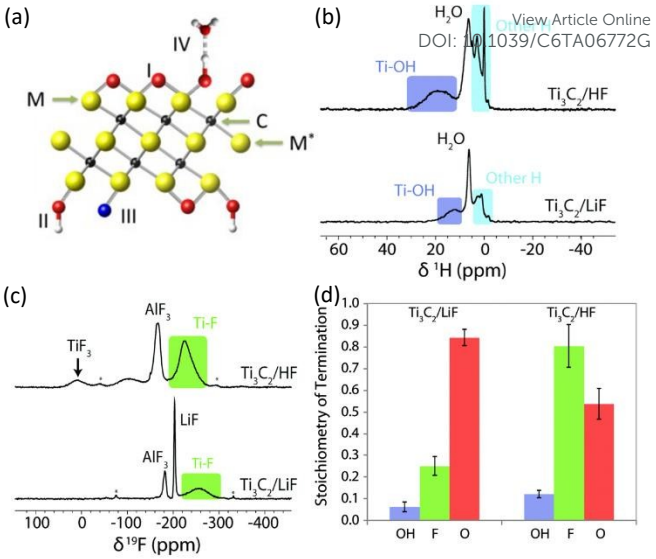

Fig. 3 (a) Side view schematic of a $M_3X_2T_x$ structure showing various M atoms and their terminations. I refers to a M atom bonded to an O atom; II, to OH; III, to a M atom directly bonded to a F-atom; IV, to an M atom bonded to OH, that, in turn, is strongly bonded to a H_2O molecule; M atoms only bonded to C atoms are designated, M^*. Yellow, black, red, white and blue circles (not to scale) represent M, X, O, H and F atoms, respectively [reprinted with permission from ref. 38. Copyright 2016 Elsevier]. (b) ^1H NMR (11.7 T) spectra of HF and HCl/LiF etched $Ti_3C_2T_x$ recorded at 60 kHz MAS. (c) ^{19}F NMR (11.7 T) spectra of HF and HCl/LiF etched $Ti_3C_2T_x$ recorded at 60 kHz MAS. (d) Graphical comparison of the differences in composition of the $Ti_3C_2T_x$ surface functional groups when synthesized by HF and HCl/LiF etching respectively [reprinted with permission from ref. 37. Copyright 2016 the Owner Societies].

groups to $Ti_3C_2T_x$ surfaces. Furthermore, quantitative NMR experiments demonstrated that majority of the surface terminations are present as an intimate mixture of –O and –F, while –OH is in the minority. More importantly, it is established that the proportion of the surface terminations is highly sensitive to the synthesis route adopted (Fig. 3b-c). For example, there are about fourfold of –F termination in HF-etched $Ti_3C_2T_x$ as compared with that in the HCl/LiF-prepared $Ti_3C_2T_x$ (Fig. 3d).[37]

These results are significant because they highlight useful strategies towards manipulating morphologies and surface chemistries; choice of etchant solution, etchant concentration, temperature and duration of immersion. For electronic and optical applications, where defect-free and large sheets are more desirable, the use of HCl/LiF etchant solution may be more preferential to HF solution. Conversely, for energy storage and catalysis applications, where higher ion accessibility and edge effects may be more valued, the route with HF solution which produces defective and nanoporous/pitted flakes may be of more relevance. Evidently, more work is needed to develop a fluoride-free MXene synthesis protocol as well.

2.2 Single/Few-layered MXenes

With the strong M-A bonds to be replaced with weak bonds, such as hydrogen and van der Waals forces, intercalation and delamination of multi-layered stacked MXenes into single or

View Article Online
DOI: 10.1039/C6TA06772G

few layers were possible. Advantageously, the as-synthesized multi-layered $Ti_3C_2T_x$ and Mo_2CT_x from the HCl/LiF etchant solution route as initially proposed by Ghidiu *et al.*, can be fully and easily delaminated by mere sonication in water.[30, 32] This significantly effective delamination have been attributed to intercalated water and possibly cations between the multi-layered MXenes acting as spacer and lubricant that facilitated shearing. It is noted that although etching Ti_3AlC_2 at higher temperature for longer duration (40 °C for 45 h) yields $Ti_3C_2T_x$ with lower Al content as verified by EDS, the ease of delamination and dispersion by mere sonicating are not as readily as that of $Ti_3C_2T_x$ 'clay' obtained under reaction conditions of 35 °C for 24 h.[30] Zhang *et al.* observed a larger *c* lattice parameter of ca. 31 Å and a significant increase in the delamination ratio of HCl-LiF etched $Ti_3C_2T_x$ from 6.5 % to 29.2 % after 1 h of sonication, which can be achieved by prior washing the exfoliated products with ethanol instead of DI water. It was suggested that ethanol could have acted as a co-intercalant, together with impurity ions, which improved the yield of the delaminated HCl-LiF etched $Ti_3C_2T_x$.[40]

Shahzad *et al.* presented a modified procedure with an increased molar ratio of LiF to Ti_3AlC_2 of 7.5:1 (instead of 5:1), to have more Li^+ ions available for intercalation and thus double the molar ratio of HCl to LiF to facilitate the etching of aluminium. Consequently, while all other aspects of the procedure (35 °C for 24 h) remained identical to that reported by Ghidiu *et al.*, $Ti_3C_2T_x$ could be delaminated without sonication.[41] Noticeably, using a more concentrated HCl of 9 M (instead of 6 M) increased the concentration of delaminated $Ti_3C_2T_x$ further, as more protons (H^+) were available to exchange with Li^+.

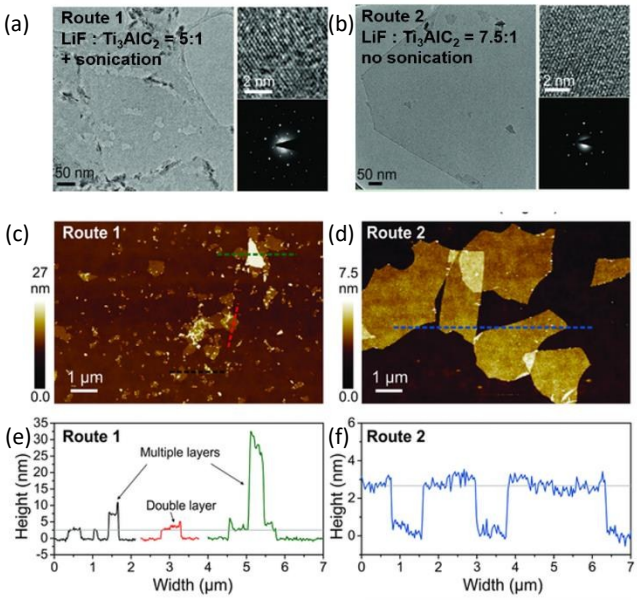

Fig. 4 TEM images of $Ti_3C_2T_x$ flakes produced by using: (a) Route 1 (ratio of LiF to Ti_3AlC_2 is 5:1), and (b) Route 2 (ratio of LiF to Ti_3AlC_2 is 7.5:1), respectively. Small panels in (a) and (b) show HRTEM images and SAED patterns of monolayer 2D crystals of $Ti_3C_2T_x$. AFM images of the $Ti_3C_2T_x$ flakes deposited on Si/SiO_2: (c) Route 1, and (d) Route 2. (e) AFM height profiles measured along the dashed lines in (c). The colors of the height profiles in (e) correspond to the colors of the dashed lines in (c). (f) AFM height profile measured along the dashed line in (d) [reprinted with permission from ref. 42. Copyright 2016 John Wiley & Sons, Inc.].

Lipatov *et al.* evaluated the quality of $Ti_3C_2T_x$ flakes synthesized with different molar ratios of LiF to Ti_3AlC_2 (5:1 and 7.5:1) in 6 M HCl solution at 35 °C for 24 h.[42] Exfoliated $Ti_3C_2T_x$ flakes, with molar ratio of LiF to Ti_3AlC_2 to be 5:1, are observed to be 200–500 nm in diameter, have uneven edges decorated with TiO_2 nanoparticles and numerous pin holes (Fig. 4a), whereas exfoliated $Ti_3C_2T_x$ flakes, with molar ratio of LiF to Ti_3AlC_2 to be 7.5:1, are 4–15 μm laterally, have well-defined and clean edges and no visible pin holes (Fig. 4b) under high resolution transmission electron microscopy (HRTEM). Expectedly, the larger exfoliated $Ti_3C_2T_x$ flakes are mechanically more robust (coarse shiny flakes after grinding) than smaller ones (fine black powders after grinding). Exfoliated $Ti_3C_2T_x$ flakes, with molar ratio of LiF to Ti_3AlC_2 to be 5:1, are less ordered and have varied thicknesses (Fig.4 e), in accordance to the XRD pattern with only (001) reflection and some remnant peaks of the parent $M_{n+1}AX_n$ phase (not exfoliated) and atomic force microscopy (AFM) height profiles. Exfoliated $Ti_3C_2T_x$ flakes, using 7.5:1 molar ratio of LiF to Ti_3AlC_2, are more orderly stacked, with a uniform height of ca. 2.7 nm (single layer with surface adsorbates) (Fig. 4f) as indicated by the series of (*00l*) XRD peaks and AFM height profiles measurement.

Unfortunately, to date, only Ti_3C_2Tx and Mo_2CT_x have been reported to demonstrate concurrent delamination by mere HCl/LiF etching of parent $M_{n+1}AX_n$ phases. Therefore, much more works are necessary to validate if this method can be extended to other MXenes. Attempts for hydrate HF-etched multi-layered $Ti_3C_2T_x$ and Mo_2CT_x to replicate the above results have previously been futile, necessitating the consideration of other intercalants.[30] Importantly, Ghidiu *et al.* experimentally investigated cation substitutions and related their effect on interlayer spacing of HF-etched multi-layered $Ti_3C_2T_x$. It was noted that only when intercalant source, LiCl, was present as part of the etchant solution—rather than as a later addition—can the Li^+ ions and a dynamic layer of H_2O lead to greater structural ordering in the HF-etched multi-layered $Ti_3C_2T_x$ (higher crystallinity as evidenced by the sharp (*002*) XRD peak), which demonstrated clay-like (hydrated) behaviour. As evidenced by XRD pattern, a discontinuous structural expansion in the direction normal to the basal plane of $Ti_3C_2T_x$ as H_2O molecules intercalate, and variance of intercalated cations (with different hydration enthalpy) expectedly cause quite different structural changes in response to relative humidity.[43]

Although only weak residual forces hold and prevent HF-etched multi-layered MXenes from readily separation into individual layers (hence the accordion-like morphologies), a sonication procedure without preceding intercalation of species between the layers can only result in low yield of single/few-layered MXenes. This was illustrated by the pioneering work by Naguib *et al.*, where accordion-like HF-etched $Ti_3C_2T_x$ was exfoliated upon sonication in methanol for 300 s, which however resulted in low yield of $Ti_3C_2T_x$ nanosheets and scrolls, approximately ten-layer thick and even lower yield of single-layer $Ti_3C_2T_x$.[1]

View Article Online
DOI: 10.1039/C6TA06772G

Mashtalir *et al.* reported the first high yield delamination of accordion-like $Ti_3C_2T_x$ into a mixture of narrow sized distributed single and few-layered $Ti_3C_2T_x$ by intercalation of dimethyl sulphoxide (DMSO) between the multi-layered $Ti_3C_2T_x$ at RT for 18 h under constant stirring, followed by sonication in DI water for 6 h.[31] Other organic intercalants such as thiophene, ethanol, acetone, tetrahydrofuran, formaldehyde, chloroform, toluene and hexane, were found to be unsuitable with the exceptions of hydrazine monohydrate (HM), $N_2H_4.H_2O$, dissolved in *N*,*N*-dimethylformamide (DMF) and urea as evident by the observed shift in major XRD peaks towards lower angles. This same group in a later study utilized inelastic neutron scattering (INS) analysis, highly sensitive to ^1H atom, to characterize pristine and HM intercalated HF-etched multi-layered $Ti_3C_2T_x$. It was concluded that HM intercalation into $Ti_3C_2T_x$ led to substantial reduction of water content, as well as the quantity of –OH and –F terminations.[44] However, the prospect of intercalating DMSO is severely limited by its exclusive effectiveness towards delaminating $Ti_3C_2T_x$, probable difficulty with thorough removal of high boiling point solvents used. Furthermore, lamellar thickness can be undesirably increased by remnant DMSO molecules, which joined the delaminated sheets together. Till date, the exact mechanism to explain how and why DMSO only interact with multi-layered $Ti_3C_2T_x$ remains unclear.

Naguib *et al.* introduced another simple and scalable approach towards delamination of HF-etched multi-layered Ti_3CNT_x, V_2CT_x and Nb_2CT_x via intercalation of relatively large basic organic molecules such as tetrabutylammonium hydroxide (TBAOH), choline hydroxide or *n*-butylanime at RT over some duration, followed by mechanical agitation (shaking or sonication) (Fig. 5c-d).[45] The surface chemistry of these MXenes was concomitantly altered, since most of the –F terminations were eliminated. Similarly, by using TBAOH as the intercalant, with the aid of sonication, Urbankowski *et al.* managed to delaminate multi-layered $Ti_4N_3T_x$ into a mixture of single- and few-layered sheets (Fig. 5a-b).[35]

Mashtalir *et al.*, on the other hand, delaminated HF-etched multi-layered Nb_2CT_x by first intercalating isopropylanime (i-PrA) between the layers in DI water at RT for 18 h and then mildly sonicating in deaerated DI water. The HF-etched multi-layered Nb_2CT_x, which is negatively charged at the surface and acidic, is expectedly intercalated with ammonium cation ($R\text{-}NH_3^+$) in i-PrA dissolved in water, presumably due to the electrostatic forces.[26, 46] Increase in efficiency of delamination of Nb_2CT_x layers is anticipated as i-PrA molecules, having three alkyl groups, are sufficiently small to overcome the steric hindrance, so as to push the Nb_2CT_x layers apart, thus further weakening the interlayer interactions. When applying to Ti_3CT_x and $Nb_4C_3T_x$, it is noteworthy that, prior to sonication, multi-layered Ti_3CT_x has been already found to partially delaminate after 18 h; which is in contrast to the lengthy (up to two weeks) period of immersion required for $Nb_4C_3T_x$.[47]

Wang *et al.* developed another alternative method that involved addition of dilute NaOH and maintaining stirring at RT for 2 h to intercalate Na^+ between HF-etched multi-layered $Ti_3C_2T_x$, followed by using sulfanilic acid diazonium salts as surface modifier in an ice bath for 4h and finally mild

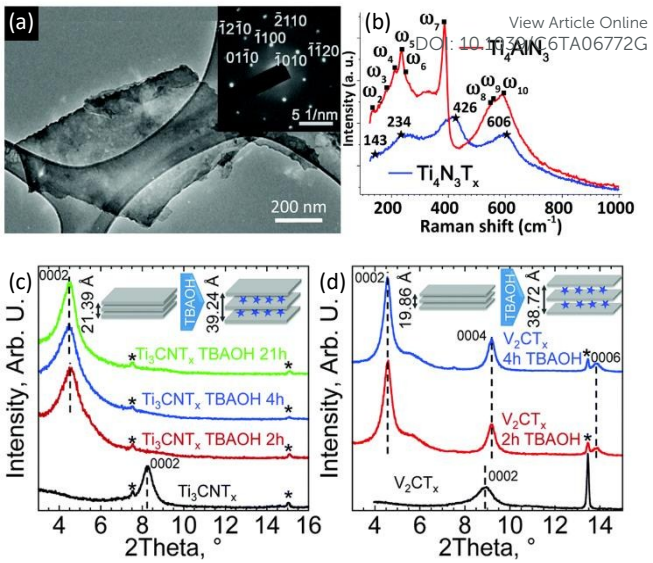

Fig. 5 (a) TEM image of an individual $Ti_4N_3T_x$ flake. Inset shows the SAED pattern of the $Ti_4N_3T_x$ flake, inheriting the hexagonal basal plane symmetry of the parent Ti_4AlN_3 phase. (b) Raman spectra of Ti_4AlN_3 (red curve) and delaminated $Ti_4N_3T_x$ (blue curve), with corresponding vibrational peaks identified through fitting with a product of Gaussian and Lorentzian functions [reprinted with permission from ref. 35. Copyright 2016 The Royal Society of Chemistry]. XRD patterns of (c) Ti_3CNT_x before TBAOH intercalation, and after mixing with TBAOH for 2, 4, and 21 h (black, red, blue and green curves, respectively); (d) V_2CT_x before TBAOH intercalation, and after mixing with TBAOH for 2, and 4 h (black, red, and blue curves, respectively). The peaks denoted by * are from remnant $M_{n+1}AX_n$ phases. Insets are schematics of the $M_{n+1}X_nT_x$ unit cells prior to, and after, TBAOH intercalation accompanied by the corresponding change in the *c* lattice parameter [reprinted with permission from ref. 45. Copyright 2015 The Royal Society of Chemistry].

sonication.[48] The intercalation of Na^+ is essential, as it further weakens the interlayer cohesive forces and allows the accommodation of aryl diazonium salts. Unreacted diazonium salts, being water-soluble, are relatively easier to remove as compared with the unreacted organic precursor(s) as used in other methods. Dispersing of $Ti_3C_2T_x$ in water can be improved with the grafting of aryl groups, while further surface modifications are made possible by the increased active sites on the surface, due to the attached reactive functional groups *p*-phenyl-SO_3H from the aryl diazonium salts.[48, 49] However, the applicability of this method towards other MXenes remains to be demonstrated.

Zhang *et al.* first demonstrated the feasibility of a substitutional solid solution based exfoliation to obtain parent $M_{n+1}AX_n$ nanosheets, about 4 nm thick and 100 to 200 nm wide, with ultrasonication in various organic solvents. It is suggested that only when the A layer in $M_{n+1}AX_n$ phases consists of different atoms and is in accordance to the Hume-Rothery rules, the effectiveness of breaking the bonds between A and MX layers can be significantly enhanced.[50] However, it is necessary to reemphasize that this low yield approach produces doped $M_{n+1}AX_n$ nanosheets but not MXenes. Thus, further treatments could be inclined towards complete conversion from these $M_{n+1}AX_n$ nanosheets to MXene and/or composite nanosheets, in

View Article Online
DOI: 10.1039/C6TA06772C

addition to extending the approach beyond $Ti_3Si_{0.75}Al_{0.25}C_2$ and $Ti_3Al_{0.9}Si_{0.1}C_2$.

2.3 MXene-based Composites

Ling *et al.* fabricated the first conductive, flexible, and free-standing $Ti_3C_2T_x$/polyvinyl alcohol (PVA) composite by using vacuum filtration of colloidal solutions of delaminated HF-etched multi-layered $Ti_3C_2T_x$ with DMSO as the intercalant, in the presence of varied amount of PVA (M_r = 115, 000). The $Ti_3C_2T_x$/PVA composite was established, because the PVA matrix had a strong interaction (hydrogen bonding) with the negatively charged surface of the $Ti_3C_2T_x$ fillers. Because of the film fabrication process, the $Ti_3C_2T_x$ layers were highly oriented and mostly parallel to the film surface. With 10 wt. % and 60 wt. % PVA, tensile strength of the $Ti_3C_2T_x$/PVA composite, as compared with pure $Ti_3C_2T_x$, was synergistically improved by about 34 % and 100 % respectively. However, its electronic conductivity was greatly compromised by a factor of 10^1 and 10^8 accordingly. A hollow, 6 mm in diameter and 10 mm tall, made with 4-5 µm thick 90 wt. % $Ti_3C_2T_x$/PVA film was able to sustain 2.9 MPa as compared with the 1.3 MPa by its pure $Ti_3C_2T_x$ counterpart.[51] Restacking of single- and few-layered $Ti_3C_2T_x$ flakes remained an unresolved issue.

Naguib *et al.* prepared a $Ti_3C_2T_x$/polyacrylamide (PAM) nanocomposite by casting a well-mixed solution of $Ti_3C_2T_x$/PAM onto a Teflon tray, followed by air-drying at room temperature over several days. A well dispersed $Ti_3C_2T_x$/PAM composite was formed as the DMSO-intercalated $Ti_3C_2T_x$ was swelled considerably and spontaneously attracted PAM (M_w 600 000 — 1 000 000 g mol^{-1}) solution when mixed, so that the hydroscopic PAM was favourably infiltrated and in-situ polymerized in between the $Ti_3C_2T_x$ layers.[52] In a 6 wt. % $Ti_3C_2T_x$ film, large quantity of PAM was available to intercalate into $Ti_3C_2T_x$. Thus, few-layered $Ti_3C_2T_x$ sheets were dispersed and randomly oriented. In comparison, in 31 wt. % $Ti_3C_2T_x$ film, multi-layered $Ti_3C_2T_x$ flakes were predominantly observed (TEM). With the incorporation of a mere 6 wt. % $Ti_3C_2T_x$, the insulating polymer matrix of PAM became semi-conducting, with an electrical conductivity to be 3.3×10^{-2} S m^{-1}. As the loading level of $Ti_3C_2T_x$ with further increased to 31 wt. %, the electrical conductivity behaviour of the $Ti_3C_2T_x$/PAM nanocomposite became metal-like, indicating that the electrical percolation threshold of PAM matrix had been overcame. Such composites may find applications in radio frequency (RF) shielding or static charge dissipation. Although no detailed quantitative characterization of mechanical properties of the $Ti_3C_2T_x$/PAM nanocomposite was conducted, it was generally observed that the addition of $Ti_3C_2T_x$ expectedly increased the stiffness of PAM.

Wu *et al.* incorporated DMSO-intercalated HF-etched $Ti_3C_2T_x$ fillers into a hydrophilic polyethyleneimine (PEI) matrix through solution mixing to prepare a hybrid active layer. Sequential drop-casting of homogeneous $Ti_3C_2T_x$/PEI and mixture of trimesoyl chloride (TMC) and n-hexane solution onto the surface of commercial polyacrylonitrile (PAN) ultrafiltration membrane and subsequent heat treatment at 60 °C for 2 h to remove residual solvent and complete the cross-linking reaction conclude the fabrication of composite solvent resistant nanofiltration (SRNF) membranes.[53] $Ti_3C_2T_x$ additives acquire good compatibility with the PEI polymeric matrix, as driven by hydrogen-bonding interaction, with noticeable weakened Fourier transform infrared spectroscopy (FTIR) characteristic bands' intensity of PEI in $Ti_3C_2T_x$/PEI composite. Intuitively, these fillers hinder polymer chain motion and enhance structural stability and solvent resistance of the PAN/PEI-$Ti_3C_2T_x$ membrane. Consequential of their large lateral area and small thickness, most $Ti_3C_2T_x$ nanosheets are horizontally-aligned and well dispersed within the PEI matrix, as observed with scanning electron microscopy (SEM). With 2 wt. % $Ti_3C_2T_x$, the rejection ability of the PAN/PEI-$Ti_3C_2T_x$ membrane for polyethylene glycol (PEG) solute is greatly improved, with molecular weight cut-off (MWCO) of approximately 200 Da. Expectedly, the inclusion of hydrophilic $Ti_3C_2T_x$ fillers slightly decreases the permeate flux for weak- or non-polar solvents, such as ethyl acetate, butanone and n-heptane, whereas the transfer ability for polar isopropanol is enhanced (ca. 30 %). It is proposed that the –OH groups on the $Ti_3C_2T_x$ surface function as adsorption sites and facilitate the storage of isopropanol molecules through hydrogen bonding interaction, which provide additional pathway for isopropanol molecules to transport along the surface and the inter-lapped gap. PAN-PEI SRNF membrane with 2 wt. % $Ti_3C_2T_x$ exhibits concurrent enhancement in membrane flux and rejection ability, overcoming the hitherto trade-off as demonstrated by other inorganic or graphene oxide fillers. Similarly, DMSO-intercalated HF-etched $Ti_3C_2T_x$ fillers were added into a hydrophobic polydimethylsiloxane (PDMS) matrix to prepare a different hybrid active layer for modifying SRNF membrane. (3-Aminopropyl) triethoxysilane (APTES) and dibutyltin dilaurate (DBTDL) were used instead of TMC. Although the $Ti_3C_2T_x$ additives are less compatible and weakly interact with PDMS matrix in the PAN/PDMS-$Ti_3C_2T_x$ membrane, as evidenced by SEM, FTIR and XRD, PAN/PEI-$Ti_3C_2T_x$ membrane exhibits concurrent enhancement in membrane flux for alcohol and rejection ability.

Aïssa *et al.* prepared a highly conductive $Ti_3C_2T_x$/graphene sandwich-like nanocomposite by alternatively depositing $Ti_3C_2T_x$ and graphene layers on a glass substrate, by using an electrohydrodynamic atomization (EHDA) deposition method.[54] These composite films were then annealed under vacuum at 200 °C for 2 h. The subsequent absence of F peak in XPS spectra suggested that this thermal treatment probably passivated the –F terminations. Both structural and electronic properties of the $Ti_3C_2T_x$ composite thin films are shown to be positively affected by the integration of graphene.

Zhao *et al.* proposed a repeated procedure of alternating vacuum filtration of delaminated HF-etched $Ti_3C_2T_x$ suspension and carbon nanotubes (CNTs) dispersion to prepare a flexible, free-standing sandwich-like 95 wt. % $Ti_3C_2T_x$/CNT composite film (Fig. 6a). For comparison, a randomly mixed 95 wt. % $Ti_3C_2T_x$/CNT was prepared by direct vacuum filtration of mixed 95 wt. % $Ti_3C_2T_x$/CNT dispersion. The sandwich-like 95 wt. % $Ti_3C_2T_x$/CNT composite was observed to have a more ordered structure, whereby sandwich-like superposition of $Ti_3C_2T_x$ and CNT layers (Fig. 6b) can be clearly identified to be unlike the

View Article Online DOI: 10.1039/C6TA06776G

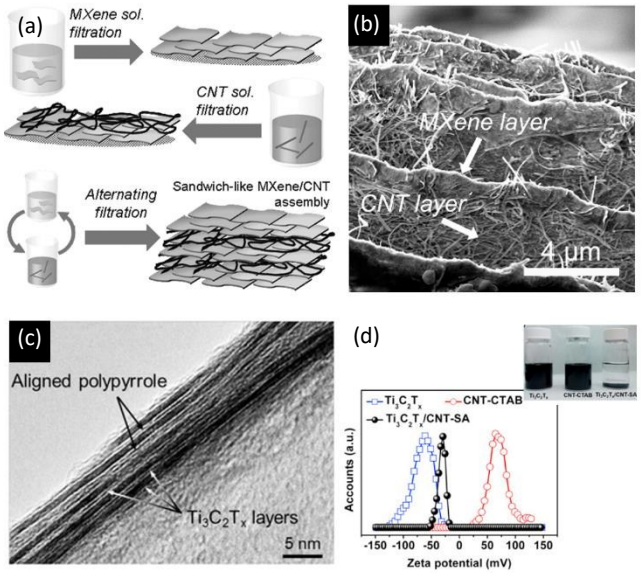

Fig. 6 (a) Schematic for the preparation of free-standing, sandwich-like $Ti_3C_2T_x$/CNT paper. (b) Cross-sectional SEM images of $Ti_3C_2T_x$/MWCNTs [reprinted with permission from ref. 55. Copyright 2014 John Wiley & Sons, Inc.]. (c) Cross-sectional TEM images of aligned PPy chains (bright) between $Ti_3C_2T_x$ layers (dark) [reprinted with permission from ref. 56. Copyright 2015 John Wiley & Sons, Inc.]. (d) Zeta potential of HCl/LiF etched $Ti_3C_2T_x$ nanosheets, CTAB-grafted CNTs (CNT-CTAB), and self-assembled $Ti_3C_2T_x$/CNT-CTAB ($Ti_3C_2T_x$/CNT-SA). Inset shows digital photographs of pristine $Ti_3C_2T_x$ suspension, CNT-CTAB in water, and $Ti_3C_2T_x$/CNT-SA composites [reprinted with permission from ref. 57. Copyright 2016 Elsevier].

randomly mixed $Ti_3C_2T_x$/CNT composite. This elucidates the effect of CNT dispersion conditions during the preparation and the implication on the arrangement of fillers, electronic percolation threshold and subsequent enhancement of overall electronic transport properties as noted in the superior conductivity of sandwich-like $Ti_3C_2T_x$/CNT composite (385 S cm^{-1}) than that of randomly mixed $Ti_3C_2T_x$/CNT composite (286 S cm^{-1}). It was generally observed that the inclusion of CNTs enlarged interlayer space (i.e., *c* lattice parameter revealed by XRD) between the $Ti_3C_2T_x$ flakes, prevented the restacking of delaminated $Ti_3C_2T_x$ sheets (Fig. 6b) and improved both the overall conductivity and available active surface area within the composites and thus electrochemical performance in electrochemical capacitors (ECs), as compared with those of the pure $Ti_3C_2T_x$ film.[55] This alternating vacuum filtration method is also advantageous for its simplicity, because no functionalization of the materials is required. It could be used to quickly fabricate several micrometres thick film, though it lacks the more controlled structures that can be realized by using the layer-by-layer (LBL) deposition method.

Similarly, Mashtalir *et al.*, used i-PrA as the intercalant to delaminate HF-etched multi-layered Nb_2CT_x, and produce a flexible and free-standing randomly mixed 90 wt. % Nb_2CT_x/MWCNTs composite "paper". A suspension of MWCNTs dispersed by 0.03 mol L^{-1} sodium dodecylsulphate (SDS) was added into the colloidal mixture of mono- and few-layered Nb_2CT_x, followed by direct vacuum filteration.[47]

Boota *et al.* introduced a simple strategy to prepare free-standing but brittle film of a self-assembled layered structure, with aligned and doped pyrrole (PPy), C_4H_4NH, confined between the $Ti_3C_2T_x$ single layers (Fig. 6c). The solution for vacuum filtration to obtain the composite film was prepared by adding the as-received PPy to a dispersion of HCl/LiF etched $Ti_3C_2T_x$, and constant stirring at 1000 rpm for 12 h at RT. Exploiting the acidic nature of $Ti_3C_2T_x$, PPy molecules may be protonated and proceed to form longer chains. Similarly, with the presence of =O, –OH and –F terminations on $Ti_3C_2T_x$ surfaces, hydrogen bonds may be established with the N-H group in PPy oligomers, so that the polymerized chains are self-aligned instead of being randomly aggregated. Concurrently, the PPy chains can be doped by –F to become conductive. Simultaneous intercalation, alignment, and metal free polymerization of PPy on $Ti_3C_2T_x$ were demonstrated. By optimizing the content of PPy, which provides directional paths for charge percolation between the $Ti_3C_2T_x$ layers, the obtained composites with enhanced electronic conductivity demonstrated exceptional performance as electrodes of supercapacitors.[56]

Xie *et al.* proposed another electrostatic self-assembly method to prepare flexible free-standing composite films of 90 wt. % $Ti_3C_2T_x$/MWCNTs and Mo_2CT_x/MWCNTs from negatively charged delaminated HCl/LiF etched $Ti_3C_2T_x$ and Mo_2CT_x and positively charged MWCNTs as spacers. Self-assembly was only possible with MWCNTs grafted with cetyltrimethylammonium bromide (CTAB), a cationic surfactant (Fig. 6d). If the MWCNTs were modified with an anionic surfactant, such as SDS, the self-assembly was not successful and $Ti_3C_2T_x$ and MWCNTs would be randomly and separately deposited on the filter paper, while restacking of single- and few-layered $Ti_3C_2T_x$ flakes remained unresolved. Consequently, the 90 wt. % $Ti_3C_2T_x$/MWCNTs-CTAB composite displays encouraging volumetric capacity and rate performance as Na-ion storage, because the CTAB-modified MWCNTs efficiently reduced the restacking of the single and few-layered $Ti_3C_2T_x$, thus improving the accessibility of electrolyte to the active material, $Ti_3C_2T_x$. The CTAB-modified MWCNTs also formed a conductive network and enhance overall electronic conductivity of the composites.[57]

Lin *et al.* alternatively improved the electronic conductivity of HF-etched multi-layered $Ti_3C_2T_x$, by growing conductive carbon nanofibers (CNFs) within the spaces of each accordion-like $Ti_3C_2T_x$ particle and between the particles (Fig. 7a). The CNFs within the void of $Ti_3C_2T_x$ provide conductive pathways to enhance charge transportation in the vertical-to-layer direction of each individual $Ti_3C_2T_x$ particle and maintain the open accordion-like structure which is favourable for electrolyte ions to access. Isolated $Ti_3C_2T_x$ particles are connected by conductive network of CNFs, thereby drastically reducing contact resistance between the adjacent sheets.[58] By using liquid-phase impregnation, a cobalt (II) nitrate ($Co(NO_3)_2$ catalyst precursor and poly(vinyl pyrrolidone (PVP) dispersant were introduced into the multi-layered $Ti_3C_2T_x$, while the succeeding heat treatment at 600 °C in Ar for 0.5 h led to the carbonization with acetylene as the carbonaceous source, and synchronous passivation of surface functional groups of $Ti_3C_2T_x$. The growth of CNFs followed the tip growth mechanism as evidenced by a

View Article Online
DOI: 10.1039/C6TA06772G

pit produced on the top of the CNF when Co catalyst was removed.

Similarly inspired by the ion exchange occurring at the hydroxyl (–OH) groups on $Ti_3C_2T_x$ surfaces, Luo *et al.* synthesized a PVP-Sn^{4+}@$Ti_3C_2T_x$ nanocomposite (Fig. 7b). By adding HF-etched multi-layered $Ti_3C_2T_x$ into 1 M of lithium hydroxide (LiOH), the interlayer spaces could be enlarged and the –F surface terminations were converted to –OH ones. Through a subsequent liquid-phase impregnation of a tin (IV) chloride ($SnCl_4$) precursor with PVP dispersant, Sn^{4+} ions were anchored on negatively charged $Ti_3C_2T_x$ surfaces as an amorphous Sn (IV) complex, due to ion exchange and electrostatic interactions (Fig. 7c). 2D conductive $Ti_3C_2T_x$ matrix serves varyingly as ion exchange sites, buffer layer to accommodate the volumetric change during electrochemical reaction, partial capacity of the entire composite and endowment of excellent rate performance. Interestingly, a synergistic "pillar effect", i.e., spontaneous expansion of anchored Sn (Fig. 7d) and alloying with Li^+, which concurrently pushed the $Ti_3C_2T_x$ interlayers further apart to allow more Li^+ ions to intercalate, was proposed to significantly contribute to its overall exceptional electrochemical capacity of the composite that far exceeds that of pure $Ti_3C_2T_x$.[59]

Naguib *et al.* actualized and proved the concept of oxidizing HF-etched multi-layered $Ti_3C_2T_x$ in air, CO_2, or pressurized DI water. Hampered by uncontrolled synthesis condition, anatase TiO_2 nanocrystals, with divergent morphologies and sizes, embedded in amorphous carbon sheets (TiO_2-C hybrid structure), were formed when $Ti_3C_2T_x$ powders were flash oxidized in air at 1150 °C for 30 s. However, when subjected to either isothermal oxidation in pure CO_2 between 150 to 300 °C

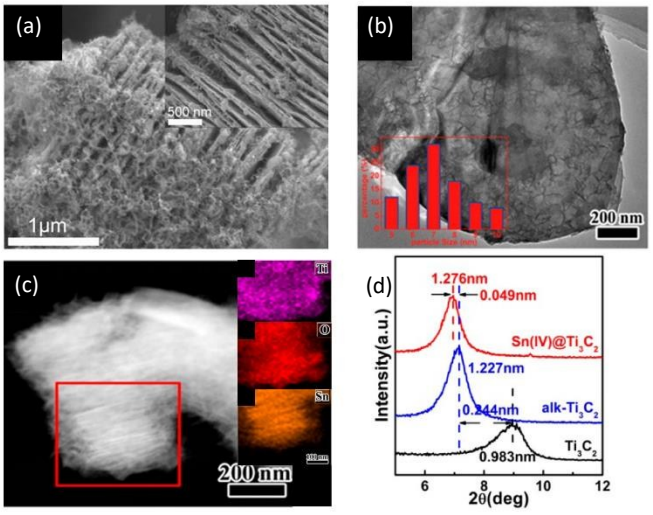

Fig. 7 (a) SEM image of HF-etched multi-layered $Ti_3C_2T_x$-CNT composite. Inset shows that some CNFs grew within the interlayer spaces of $Ti_3C_2T_x$ flakes [reprinted with permission from ref. 58. Copyright 2015 The Royal Society of Chemistry]. (b) TEM image of PVP-Sn^{4+}@$Ti_3C_2T_x$. Inset shows the lateral size distribution of the anchored Sn^{4+} nanocomplex particles. (c) STEM image of PVP-Sn^{4+}@$Ti_3C_2T_x$. Inset shows the corresponding elemental mapping of Ti, O, and Sn. (d) Close-up XRD patterns of three different samples ($Ti_3C_2T_x$, alk-$Ti_3C_2T_x$, and Sn^{4+}@$Ti_3C_2T_x$) [reprinted with permission from ref. 59. Copyright 2016 American Chemical Society].

for 1h or hydrothermal treatment at 150–250 °C at 1 to 5 MPa for various durations, a hybrid structure with low content of unreacted $Ti_3C_2T_x$ (as evidenced by remnant XRD peaks) and varied shaped and sized anatase TiO_2 nanocrystals embedded in amorphous carbon sheets was formed instead. Hydrothermal oxidation of HF-etched multi-layered Nb_2CT_x at 150 °C for 2h yielded a hybrid structure of Nb_2CT_x, coupled with feather-like non-crystalline Nb_2O_5, with a low content of amorphous carbon.[60] Amongst these three synthesis routes, hydrothermal synthesis offers the most convenient control over morphology of the oxide particles, together with the requirement of generally low temperatures albeit longer duration. Ghassemi *et al.* investigated the $Ti_3C_2T_x$ oxidation mechanism by using in situ TEM analysis. [61] They found that TiO_2 nanoparticles were formed from top and bottom of the Ti layers during flash oxidation whereas nanocrystalline TiO_2 sheets were formed instead during slow oxidation.

Coincidentally, Li *et al*. also identified that $Ti_3C_2T_x$ could be partially oxidized by O_2 at low temperature of 200 °C for an accumulated period of 40 min to form evenly distributed anatase TiO_2 nanoparticles on $Ti_3C_2T_x$ sheets, variant to that of TiO_2-C hybrid structure by Naguib *et al.*; and at higher temperature, the synthesized anatase TiO_2 nanoparticles would then be transformed to rutile TiO_2 nanoparticles.[62]

Zhang *et al*. synthesized a layered hierarchical structure composite of orthorhombic Nb_2O_5 nanoparticles, which were uniformly decorated on surface of the $Nb_4C_3T_x$ flakes and intertwined with amorphous carbon, by using a facile one-step oxidation of HF-etched $Nb_4C_3T_x$ powders in CO_2 at 850 °C for 0.5 h (Fig. 8a). Similarly, hierarchical composites of Nb_2O_5@Nb_2CT_x and TiO_2@$Ti_3C_2T_x$ were derived from Nb_2CT_x and $Ti_3C_2T_x$, respectively by using the CO_2 partial oxidation method.[63] Such a hierarchical design is advantageous for electrochemically active and high rate-response metal oxide nanocrystals, i.e., Nb_2O_5 or TiO_2, are at the edges (Fig. 8b) and interlayers and directly exposed to the electrolyte, so that ion diffusion paths are effectively shortened. Meanwhile, the internal network of the highly conductive carbon and unoxidized MXenes promotes the overall electronic conductivity of the composites. Additionally, the carbon can probably also function similarly to that of a binder and strengthen interaction between the metal oxide and MXene particles.

In a separate study, the same group explored the influences of oxidation temperature, time and CO_2 feed rate on the phase composition, particle size of Nb_2O_5, constitutions of the hierarchical composites and the corresponding electrochemical performances (Fig. 8c).[64] A similar phenomenon for Ti_2CT_x was reported, laying the groundwork for modification and/ or elimination of surface groups by using heat treatment or post-etch annealing in various gas environments to structurally alter the morphology of Ti_2CT_x, partially oxidize Ti_2CT_x to form TiO_2 under certain conditions and thus favourably impact its electrochemical performance.[65, 66] In the latter, it was noted that annealing Ti_2CT_x in various controlled atmospheres, such as Ar, N_2 or N_2/H_2, retained its initial chemical structure but caused slight thinning of the layers (i.e., larger interplanar distance and

View Article Online
DOI: 10.1039/C6TA06772G

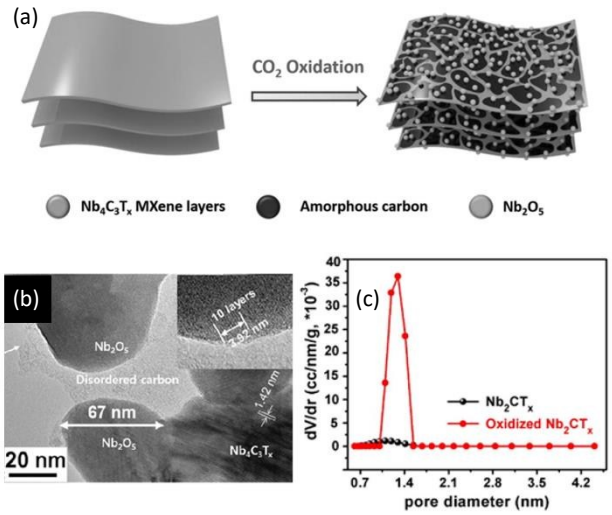

Fig. 8 (a) Schematic for structure of $Nb_4C_3T_x$ and its hierarchical composite structure after oxidation. (b) TEM image of oxidized $Nb_4C_3T_x$ at 850 °C for 0.5 h under a CO_2 flow rate of 75 sccm. Inset shows a higher resolution TEM image [reprinted with permission from ref. 63. Copyright 2016 John Wiley & Sons, Inc.]. (c) Pore size distribution comparison of Nb_2CT_x before and after CO_2 oxidation at 800 °C for 1 h at a CO_2 feed rate of 150 sccm, the formation of 1.0-1.5 nm pores is indicative of the formation of voids between the layers of Nb_2CT_x after CO_2 oxidation [reprinted with permission from ref. 64. Copyright 2016 American Chemical Society].

higher surface areas), thus leading to a favourable mesoporous structure to allow more access of aqueous electrolyte. Noticeably, annealing in N_2/H_2 atmosphere removed more functional groups on Ti_2CT_x, as inferred from the highest carbon content and lowest fluorine concentration, than in Ar or N_2, and consequently exhibited the highest specific capacitance.[66] Lai *et al.* also reported the preservation of initial Ti_2CT_x layered framework and modifications to surface functional groups and carrier transport properties (from metallic to semiconducting) after subjecting mechanically exfoliated Ti_2CT_x sheets to thermal annealing.[67]

Ahmed *et al.* demonstrated a scalable, cost efficient and rapid method at RT to obtain TiO_2/Ti_2CT_x hybrid. By immersing HF-etched multi-layered Ti_2CT_x in hydrogen peroxide (H_2O_2) with various concentrations for different durations at RT, the amount of anatase TiO_2 nanoparticles formed and embedded on the surface of multi-layered Ti_2CT_x could be well controlled. The surface defects of HF-etched Ti_2CT_x acted as nucleation sites for TiO_2 formation. For instance, after a brief (5 min) immersion in 30 wt. % H_2O_2, TiO_2 nanoparticles were formed at the expense of Ti_2CT_x and the Ti_2CT_x layers were swelled, thus leading to a five-fold increment in specific surface area (SSA) and more active sites for Li^+ ions to intercalate. This hybrid has a molar composition of one Ti_2CT_x and four TiO_2. Comparatively, for an extended period of immersion of 5 h, Ti_2CT_x was completely converted into TiO_2.[68]

A myriad of particulate $TiO_2/Ti_3C_2T_x$ composites have been hydrothermally synthesized, with or without additional variant Ti precursors, at various heating temperatures for various durations. Gao *et al.* prepared $TiO_2/Ti_3C_2T_x$ composites with promising photocatalytic activity by heating a mixture of HF-etched multi-layered $Ti_3C_2T_x$, different amount of titanium (II) sulfate ($TiSO_4$) and DI water at 180 °C for 18 h. Through an in situ hydrolysis of tetrabutyl titanate (TBOT) within a mixture of HF-etched multi-layered $Ti_3C_2T_x$, followed by either a microwave-assisted hydrothermal synthesis or heat treatment in vacuum, Wang *et al.* synthesized another two types of $TiO_2/Ti_3C_2T_x$ composites for potential applications in electrochemical biosensors and supercapacitor electrodes.[70, 71] The organ-like and conductive $Ti_3C_2T_x$ structure, with high SSA, capably channels large quantity of enzymes towards the interior and immobilizes them between the interlayers. Additionally, biocompatible TiO_2 nanoparticles present a protective and conducive environment for these enzymes to remain active and collide with each other for long period.

Another group hydrothermally synthesized rutile $TiO_2/Ti_3C_2T_x$ composites with various contents of HF-etched delaminated $Ti_3C_2T_x$ but fixed amount of titanium (IV) chloride ($TiCl_4$) at 95 °C for 4 h. TiO_2 strategically encapsulated the $Ti_3C_2T_x$, and this intimate contact allowed efficient charge transfer from TiO_2 to $Ti_3C_2T_x$. The variation of $Ti_3C_2T_x$ content in the composites was reportedly influential towards deviation in both optical properties and photocatalytic performance as excessive $Ti_3C_2T_x$ scattered light and prevented TiO_2 from efficiently capturing light. This synthesis was extended to prepare TiO_2/Ti_2CT_x and TiO_2/Nb_2CT_x composites.[72]

Exceptionally, without additional Ti source, Peng *et al.* fabricated an atomic scale interfacial heterojunction of homogeneously distributed (001) TiO_2 nanosheets inserted in layered $Ti_3C_2T_x$ (Fig. 9a-f), through delicately controlled hydrothermal oxidation of HF-etched multi-layered $Ti_3C_2T_x$ in the presence of directing agent, sodium tetrafluoroborate ($NaBF_4$). This minimally defective and interfacial well-bonded (001) $TiO_2/Ti_3C_2T_x$ hybrid exhibited significantly enhanced photocatalytic activity as the defect-induced electron-hole recombination was reduced and highly conductive $Ti_3C_2T_x$ efficiently conducted photogenerated electrons away and increased the lifetime of photogenerated electron-hole pairs.[73]

Zhang *et al.* fabricated a sandwich-like, magnetic $Ti_3C_2T_x$/magnetite (Fe_3O_4)/maghemite (Fe_2O_3) composite with enhanced phosphate sorption selectivity and capacity. A mixture of 1 M $FeSO_4$, 2 M iron (II) chloride ($FeCl_3$) and HF-etched multi-layered $Ti_3C_2T_x$ was held isothermally at 80 °C for 4 h to facilitate ion exchange reactions that resulted in Ti-Fe in place of Ti–H terminations as well as intercalate Fe^{2+} and Fe^{3+} ions. This mixture was then added to a boiling 6 M NaOH solution, to convert remnant Fe salts to Fe-based hydroxides. By maintaining at 100 °C for 5 h, the Fe-based hydroxides were then transformed into nanosized ferrites.[74]

Ren *et al.* developed a chemical etching procedure to prepare mesoporous $Ti_3C_2T_x$ at RT (Fig. 9g). An aqueous solution of copper (II) sulphate ($CuSO_4$) was added to a colloid of delaminated HCl/LiF etched $Ti_3C_2T_x$. Catalysed by Cu^{2+} ions, the dissolved O_2 in water partially oxidized the $Ti_3C_2T_x$ flakes, forming TiO_2 nanoparticles that were removed by subsequent HF treatment to leave behind porous $Ti_3C_2T_x$ flakes (Fig. 9h)with more defects, less –F, more =O and –OH terminations and larger exposed surfaces.[75] These mesoporous $Ti_3C_2T_x$ flakes are then

View Article Online
DOI: 10.1039/C6TA06772G

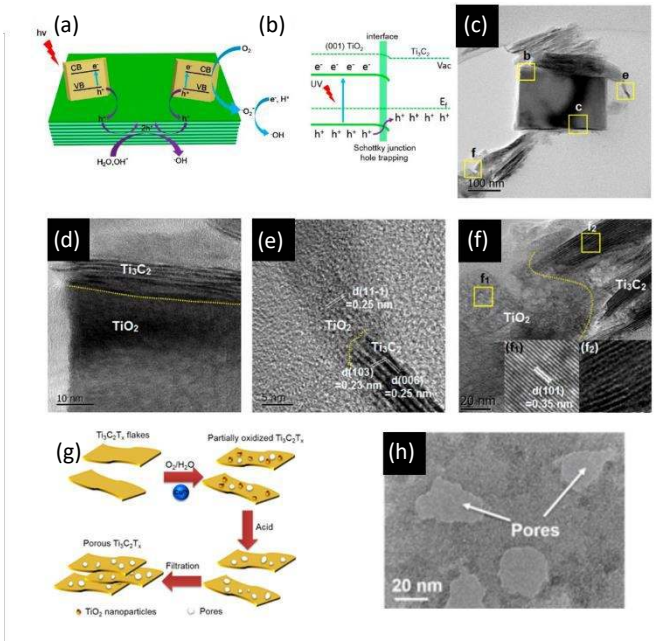

Fig. 9 Schematic for (a) Charge-transfer process over (001) $TiO_2/Ti_3C_2T_x$, (b) Band alignments and charge flow at {001} $TiO_2/Ti_3C_2T_x$ interfaces. (c) Low resolution TEM image of $TiO_2/Ti_3C_2T_x$. High resolution TEM image of (d) the area highlighted by yellow box labelled b in (c), shows the intimate proximity of layered $Ti_3C_2T_x$ and a TiO_2 crystal, (e) the growth of TiO_2 perpendicular to the [001] direction of the $Ti_3C_2T_x$ sheet, and (f) small TiO_2 crystal formed near the edge of $Ti_3C_2T_x$. The insets (f_1) and (f_2) show the lattice fringes of TiO_2 and $Ti_3C_2T_x$ respectively [reprinted with permission from ref. 73. Copyright 2016 American Chemical Society]. (g) Schematic for the chemical etching of $Ti_3C_2T_x$ flakes to produce porous $Ti_3C_2T_x$ structure. (h) TEM image of porous $Ti_3C_2T_x$ after chemical etching in 0.2 M $CuSO_4$ solution at RT [reprinted with permission from ref. 75. Copyright 2016 Wiley].

used together with MWCNTs to prepare electrode materials with promising performances.

Ma *et al.* combined delaminated HF-etched $Ti_3C_2T_x$ and exfoliated graphitic carbon nitride (g-C_3N_4) nanosheets through vacuum filtration to form a robust free-standing hybrid film. It exhibited outstanding performance in catalysing oxygen-evolution reaction (OER) due to this novel coupled Ti-N_x motifs acting as electroactive sites, high surface area from hierarchically porous structure contributed to a high electrochemical double layer capacitance. Additionally, its hydrophilic and porous nature allowed good wettability of active surfaces with aqueous electrolyte and rapid transport of reactants to the active sites and fast removal of reaction products, such as O_2.[76]

Zhang *et al.* synthesized an urchin-shaped alkalization-intercalated HF-etched $Ti_3C_2/Ag/Ag_{0.9}Ti_{0.1}$ bimetallic nanowire composite (Fig. 10a-d) by mixing 30 mM of $AgNO_3$, 100 mg of 6 M NaOH-activation-treated $Ti_3C_2T_x$ and 100 mg of PVP in DI water at room temperature. It was proposed that the NaOH-activation-treatment of $Ti_3C_2T_x$ substituted –F groups with –OH groups and increased the *c* lattice due to ion exchange forming –ONa groups from some –OH groups. The presence of activated low-valence Ti species on $Ti_3C_2T_x$ was ascribed to Ag self-reduction while addition of PVP induced the formation of 5-fold nanotwin Ag seeds (Fig. 10d), which subsequently grew into Ag/Ti ($Ag_{0.9}Ti_{0.1}$) bimetallic nanowires (Fig. 10c). This nanocomposite, with enhanced conductivity, numerous oxygen adsorption sites and shortening the diffusion path of adsorbed oxygen, displayed encouraging electrocatalytic activity for ORR, whereby its onset potential and half-wave potential are higher than commercial 20 wt. % Ag/C and previous reported Ag-based catalysts.[77] This group also evaluated a HF-etched Ti_3C_2/Ag composite, synthesized without the NaOH-activation-treatment of $Ti_3C_2T_x$ and PVP addition, as a high rate anode material for Li-ion batteries with excellent cyclability.[78]

Chen *et al.* initiated, in the absence of an initiator, grafting of poly(2-(dimethylamino)ethyl methacrylate) (PDMAEMA) onto HF-etched multi-layered V_2CT_x by using a facile method of self-initiated photografting and photopolymerization (SIPGP) to prepare V_2CT_x@PDMAEMA composite.[79] The cationic-charged PDMAEMA favourably interacted with the negatively charged surface of V_2CT_x to form a composite. Consequently, V_2CT_x was endowed with the versatile reversible hydrophilic to hydrophobic behaviour of PDMAEMA when thermally stimulated and the controlled conductivity as triggered by carbon dioxide (CO_2) stimulation, and such functionalized V_2CT_x hybrids may potentially find applications in biological field.

Experimentally, in most MXene/polymer composites to date, in which MXene is the additive and polymer serves as the matrix, DMSO-intercalated HF-etched $Ti_3C_2T_x$ single/few-layered fillers have been unanimously added to polymeric matrices. Polymeric-based composites which incorporate other MXenes, beyond DMSO-intercalated HF-etched $Ti_3C_2T_x$, expectedly remain unexplored because of the trickle-down effect from the bottleneck in effective preparation of other single/few-layered MXenes. Gradually, as more other exfoliated

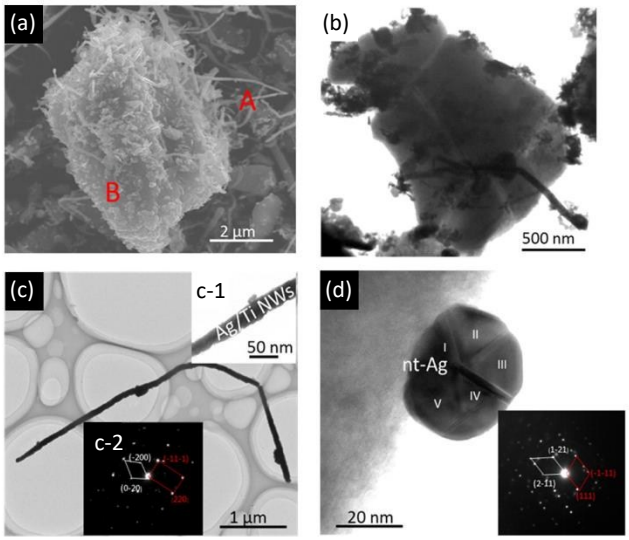

Fig. 10 FESEM image of the HF-etched $Ti_3C_2/Ag/Ag_{0.9}Ti_{0.1}$. A and B represent a Ag nanowire and a Ag nanoparticle, respectively. (b) TEM image of the $Ti_3C_2/Ag/Ag_{0.9}Ti_{0.1}$. (c) HRTEM image of nanowire A. Inset (c-1) shows the width of $Ag_{0.9}Ti_{0.1}$ nanowire ~42 ± 5 nm. Inset (c-2) shows the SAED fringe confirming the nanotwinned Ag structure. (d) HRTEM image of nanoparticle B with a 5-fold twin; the inset corresponds to the SAED of nanoparticle B [reprinted with permission from ref. 77. Copyright 2016 American Chemical Society].

View Article Online
DOI: 10.1039/C6TA06772G

single/few-layered MXenes are prepared, their incorporation into polymeric composites with new properties and applications are to be explored in the near future.

Critical to fabricating a well-mixed MXene/polymer composite, the selection of polymer must also take into consideration its solubility in solvent(s) during processing, in addition to having the polymer favourably interact with negatively-terminated MXene surface. Generally, mechanical properties of polymeric composites are enhanced with the addition of MXene fillers, although the orientation or how the fillers are randomly stacked is influential towards if the enhanced mechanical properties are anisotropic or isotropic.[52]

As mentioned above, one early strategy to improve the electrochemical performance of MXene-based composites is to open the structure of the multi-layered MXene matrix through delamination and reassembling them into a porous "paper"-like structure. Incorporation of interlayer spacers, such as CNTs, or conductive polymers, such as PPy, have further enhanced the electrochemical performance of the free-standing "papers" by increasing their electrical conductivities (with additional electron conductive pathways) and interlayer spaces that promote electrolyte ion access and transportation.[47, 55-58] Since no polymeric binders or conductive additives are included, undesirable dead volume and interface are reduced and associated overpotentials are eliminated.

Surface terminations of MXenes are chemically modified, so that it is able to change from one predominant surface group to another, so as to more effectively attach cations to increase interlayer spacings, or to facilitate subsequent procedures such as oxidation or self-assembly, and achieve hitherto properties and improved performances than their non-composite counterparts.[59, 80, 81] Functionalization of MXene-based additives or matrices to endow desirable and hitherto properties, such as enhancement of the matrix-filler interfacial strengths, remains to be conducted. Passivation or removal of MXenes' inherent surface functional groups is also possible through thermal treatment in Ar, hence presenting a wide array of probable modifications to be studied for work with or around microscopically defective and varyingly surface terminated MXene-based materials. Hydrothermal oxidation, which offers scalable products and highly reproducible crystallinity, well morphological and compositional control, relatively low temperature and short duration, seems to be most preferred method to develop MXene/oxide composites, and alternative methods remain yet to be explored.[60, 63, 68-74]

Similarly, intimate contact between the conducting MXene matrices and well-dispersed fillers, be it as-synthesized oxides or CNTs, is crucial to the overall homogeneity and properties of MXene-based composites. It remains intriguingly challenging to alternatively attain a hierarchical structure with such intimate contact and well-distribution of exposed foreign additive material(s) amongst the MXene matrix network if the MXene does not participate as both the precursory source of metal cations and as the supporting matrix structure itself. Details for the performance of various composites in their respective applications and the comparison in electrochemical performances amongst some composites will be discussed in the following section.

3. Structures, Properties and Applications

Various as-synthesized MXenes are endowed with the rare combination for 2D materials of good electronic conductivity comparable to multi-layered graphene and high hydrophilicity with small contact angles measured.[14] Intercalated epitaxial MXene thin films (< 20 nm) are highly transparent with about 90 % transmittance (T) in the visible-to-infrared region.[25] Weak coupling between stacked MXene layers, spontaneous intercalation of a variety of organic and inorganic molecules or ions and subsequent delamination to single or few layers via sonication have been demonstrated.[25, 26, 31, 35, 43, 45-48] Understanding both the surface terminations and the interlayer interactions is the prerequisite to purposefully manipulating the properties of MXenes for their various applications. Consequently, modelling and simulation, such as density functional theory (DFT) and to a lesser extent, molecular dynamics (MD) simulations, have been extensively applied to understand the structure, to predict properties and to identify potential applications of MXenes, guiding much of the experimental research in the field of MXenes, although most of earlier modelling works are regarding uniform terminating species.[34, 82-105]

On the basis of DFT calculations, Srivastava *et al.* detailed the mechanism of exfoliation and simultaneous functionalization of

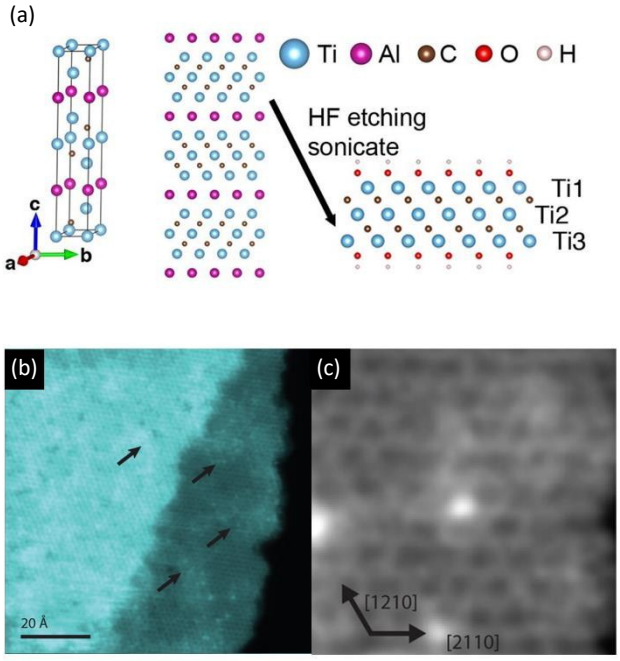

Fig. 11 (a) Crystal structure model of MAX phase Ti_3AlC_2 (left), MAX phase Ti_3AlC_2 projected along the *a* axis (middle), and MXene phase $Ti_3C_2T_x$ projected along the *a* axis (right) with −OH-terminated functional groups. The three Ti sublayers are labelled Ti1, Ti2, and Ti3 [reprinted with permission from ref. 108. Copyright 2016 American Chemical Society]. (b) Atomic resolution HAADF-STEM image of a typical $Ti_3C_2T_x$ sheet with the positions of surface groups labelled by the arrows. (c) HAADF-STEM image of a Ti adatom on a single $Ti_3C_2T_x$ sheet [reprinted with permission from ref. 107. Copyright 2015 American Chemical Society].

$Ti_3C_2T_x$ by HF etchant.[106] The Ti atoms on the edges of parent phase Ti_3AlC_2 were proposed as the initial sites for dissociated H/F ions to attach onto, subsequently weaken Ti-Al bonds and increase interlayer gap for more HF molecules to intercalate. Al was then removed from Ti_3AlC_2 due to the formation and release of AlF_3 and H_2, leaving behind Ti_3C_2 that strongly bond to –OH and –F. Density of state and electron localization function calculations identified that the functionalization of Ti_3C_2 was motivated by the formation of strong bonds. Gibbs free energy (ΔG) calculations indicated that the formation of fully fluorinated or mixed functionalized Ti_3C_2 were both thermodynamically favourable and conferred the random, uncontrolled and mixed functionalization of Ti_3C_2. Consistent with a recent NMR study, more of –F terminations were observed due to the preference of higher electronegativity of F ions and associated greater stability to the overall structure.[37] The random and non-uniform distribution of surface termination groups on MXenes is consequential of the chemical exfoliation process itself, and re-emphasizes the need for development of alternative preparation routes to achieve controlled functionalization of MXenes.

Early theoretical models predicted $Ti_3C_2T_x$ configurations, in which surface termination groups were energetically favoured to be located either above the hollow sites between three neighbouring C atoms or above the C atoms on both sides of the Ti_3C_2 or a combination of the aforementioned.[97, 98] However, later computational studies revealed the complexity in the locations and orientations of surface groups for they depended on the species (n values) and elemental compositions.[100, 101] Xie *et al.* suggested that =O and/ or –OH terminated MXenes were the most stable, because –F terminations were readily replaced by –OH groups, which could occur when they were washed and/or stored in H_2O; and –OH was converted to –O terminations during the high temperature treatments and/or metal adsorption processes.[102]

Karlsson *et al.* investigated the structural, elemental and chemical properties of single and double sheets of $Ti_3C_2T_x$ (prepared by immersion of 2.5 g of Ti_3AlC_2 1 M NH_4HF_2 for 5 days) by aberration-corrected atomic-resolution scanning transmission electron microscopy (STEM)-electron energy loss spectroscopy (EELS). Under high angle annular dark-field (HAADF)-STEM imaging, with Ti-sites as reference, the inherited close-packed structure of $Ti_3C_2T_x$ was observed as atomic positions of two $Ti_3C_2T_x$ sheets remained laterally aligned (Fig. 11b) even after the removal of Al layers. Non-uniform coverage of O-based surface groups on $Ti_3C_2T_x$, native point defects such as Ti vacancies and oxidized titanium adatoms (TiO_x) (Fig. 11c) were also observed.[107]

Sang *et al.* similarly adopted STEM-EELS to characterize single layer $Ti_3C_2T_x$ (using 7.5:1 molar ratio of LiF to Ti_3AlC_2, in 6 M HCl at 35 °C for 24 h). The prevalence of different point defects (single Ti vacancies, Ti vacancy clusters) in the monolayer flakes and the importance of etchant concentration in defect formation was elucidated. The experimental HAADF-STEM image of $Ti_3C_2T_x$ flake was ascertained to be that of a single layer through comparison with similarly oriented simulated HAADF-STEM images calculated by using multislice algorithm (Fig. 12a-b). Additionally, DFT simulations were performed to provide insight on the energetic costs associated with Ti defect formation, and the influence of different functional groups on the stability of the vacancies. Ab initio molecular dynamics (AIMD) simulations were adopted to theoretically study the influence of the

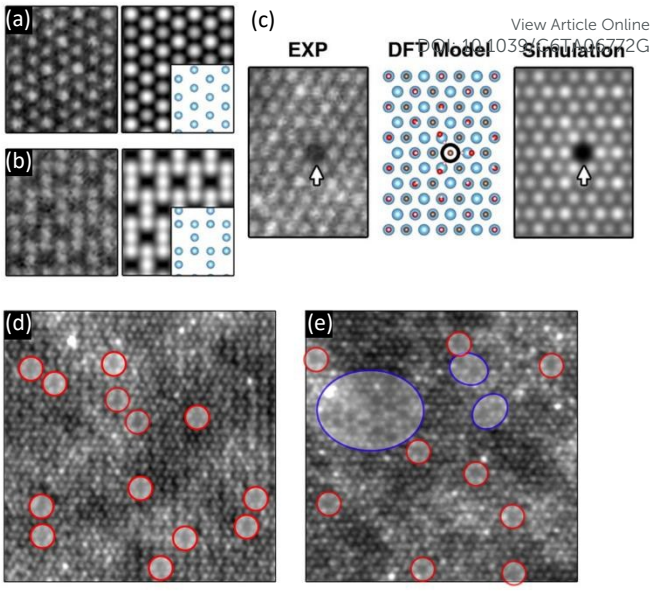

Fig. 12 Comparison between experimental high-resolution HAADF-STEM images and simulated HAADF-STEM images for $Ti_3C_2T_x$ MXene from a single layer at two different off-tilt orientations: (a) α = 0 and β = 0 mrad; (b) α = 0 and β = −189 mrad. Insets show the projected arrangement of Ti atoms for each case. (c) Atomic-scale HAADF-STEM images of defects in single-layer $Ti_3C_2T_x$. Comparison between experimental HAADF-STEM image, defect crystal structure determined from DFT, and simulated HAADF-STEM image of V_{Ti}. HAADF-STEM images from single-layer $Ti_3C_2T_x$ MXene flakes prepared using etchants with different HF concentrations: (d) 2.7 wt. % HF and (e) 5.3 wt. %. Single V_{Ti} vacancies and vacancy clusters V_{Ti}^C are indicated by red and blue circles, respectively [reprinted with permission from ref. 108. Copyright 2016 American Chemical Society].

defects on the surface chemistry and electronic properties of $Ti_3C_2T_x$ and derived at insensitivity of $Ti_3C_2T_x$'s conductivity to defect concentration. Experimentally, with 2.7 wt. % HF etchant, vacancy clusters were rarely observed in $Ti_3C_2T_x$ single layer, however with 5.3 wt. % HF etchant, vacancy clusters became more of a common sight (Fig. 12d-e).[108]

Coinciding with DFT calculations, the electronic properties (metallic or semi-conductive), thermodynamic stability, intercalation mechanisms and energy storage capability of MXenes are also found to be dependent on defects and surface terminations. Beyond =O, –OH, and –F, there could exist other stable and viable surface terminations, such as methoxy ($–OCH_3$).[1, 84, 94, 100, 102, 104]

Magne *et al.* investigated the site-projected electronic structure of multi-layered (both HF-etched and HCl/LiF etched) $Ti_3C_2T_x$ by using a combination of TEM-EELS and DFT calculations. The electron energy-loss near edge structures (ELNES) at the carbon (C) and surface element (O or F) K edges are shown to be highly sensitive to the identity and location of the surface groups (Fig. 13b), and can be indirectly used to probe the Ti d density of states and subsequently the electronic properties (Fig. 13c). T_x groups were revealed to above the hollow sites of three neighbouring C atoms (C1) and not directly above the C atoms (C2) (Fig. 13a).[109]

Hui Pan theoretically calculated the electronic properties of transition metal nitride monolayers and their applicability as anode material for LIBs. Metallic and anti-ferromagnetic bare Ti_2N monolayers were predicted to have an open circuit voltage of 0.53 V

View Article Online
DOI: 10.1039/C6TA06772G

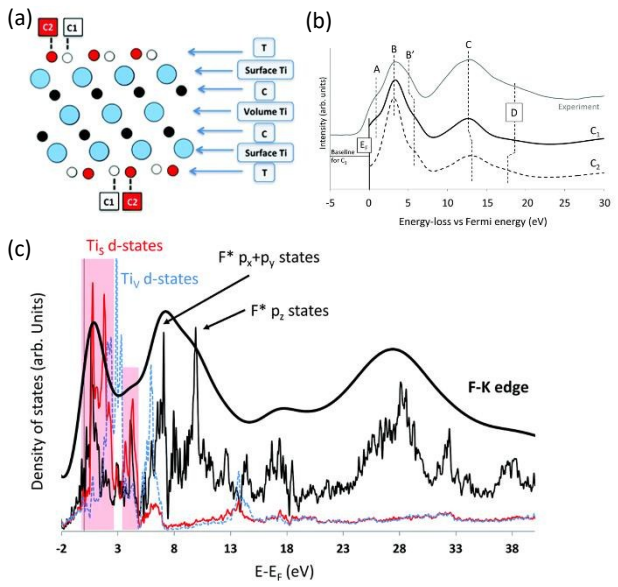

Fig. 13 (a) Side view of a $Ti_3C_2T_2$ single sheet with the two T surface group locations labelled C1 and C2. (b) Comparison between the experimental C-K edge and calculations performed considering the –OH group (T_x) in configurations C1 or C2. (c) Comparison between the simulated F-K edge in C1 (bold black line), the unoccupied p-DOS of the excited F atom (F* – thin black line), the surface titanium (Ti_s) d-DOS (red line) and the volume titanium (Ti_v) d-DOS (blue dashed line). The Ti_s and Ti_v DOS were divided by 500 and 250 respectively to be plotted on the same scale as the F* DOS [reprinted with permission from ref. 109. Copyright 2016 The Royal Society of Chemistry].

and a high specific capacity of 487 mAh g^{-1}, due to low adsorption energy and long bonding distance with Li atoms. Although –OH surface groups could reduce the diffusion barrier to 0.005 eV, unlike =O and –F terminations, the lithiation process required more effort for its positive adsorption energy and overall detrimental to its performance as anode. Additionally, other metallic $M_{n+1}N_n$ (M = Ta, Ti and V; n = 1 and 2) monolayers were computed and identified as non-magnetic with the exception of Ti_3N_2 being ferromagnetic.[110] More interestingly, according to computations by He *et al.*, Mn_2CF_2, a yet-to-be-synthesized but stable MXene was predicted to room-temperature ferromagnetism (high Curie temperature of 520 K), wide half-metallic gap (0.9 and 2.5 eV at PBE+U and HSE06 levels, respectively) and a substantial magnetic anisotropy (24 μeV) and its potential application in spintronics was highlighted by Hu *et al.*.[111, 112] Although various Cr_2XT_x have also been predicted to retain its ferromagnetism even with surface terminations unlike other MXenes, to date none of these MXenes have been experimentally synthesized and examined to verify the validity of the calculations.[100]

Experimentally, most MXenes are hitherto characterized to have inherent metallic behaviour except for a semiconducting oxygen-terminated Ti_2CO_x and Mo_2CT_x.[32, 67] Zhou *et al.*, using ab initio calculations, examined the electronic structures and electron transport properties of Ti_2CO_2 nanoribbons and revealed that the energy gaps in patterned (armchair- (Fig. 14a) and zigzag-terminated edges (Fig. 14b)) Ti_2CO_2 nanoribbons were tunable by appropriate crystallographic orientation and widths.[113] At width parameter beyond six, the armchair Ti_2CO_2 nanoribbons remain semiconducting (although band gaps decrease with increasing width of nanoribbons) (Fig. 14c), while zigzag nanoribbons become conducting (no or little band gaps) (Fig. 14d) and this is in accordance with previous calculations.[114] By combining nonequilibrium Green's function with DFT calculations, armchair and zigzag nanoribbon systems exhibit different current-voltage curves, with no onset bias for most of the zigzag nanoribbons. Nonlinear features and weak negative differential resistance behaviours were observed in some armchair and zigzag nanoribbon systems.

Zhang *et al.* computed the acoustic phonon limited carrier mobility of Ti_2CO_2 monolayers and nanoribbons by using DFT and deformation potential theory. The hole mobility along the *x* direction (10^4 cm^2 V^{-1}) was derived to be thrice as large as the value along the *y* direction, while the electron mobility was about two orders of magnitude lower (10^2 cm^2 V^{-1}). By controlling its width and engineering its edge, the Ti_2CO_2 nanoribbons, with drastic difference between the electron and hole mobility, were anticipated to be useful for photocatalysis and field-effect transistors.[115]

Different MXenes have been predicted with varying high in-plane elastic moduli.[85, 91] According to theoretical investigations by Fu *et al.*, the enhancement in strength by highly stabilising oxygen functional groups of $Ti_3C_2O_2$ was attributed to the charge transfer from inner Ti-C bonds to the external Ti-O surface bonds, hindering irreversible deformation and subsequently a high critical stress was needed for lattice failure.[116] Guo *et al.* studied the tensile stress-strain relations of $Ti_{n+1}C_n$ (n = 1, 2, or 3) and surface functionalized $Ti_{n+1}C_nT_x$ under different loading directions and unravelled the corresponding deformation mechanisms using first-principles calculations (Fig. 15a-b). Under biaxial and tensile strains, up to critical point, Ti–C bonds are gradually stretched resulting in stress induced strengthening; and beyond critical strain, the surface Ti layer

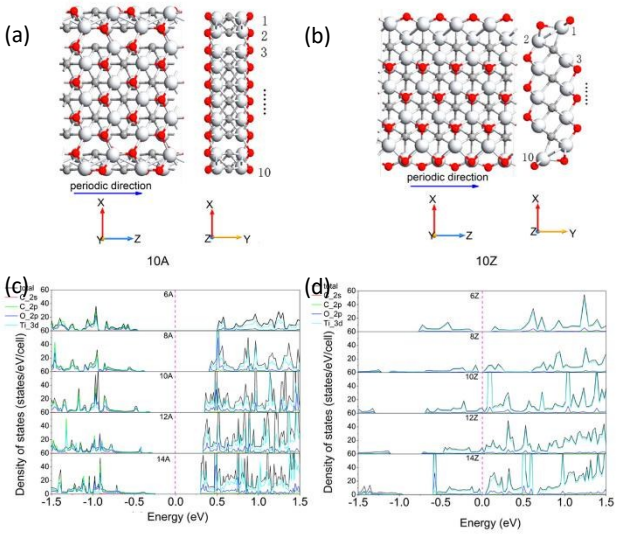

Fig. 14 Optimized atomic configurations of Ti_2CO_2 nanoribbons. (a) Top and side view of armchair Ti_2CO_2 nanoribbon monolayer with the width parameter of 10. (b) Top and side view of zigzag Ti_2CO_2 nanoribbon monolayer with the width parameter of 10. The red, gray and white circles represent O, C and, Ti atoms, respectively. Total density of states (TDOS) and projected density of states (PDOS) on atomic orbitals of Ti, C, and O atoms of (c) asymmetric armchair; and (d) zigzag Ti_2CO_2 nanoribbons, respectively. The Fermi energy is at zero [reprinted with permission from ref. 113. Copyright 2016 American Chemical Society].

View Article Online
DOI: 10.1039/C6TA06772G

abruptly collapses along the out-of-plane direction and is accompanied by shrinkage of Ti–C bonds and relaxation of stress (Fig. 15c-d). Importantly, surface functionalization (=O, –OH or –F) is observed to form covalent bonds with Ti (disappearance of lone pair electrons from Ti atoms) and enhance the mechanical flexibility of $Ti_{n+1}C_n$. Young's modulus of $Ti_{n+1}C_n$ is also observed to slightly decrease as n increases.[117]

Beyond the stable and superconductive (under 2.5 K) Mo_2C (> 100 μm) without surface functional groups prepared by Xu *et al.* through the traditional vapour deposition (CVD) method and the first Mo_2CT_x recently synthesized by Halim *et al.* as a potential Li-ion battery anode, most intrinsic physical properties of Mo_2CT_x remained unavailable.[32, 118] Computationally, Zha *et al.* predicted Mo_2CT_x to have more widespread of potential applications beyond high capacity anode material for it was found be nonmagnetic, possessed a high electrical conductivity (10^6 $\Omega^{-1}m^{-1}$), favourable thermal conductivity (48.4 Wm^{-1} K^{-1}), small thermal expansion coefficient (2.26×10^{-6} K^{-1}) and as well as high mechanical strength.[119, 120]

Aston *et al.* calculated the theoretical thermodynamic stability of 54 MXene compounds to streamline and identify yet-to-be-synthesized but stable MXenes. From a thermodynamic perspective, oxygenated transition metal nitrides such as $Ti_3N_2O_2$, $Ti_3N_3O_2$, $V_3N_2O_2$, $V_4N_3O_2$ and $Cr_4N_3O_2$ were predicted to be experimentally probable and six fluorinated Sc-based Mxenes ($Sc_{n+1}X_nF_2$) were expected to easily exfoliate and produce single layers.[121]

Theoretically, Ti_2CO_2, Hf_2CO_2, Zr_2CO_2, Sc_2CO_2, Sc_2CF_2 are predicted to possess indirect band gap while $Sc_2C(OH)_2$ is expected to have a small direct band gap.[100] Theoretical studies by L. Li, Khazaei *et al.*, and Si *et al.* indicated that $Mo_2Ti_2C_2O_2$ to be topological semiconductor.[122-124] Anasori *et al.*, using DFT calculations in conjunction with experimental data, predicted the controlled modifications to electronic properties (from metallic to semiconducting) of a subfamily of ordered layered double transition metals carbides ($M'_2M''C_2$ and $M'_2M''_2C_3$, where M' layers are sandwiched between M'' layers and the C atoms occupy the octahedral sites between them) may be achieved through surface terminations and choice of outer M' layers.[125]

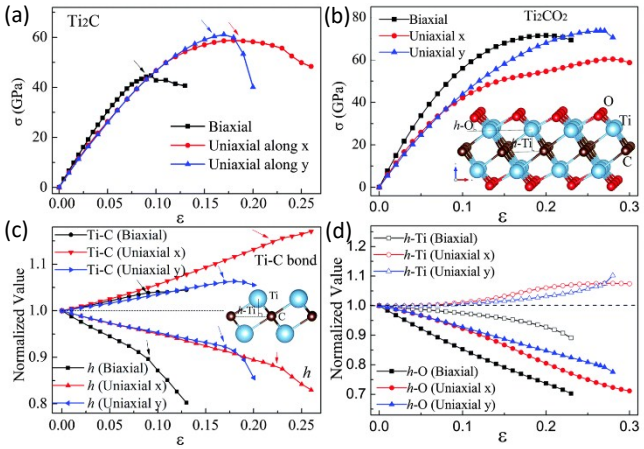

Fig. 15 Calculated stress–strain curves of (a) Ti_2C; and (b) Ti_2CO_2. (c) Variations of bond lengths (Ti–C) and the out-of-plane heights, h, of Ti atoms in Ti_2C. The arrows indicate the onset strains of instability. Inset shows atomic structure of Ti_2C. (d) Variations of the out-of-plane heights, h-Ti of Ti atoms in Ti_2CO_2 and the out-of-plane heights, h-O, of O atoms. Inset shows the atomic structure of Ti_2CO_2 wherein the surface groups are located at the most energetically favorable positions. Bond lengths and out-of-plane heights are normalized by their equilibrium values [reprinted with permission from ref. 117. Copyright 2015 The Royal Society of Chemistry].

Lee *et al.* and Ma *et al.* investigated and reported the possibility to hypothetically induce an indirect-to-direct band gap of Sc_2CO_2 with application of either a critical tensile strain or external electric field.[92, 96, 126] Using DFT tight-binding method, Zhang *et al.* examined the stability and electronic properties of Sc_2C monolayers, nanotubes and their functionalized counterparts. Sc_2CH_2 and $Sc_2C(OH)_2$ nanotubes were found to be stable and increasing so as their radii increased; semiconducting and with band gaps tunable by changing their radii.[127] Yang *et al.* identified that magnetic Sc_2CT_2 could be theoretically obtained through doping with Cr or Mn.[128]

More recently, Wang *et al.* proposed experimentally derived atomistic models that encompassed total neutron scattering and multilevel refinement methods, accounting for the coexistence and random surface groups (Fig. 16a-f) in certain MXenes, so as to improve the accuracy in predicting the properties of MXene from the existing idealized, limited, hypothetical and unrealistic models.[129] As most theoretical studies to date have been calculated based on single, isolated sheets, deviating from most experimentally obtained few-/multi-layered MXene flakes, ensuing models should also accommodate interlayer interactions such as van der Waals forces and hydrogen bonding for more realistic computations. It is also to be noted that although DFT calculations produce stable and consistent geometries, the computed electronic properties (whether metallic or narrowly-band semiconducting) are much dependent on the choice of the exchange-correlation functional.[130] As compared to

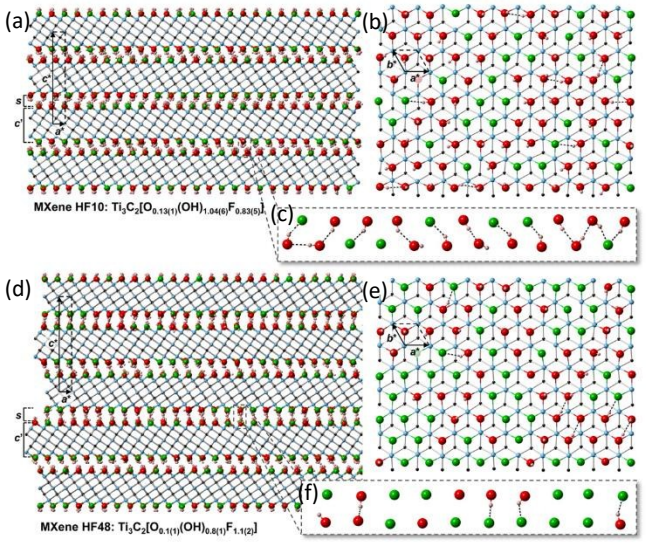

Fig. 16 Structural representation of (a-c) HF10 and (d-f) HF48 MXenes. The Ti, C, O, F, and H are in blue, black, red, green, and pink spheres, respectively. Hydrogen bonds are as black/white dashed lines for O···H and F···H. All other bonds are as solid lines. Plots (a) and (d) are viewed along the crystallographic *c** axis (i.e., the stacking direction). Plots (b) and (e) are top view (the *a**–*b** surface) of a single isolated sheet, illustrating random occupation of –O/OH/F groups. Plots (c) and (f) highlight the formation of interlayer hydrogen bonds (attractive force) and repulsive interactions when alike terminating atoms are facing each other. All hydrogen bonds shown in the plot are with the lengths of ≥1.5 Å and ≤2.3 Å [reprinted with permission from ref. 129. Copyright 2015 American Chemical Society].

View Article Online
DOI: 10.1039/C6TA06772G

Perdew-Burke-Ernzerhof (PDE) functional, Heyd-Scuseria-Eznzerhof (HSE06), a hybrid functional, was recommended to be included in calculations of electronic properties for more accurate band gap predictions.[97, 101]

These inherently complex MXenes, with nanocrystalline $M_{n+1}X_nT_x$ layers, short-range ordering of surface structure and randomly stacked monolayers, have shown immerse potential applications as transparent conductive films, environmental remediation, electromagnetic interference (EMI) absorption and shielding, electrochemical applications, such as Li-ion batteries (LIBs), supercapacitors, other electrochemical storage systems and electrocatalysts. Other prospective applications, include hydrogen storage media (using Sc_2C, Ti_2C, V_2C and Cr_2C), NH_3 electrosynthesis (using V_3C_2 and Nb_3C_2), and additives for tribological studies are however still in their hypothetical or infancy stage will not be covered in this review.[79, 88, 89, 131-136]

3.1 Transparent conductive films

Berdiyorov *et al.* theoretically derived the isolated effect of each individual surface termination group on dielectric and optical properties of $Ti_3C_2T_x$. Generally, the different surface groups were observed to similarly decrease the static dielectric function and increase ultraviolet reflectivity of $Ti_3C_2T_x$ than that of pristine Ti_3C_2, though, in the visible range, only –F and –OH demonstrated lower absorption and reflectivity than pristine Ti_3C_2.[105]

Halim *et al.* first demonstrated the potential application of MXenes as transparent conductive electrodes, by using a transparent (85 % transmittance) and highly conductive intercalated $Ti_3C_2T_x$ thin film (19 nm) that was prepared by chemically etching a magnetron-sputtered Ti_3AlC_2 with NH_4HF_2 solution at RT.[25] However, it is not scalable due to the high cost and small quantity of magnetron-sputtered films.

Dillon *et al.* reported a low cost and scalable fabrication method to prepare continuous, optically transparent (Fig. 17a) and highly in-plane conductive (bulk conductivity = 6500 S cm^{-1}) $Ti_3C_2T_x$ thin films (Fig. 17b) by spin-casting, the basal planes of individual $Ti_3C_2T_x$ flakes showed a high degree of alignment, parallel to the substrate as reflected by the high intensity of *002* XRD peak at 7.1 °. Stability and performance of these $Ti_3C_2T_x$ thin films in ambient atmosphere are still a work in progress though, since their conductance was degraded rather quickly by a factor of three when exposed to either O_2 or moisture albeit retaining their good transmittance.[137]

More recently, Hantanasirisakul *et al.* fabricated homogeneous, transparent conductive $Ti_3C_2T_x$ thin films by using spray coating from colloidal HCl/LiF etched $Ti_3C_2T_x$ on various substrates (Fig. 17c). As revealed by the measurement of ultraviolet-visible (UV-vis) spectrophotometry, a comparatively thick $Ti_3C_2T_x$ film of 70 nm still retained 44 % transmittance in the visible region while a thin $Ti_3C_2T_x$ film had a transmittance of as high as 91%. Intuitively, a trade-off between transparency and conductivity exists in terms of the film thickness. Although the changes in transmittance are yet to be fully understood and insignificant to be practically applied, reversible changes of %T during electrochemical intercalation/deintercalation of $Ti_3C_2T_x$ films (Fig. 17d), suggested potential application in sensors and electrochromic applications.[138]

Mariano *et al.* detailed the increment of superimposed $Ti_3C_2T_x$ flakes with reduction of spin casting rate, i.e. 800 rpm produced a 3 flake overlap, 600 rpm gave a 4 flake overlap and 400 rpm resulted in a 5 flake overlap. It was noted that with additional overlapping layers may help to improve the interconnectivity between nanosheets while retaining high VIS-NIR region transmission, as evidenced by the low sheet resistance of 437 Ω sq^{-1}, high 77 %T for films (5 flake overlap, 7.4 ± 0.5 nm) deposited at 400 rpm. Thicker films were found to be less drastically impacted by oxidation and remained stable in air over two months. By annealing the films between 100 °C and 200 °C, sheet resistance was further decreased due to the removal of any remnant adsorbed water, intercalated species on and within $Ti_3C_2T_x$ layers, however at temperature beyond 250 °C, the films began to oxidize and sheet resistance reverted to its initial values.[139]

Ali *et al.* fabricated conductive and transparent thin films of $Ti_3C_2T_x$ using EDHA, a scalable electrospray technique which involved deposition of solution in the absence of a vacuum under the influence of an electric field at ambient temperature.

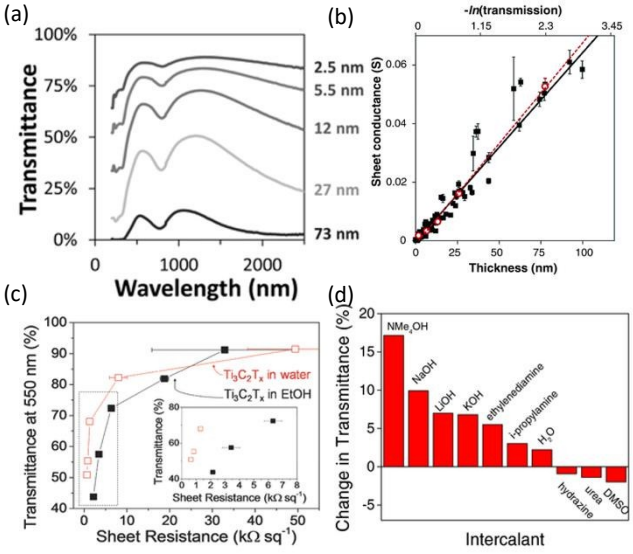

Fig. 17 (a) UV-vis-NIR transmittance spectra of spincast $Ti_3C_2T_x$ film with varying thickness. (b) Sheet conductance vs. film thickness (lower *x*-axis) and ln (transmittance) (upper *x*-axis) of spincast $Ti_3C_2T_x$ films. Red circles represent thickness of $Ti_3C_2T_x$ film deposited on Si-SiO_2 substrate as measured by AFM; dashed red line is the linear fit with slope σ = 6600 S cm^{-1}. Black solid squares represent thickness of $Ti_3C_2T_x$ film deposited on glass, quartz and polyetherimide, derived from measured transmittance; black line is the linear fit to the data points of derived thickness with slope σ = 6500 ± 800 S cm^{-1} [reprinted with permission from ref. 137. Copyright 2016 John Wiley & Sons, Inc.]. (c) Sheet resistance vs. transmittance at 550 nm of $Ti_3C_2T_x$ sprayed from ethanol and water solutions. Inset shows the low sheet resistance region. (d) Change in %T of $Ti_3C_2T_x$ films due to chemical intercalation (positive change indicates an increase in %T as compared to pristine $Ti_3C_2T_x$ films [reprinted with permission from ref. 138. Copyright 2016 John Wiley & Sons, Inc.].

View Article Online
DOI: 10.1039/C6TA06772G

A low resistivity of 3.4×10^{-4} Ω cm and ca. 86.7 %T was recorded for a 135 nm $Ti_3C_2T_x$ thin film.[140]

Aïssa *et al.* reported to exhibit a similarly low resistivity of ca. 3.4×10^{-4} Ω cm for an electrosprayed thin film of $Ti_3C_2T_x$ (250 nm thick on a glass substrate), even lower than that of an indium tin oxide (ITO) thin film of identical thickness. More significantly, with a mere 0.25 wt. % of graphene incorporated, the measured conductivity and Hall mobility doubled and tripled respectively. An optimized 30-fold reduction in resistivity as compared to its electrosprayed pristine $Ti_3C_2T_x$ counterpart was achieved by incorporating a low content of 2.5 wt. % graphene (indicative of a low electrical percolation threshold) to form a binary, fully percolated composite.[54] This markedly improved electrical conductivity (9.5×10^4 S cm^{-1}) is attributed to filling up and smoothening of HF-etched $Ti_3C_2T_x$ inherent defects (such as nanopores which acted as resistance for electron flow) by graphene deposition, as observed under SEM and AFM. The formation of a cross-linked and electrically conductive network of graphene within the film that provides additional interconnecting path throughout the composite for more electrons flow and probable alignment of graphene flakes through interaction with $Ti_3C_2T_x$ surface, especially so in low graphene content (< 0.5 wt. %).

Lipatov *et al.* fabricated field-effect transistors (FETs) with large HCl/LiF etched $Ti_3C_2T_x$ monolayer flakes (using 7.5:1 molar ratio of LiF to Ti_3AlC_2) as conductive channels, by first drop-casting diluted colloidal solution of delaminated HCl/LiF etched $Ti_3C_2T_x$ onto a Si/SiO_2 substrate, followed e-beam lithography for device patterning and e-beam evaporation for the deposition of 3 nm Cr and 20 nm Au as metal contacts. The average resistivity and field-effect electron mobility of 10 similarly fabricated devices under vacuum were respectively measured to be 2310 ± 570 Ω □$^{-1}$ and 2.6 ± 0.7 cm2 V^{-1} s^{-1}. The resistivity of a $Ti_3C_2T_x$ single layer (ca. 1 nm) was thus calculated to be 2.31 ± 0.57 μΩ.m (4600 ± 1100 S cm^{-1}). Sheet resistivity of bulk HCl/LiF etched $Ti_3C_2T_x$ film (ca. 9 μm thick) was measured to be 15.8 ± 1.3 μΩ.m via van der Paw method.[42] The small difference of within one order of magnitude between resistivity of a single $Ti_3C_2T_x$ monolayer and that of a $Ti_3C_2T_x$ film, was consistent with the reported resistance anisotropy in an earlier theoretical prediction and in situ experimental work by Hu *et al.* and implied decent inter-flake conductance through the surface functional groups.[141] Environmental degradation and decrease in the conductivity of the devices in humid air were caused by p-doping due to electron accepting adsorbates such as oxygen and water molecules and oxidation at the edges of $Ti_3C_2T_x$ flakes.

3.2 Environmental remediation

Mashtalir *et al.* first demonstrated that negatively surface charged $Ti_3C_2T_x$ could be used to remove a cationic dye, methylene blue (MB), from solution in dark, due to favourable adsorption (Fig. 18a). Under ultraviolet (UV) irradiation, in the presence of the HF-etched multi-layered $Ti_3C_2T_x$, both MB and an anionic dye, acid blue 80 (AB80), were observed to undergo rapid photodegradation, suggesting the presence of possible complex processes, such as selective adsorption, degradation of various molecules and catalysing reactions. It was also found that the as-synthesized $Ti_3C_2T_x$ was not stable in water, especially in the presence of O_2, because they could be partially oxidized to form TiO_2, thus requiring more work to address this issue.[46]

Using photodegradation of methyl orange under UV irradiation as a representative model, Gao *et al.* assessed that a hydrothermally synthesized $TiO_2/Ti_3C_2T_x$ nanocomposite possessed enhanced photocatalytic activity (electron-hole separation) as compared with pure anatase TiO_2 or HF-etched $Ti_3C_2T_x$. Due to the presence of heterojunction in $TiO_2/Ti_3C_2T_x$, this composite could be suitable for applications in purification of contaminated water or air.[69]

Peng *et al.* elucidated the preferential reversible adsorption of lead ions (Pb^{2+}) from a solution with effluent contents below 2 μg L^{-1}, as well as high level Ca^{2+} and Mg^{2+}, by using HF-etched multi-layered $Ti_3C_2T_x$ treated with alkalization intercalation. The sequestration of heavy metal pollutant is enhanced by cation (Na^+) substitution for the –OH groups, thus forming active sites favourable for ion-exchange. It is anticipated that the exhausted materials could be efficiently regenerated.[81] Based on first-principles calculations, this group further elucidated the adsorption mechanism as heavy-metal ions being trapped within hydroxyl potential traps (with sufficient opposite-spin electron pairs) and examined the effect of different hydroxyl

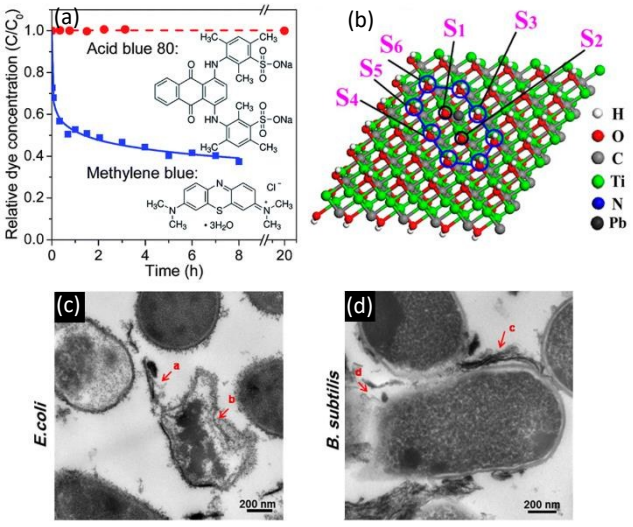

Fig. 18 (a) Time dependence of MB (C_0 = 0.05 mg mL^{-1}) and AB80 (C_0 = 0.06 mg mL^{-1}) concentrations in aqueous $Ti_3C_2T_x$ suspensions in the absence of light [reprinted with permission from ref. 46. Copyright 2014 The Royal Society of Chemistry]. (b) Schematic of hydroxyl trap, top view of $Ti_3C_2(O_2H_{2-2m}Pb_m)$ structure when Pb coverage is 1/9 ML. S_1–S_6 represent the different atom sites of the hydroxyl [reprinted with permission from ref. 142. Copyright 2015 American Chemical Society]. TEM images of (c) *E. coli* and (d) *B. subtilis* treated with 200 μg/mL of $Ti_3C_2T_x$ for 4 h. The cell wall stripped down after exposure to $Ti_3C_2T_x$ nanosheets (red arrows b, d), $Ti_3C_2T_x$ nanosheets tightly adsorbed around the cells and entered the cells (red arrows a, c). The intracellular densities of both cells decreased and $Ti_3C_2T_x$ attached to the cellular membrane of both bacteria (red arrows b, d) [reprinted with permission from ref. 147. Copyright 2016 American Chemical Society].

View Article Online
DOI: 10.1039/C6TA08772G

sites (Fig. 18b), different functional groups on the adsorption behaviour thus extending intercalated $Ti_3C_2(OH)_2$'s applicability to adsorb other heavy metal.[142]

Ying *et al.* observed simultaneous reduction of Cr (VI) to Cr (III) and adsorption of Cr (III) at pH 5.0, as well as reduction of other oxidant agents such as $K_3[FeCN]_6$, $KMnO_4$ and $NaAuCl_4$ by delaminated HF-etched $Ti_3C_2T_x$ nanosheets. Additionally, its reducing activity in aqueous solution was reaffirmed by the observation that white rutile TiO_2 nanoparticles were slowly precipitated from black delaminated $Ti_3C_2T_x$ aqueous dispersion over the course of 3 months under atmospheric conditions.[143] Consequently, these dispersions, containing high surface area $Ti_3C_2T_x$ nanosheets, are promising candidates for efficient removal of high valence toxic metal compound from industrial wastewater.

Similarly, a sandwich-like, magnetic $Ti_3C_2T_x/Fe_3O_4/Fe_2O_3$ composite was prepared by Zhang *et al.* for phosphate removal by exploiting its sorption selectivity with both Ti-O and Ti-F surface terminations, readily forming Ti-O-P complexes across a wide acidic pH range of 2.5 to 6.0.[74] Nanosized Fe_2O_3 intercalated between the HF-etched $Ti_3C_2T_x$ layers, increased available surface area for reaction and the surface embedded magnetic Fe_3O_4 would be responsible for the effective separation. It is expected that the separation kinetics could greatly enhance, when an industrial magnetic field is applied. Additionally, the exhausted $Ti_3C_2T_x/Fe_3O_4/Fe_2O_3$ can be readily regenerated in binary alkaline brine solutions.

Wang *et al.* experimented with multi-layered HF-etched V_2CT_x as a potential and efficient adsorbent for the capture of radionuclide, uranium (U(VI)), with a high normalized U(UI) adsorption capacity at 256 mg g^{-1} over pH range of 3.0 to 5.0. Encouragingly, these multi-layered V_2CT_x with adsorbed U(VI) could be regenerated when exposed in highly acidic (pH < 3) solutions. Based on DFT calculations and extended X-ray absorption fine structure (EXAFS) results, the preferential adsorption of uranyl ions by –OH bonded to V of the V_2CT_x layers suggested the work of an ion-exchange mechanism.[144]

Chang *et al.* vacuum filtrated dilute suspensions of HCl/LiF etched $Ti_3C_2T_x$ (0.01 mg/ mL) to fabricate membranes of thicknesses 1.5 ± 0.1 µm with water flux ca. 38 L/ (Bar.h.m^2) on commercial polyvinylidene fluoride (PVDF) supports. It was distinctively observed that HCl/LiF etched $Ti_3C_2T_x$ membranes exhibited better selectivity, than graphene oxide membranes, towards small (<4.5 Å) metal cations with increasing charges from +2 to +4, under similar testing conditions, with single-charged cations having an order of magnitude faster permeation of water as compared to multiple-charged cations. It was explained that single-charged and small radii (< 6.4 Å) cations (Li^+, Na^+, K^+) capably penetrated between $Ti_3C_2T_x$ interlayers and adsorption of ions on both sides of $Ti_3C_2T_x$ formed electric double layer on the surface of each individual flake and subsequently led to repulsion of the sheets which enabled higher permeation rates. For multiple-charged cations (Mg^{2+}, Ca^{2+}, Al^{3+}), beyond an initial increment of the $Ti_3C_2T_x$ interlayer distances, as more of such multi-charged ions were intercalated, the electrostatic attraction between the negatively charged $Ti_3C_2T_x$ and highly charged cations shrank the interlayer distances instead, and reduced permeation rates. Intuitively, bulky MB^+ dye ions (> 6.4 Å) were excluded by these $Ti_3C_2T_x$ membranes because they are too large to pass through.[145] From DFT calculations, Berdiyorov *et al.* explained the origin of ionic selectivity to be from the variation of energy barriers for ions of different charge to be intercalated between the layers.[146]

Additionally, Rasool *et al.* evaluated the suitability and applicability of such $Ti_3C_2T_x$ membranes for ion separation, water purification, antimicrobial coatings and related applications, through the investigations of their interaction mechanisms and bactericidal activity in two bacterial models (Fig. 18 c-d). Its negatively charged surfaces, high hydrophilicity, hydrogen bonding between oxygenate groups have been suggested to be the contributing factors towards the strong antibacterial behaviour observed. However, the exact antibacterial mechanism is yet to be fully understood.[147]

Smith *et al.* first proposed, conceptualized and theoretically simulated the use of symmetric Na-ion intercalation electrodes separated by Na-blocking membrane to desalinate NaCl from water.[148] Most recently, Srimuk *et al.* demonstrated the first use of HF-etched multi-layered $Ti_3C_2T_x$ as a novel intercalation electrode for desalination via capacitive deionization (CDI). Tapping into its exceptional pseudocapacitance, a CDI cell, with both electrodes based on drop-casted HF-etched multi-layered $Ti_3C_2T_x$ onto commercial porous separator, was set up and evaluated to have an average salt adsorption capacity of 13 ± 2 mg/g over 30 CDI cycles.[149] Beyond carbonaceous materials and ion immobilization via double layer formation, ion intercalation into the layered $Ti_3C_2T_x$ structure presents itself as an alternative towards enhanced electrochemical desalination.

3.3 Electromagnetic interference (EMI) absorption and shielding

Qing *et al.* first explored the use of HF-etched multi-layered $Ti_3C_2T_x$ as fillers (50 wt. %) to an epoxy composite of 1.4 mm thickness and achieved a low reflection loss (RL) of – 11 dB (excellent microwave absorption performance exceeding 92%) over the frequency range of 12.4 — 18 GHz. It was proposed that the presence of surface functional groups, intrinsic defects and dangling bonds of HF-etched $Ti_3C_2T_x$ and the numerous interfaces between $Ti_3C_2T_x$ and epoxy matrix, resulted in more electron relaxation polarization and interfacial polarization under an alternating electrical field and thus contributed significantly towards dielectric loss.[150]

Han *et al.* investigated the post-etching heat treatment of $Ti_3C_2T_x$ and its related surface structural change and influence on its dielectric properties and EM wave absorption performance (Fig. 19a). The removal of Al layers through HF-etching was reaffirmed to lead to a significant enhancement of complex permittivity because of the surface functional groups and improved electrical conductivity. Rapid annealing of HF-etched multi-layered $Ti_3C_2T_x$ at 800 °C for 2 h in argon with a heating rate of 10 °C/min resulted in the oxidation of the surface Ti layers to form localized sandwich structure of anatase and rutile TiO_2 nanoparticles and amorphous carbon sheets supported by the layered $Ti_3C_2T_x$ flakes. The decrease in hydroxyl groups and formation of amorphous carbon improved the electronic conductivity, and coupled with the formation of capacitor-like

View Article Online
DOI: 10.1039/C6TA06772G

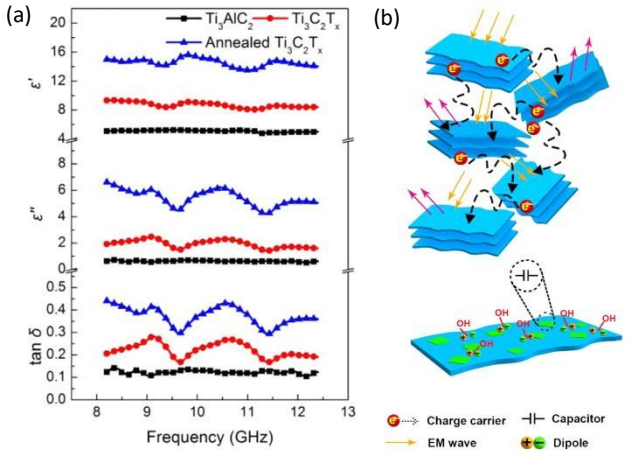

Fig. 19 (a) Permittivity (real (ε′) and imaginary (ε″) and the loss tangent (tan δ) versus frequency for composites of the Ti_3AlC_2 MAX phase, $Ti_3C_2T_x$, and annealed $Ti_3C_2T_x$ in a wax matrix with 50 wt % loading. (b) Schematic for Proposed EMI shielding mechanism. Incoming EM waves (orange arrows) strike the surface of a MXene flake. Because reflection occurs before absorption, part of the EM waves is immediately reflected from the surface owing to many charge carriers from the highly conducting surface (magenta arrows), whereas induced local dipoles, resulting from termination groups, help with absorption of the incident waves passing through the MXene structure. Transmitted waves with less energy are then subjected to the same process when they encounter the next MXene flake, giving rise to multiple internal reflections (dashed black arrows), as well as more absorption. Each time an EM wave is transmitted through a MXene flake, its intensity is substantially decreased, resulting in an overall attenuated or eliminated EM wave [reprinted with permission from ref. 151. Copyright 2016 American Chemical Society].

structures by amorphous carbon and low permittivity anatase and rutile TiO_2, dielectric dipole interactions and accompanying relaxation at these multiple interfaces enhanced the dissipation of the EM wave. A minimum reflection coefficient of -48.4 dB at 11.6 GHz was attained by a 50 wt. % annealed $Ti_3C_2T_x$/wax composite of 1.7 mm thickness. Contrary to EM absorbing materials, increased loading of $Ti_3C_2T_x$ (between 60 wt. % to 90 wt. %) in wax composites were also examined for their EMI shielding performance. Counterintuitively, majority of the total shielding effectiveness (SE) of $Ti_3C_2T_x$/wax composites was contributed by EM wave absorption and not EM wave reflection (Fig. 19b) even though $Ti_3C_2T_x$ possessed metal-like free electron density.[151]

Shahzad *et al.* adopted a higher LiF to Ti_3AlC_2 molar ratio (7.5 to 1) to prepare delaminated $Ti_3C_2T_x$ without sonication and films of these pristine HCl/LiF-derived delaminated $Ti_3C_2T_x$ and its composite with 10 wt. % sodium alginate (SA) at recorded exceptional EMI SE performance at 92 (45 µm thickness) and 57 dB (8 µm thickness) respectively. It was proposed that in addition to polarization losses from the induced dipoles by the surface terminations, the abundance of $Ti_3C_2T_x$ surface free electrons partially reflected some incident EM waves, the high electron density $Ti_3C_2T_x$ absorbed and caused a decrease in energy of the remaining waves due to ohmic losses and the 2D nanolamellar structure of $Ti_3C_2T_x$ provided the necessary reflecting surfaces for internal multiple reflection phenomenon that scattered EM waves and dissipated energy in the form of heat. Unprecedentedly, this 90 wt. % $Ti_3C_2T_x$-SA composite encompasses many desirable properties for commercialization such as high EMI SE at 57 dB, low density of 2.31 g cm^{-3}, low thickness of 8 µm, oxidation resistance, high flexibility and ease of processing.[41]

Evidently, even though this three EMI shielding with MXenes similarly involved $Ti_3C_2T_x$, the variances in synthesis conditions resulted in fundamentally different $Ti_3C_2T_x$, in terms of the degree of exfoliation and delamination (number of atomic layers) and the proportion of surface terminations, and consequently EMI absorption or shielding performance. More interestingly, surface modification to the MXene, use of other members in the MXenes family or MXene-based composites remains a promising possibility to be further explored.

3.4 Energy storage

3.4.1 Lithium-ion batteries (LIBs). LIBs, as a ubiquitous cornerstone of portable consumer electronic era and de facto front-runner incorporated in commercial battery packs for electric vehicles (EVs), are still limited in terms of energy density, due to the incumbent commercial graphite anodes. MXenes are promising LIB anode materials, since they have excellent electronic conductivity, low operating voltage range of (-0.2 to 0.6 V vs. Li/Li^+), low diffusion barriers which are favourable for high rate performance and exceptional mechanical properties that are invariant to Li adsorption. Unlike typical diffusion limited battery electrode materials, intercalation of ions in MXenes can paradoxically occur at a high rate, without significantly depreciating their energy storage capacities. Levi *et al.* explained that the rapid electrochemical cationic intercalation between partially swollen MXene layers, resembling ion adsorption at the solid-liquid interface, was facilitated by the presence of water molecules and resulted in significant structural deformation (expansion and contraction). It was conjectured that this electrochemical capacitive paradox was made possible by the presence of both shallow and deep cationic adsorption sites, filled with ions and water molecules.[152] As mentioned earlier, MXene sheets with more =O terminations are suggested to possess the highest capacity as compared to other surface groups.[102, 104] It seems that HCl/LiF etching may be the most preferred method to prepare MXenes for LIBs although it has a relatively lower yield and controlling surface chemistry of MXenes can be pivotal to performance enhancement.[37, 94, 99]

Based on DFT calculations, Tang *et al.* predicted a high theoretical Li-ion capacity of 320 mAh g^{-1} for a hypothetically bare Ti_3C_2 monolayer whereas if fully terminated by either –OH or –F, a drastically reduced theoretical capacity of 67 or 130 mAh g^{-1} would be obtained instead.[97] Based on X-ray Absorption Near Edge Structure (XANES) data, Xie *et al.* proposed the formation of extra Li layers on the already-lithiated O-terminated Ti_3C_2 to account for the exceptional capacity of 410 mAh g^{-1}, as reported by Mashtalir *et al.* for a DMSO-intercalated HF-etched $Ti_3C_2T_x$, which exceeded its theoretical capacity (320 mAh g^{-1}).[31, 102] Eames *et al.*, in a later DFT study, reaffirmed surface termination by oxygen (=O) presented the highest capacity than those terminated by either –OH or –F.[104] Xie *et al.* and Er *et al.* had separately conducted ab initio DFT calculations to derive the theoretical lithium and sodium capacity of $Ti_3C_2T_x$, and it was noted that storage capacities were enhanced by larger

interlayer distance.[87, 99] Zhao et al. assessed the influences of strain and Li concentration on Li-ion storage capacity of Ti_2C and reported that the low diffusion barriers (favourable for good rate performance) remained invariant under high strain or Li concentration and only binding energy of Li (related to stability) slightly lowered under high strain.[103] The diffusion barriers of bilayer structure of oxygen-functionalized Ti- and V- based carbide MXenes, as computed by Ashton *et al.*, were significantly higher than that of corresponding monolayers, thus reiterating the importance of having dispersed MXene single layers to attain high LIBs anode performance.[153]

Encouraged by the first application of HF-etched multi-layered Ti_2CT_x as anode material in LIBs, where a reversible capacity of 70 mAh g^{-1} was recorded even after 200 cycles at 10 C in a half-cell configuration, other MXene materials, such as $Ti_3C_2T_x$, $Mo_2TiC_2T_x$, Nb_2CT_x, V_2CT_x, $Nb_4C_3T_x$, and Mo_2CT_x, have also been examined as potential anode for LIBs.[15, 17, 31, 32, 63, 154] By combination with transition metal oxides (TMOs) which have higher Li^+ capacity but poor conductivity, synergistic effect of TMO and Ti_2CT_x leads to much improved performance (Fig. 20a) as compared with either individual TMO or Ti_2CT_x.[68, 155]

Mashtalir *et al.* prepared a mixture of narrow sized distributed single and few-layered $Ti_3C_2T_x$ by intercalation of DMSO between the HF-etched multi-layered $Ti_3C_2T_x$ at RT for 18 h under constant stirring, followed by sonication in DI water for 6 h. A free-standing, binder-free $Ti_3C_2T_x$ electrode was then assembled by filtering the mixture through a membrane. Reportedly, this $Ti_3C_2T_x$ electrode demonstrated excellent rate performance of 410 mAh g^{-1} at 1 C and 110 mAh g^{-1} at 36 C, both after 700 cycles. This elucidated the possible formation of additional Li layers on the already lithiated and surface terminated $Ti_3C_2T_x$, resulting in capacity exceeding the theoretical value.[31] Despite its inherent moderate gravimetric capacity (320 mAh g^{-1}), Kim *et al.* showed that by cold-pressing HF-etched multi-layered $Ti_3C_2T_x$ with conductive agent, carbon black (CB), a high-density and practical $Ti_3C_2T_x$ electrode with an areal capacity of 5.9 mAh cm^{-2} at C/3 exceeding that of commercial graphite anodes could be achieved.[156]

In bid to improve the electronic conductivity between layers of HF-etched $Ti_3C_2T_x$ sheets, reduced contact resistance amongst the sheets and increase ion accessibility by preventing restacking, Lin *et al.* grew conductive CNFs to connect the isolated layers. Consequently, this 86.2 wt. % $Ti_3C_2T_x$/CNFs retained a reversible capacity of 320 mAh g^{-1} at 1 C after 300 cycles and 97 mAh g^{-1} at 100 C even after 2900 cycles (Fig. 20b).[58] Alternatively, Ren *et al.* improved ion accessibility by synthesizing porous $Ti_3C_2T_x$ flakes and by incorporating 10 wt. % of MWCNTs as interlayer spacers and conductive agent, the as-prepared porous $Ti_3C_2T_x$/MWCNTs retained reversible capacity of 800 mAh g^{-1} at 160 mA g^{-1} after 350 cycles. This exceptional reversible capacity is presumed to be consequential of more adsorption and storage of Li^+ ions on the edges of pores in this porous $Ti_3C_2T_x$/MWCNTs composite.[75] Zou *et al.* synthesized a 90 wt.% HF-etched Ti_3C_2/Ag composite, by reducing $AgNO_3$ in the presence of $Ti_3C_2T_x$. The formation of well-dispersed Ag nanoparticles on the layered $Ti_3C_2T_x$ improved its overall

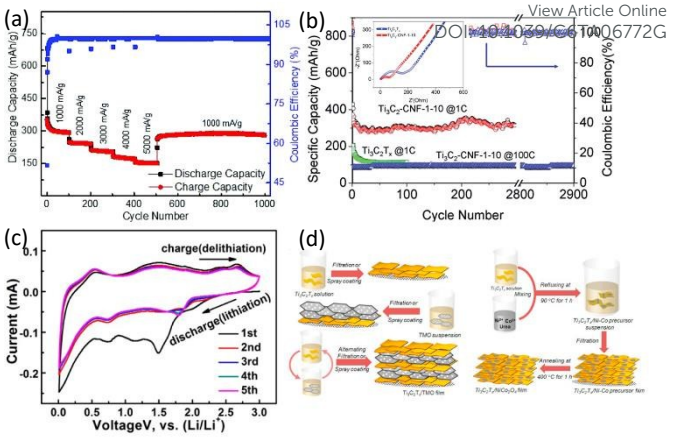

Fig. 20 (a) Rate performance of TiO_2/Ti_2CT_x hybrid obtained by partially oxidizing Ti_2CT_x with H_2O_2 (ca. 5 minutes of contact time) at various current densities [reprinted with permission from ref. 68. Copyright 2016 The Royal Society of Chemistry]. (b) Cycling stability of $Ti_3C_2T_x$ at 1 C and the $Ti_3C_2T_x$/CNFs composite at 1 C and 100 C. Inset shows the electrochemical impedance spectroscopy (EIS) plots of $Ti_3C_2T_x$ and $Ti_3C_2T_x$/CNFs composite [reprinted with permission from ref. 58. Copyright 2015 The Royal Society of Chemistry]. (c) CV curves of PVP-Sn^{4+}@$Ti_3C_2T_x$ at a scan rate of 0.1 mV s^{-1} [reprinted with permission from ref. 59. Copyright 2016 American Chemical Society]. (d) Schematics of synthesis processes for the fabrication of free-standing and flexible $Ti_3C_2T_x$/TMO hybrid films through sandwich-like assembly by alternating filtration or spray coating methods or an in-situ growth method [reprinted with permission from ref. 157. Copyright 2016 Elsevier].

electrical conductivity. This composite electrode recorded a reversible capacity of 310 mAh g^{-1} at 1 C (320 mA g^{-1}) after 800 cycles, 260 mAh g^{-1} at 10 C after 1000 cycles and 150 mAh g^{-1} at 50 C after 5000 cycles. It was inferred that the Ag species had important catalytic roles for the increase of more efficient and conductive Ti (III) species from Ti (II) species in Ti_3C_2/Ag composite after 2000 cycles (discharge-charge), whereas a pristine $Ti_3C_2T_x$ displayed negligible Ti species variation after cycling.[78]

To overcome its inherent moderate gravimetric capacity, Luo *et al.* synthesized a PVP-Sn^{4+}@$Ti_3C_2T_x$ nanocomposite, which exhibited a synergistic "pillar effect", whereby spontaneous expansion of anchored Sn when alloying with Li^+, concurrently pushed the $Ti_3C_2T_x$ interlayers further apart to allow more Li^+ intercalation and when tested in a half-cell configuration, it retained reversible capacity of 544 mAh g^{-1} at 500 mA g^{-1} after 200 cycles.[59] However, it is also noted that the charge-discharge profiles of $Ti_3C_2T_x$ resemble more of supercapacitors than that of LIBs (Fig. 20c), thus it is noteworthy that they may be more compatible in Li-ion capacitors or hybrid devices instead. Zhao *et al.* prepared freestanding delaminated HCl/LiF etched $Ti_3C_2T_x$/planar $NiCo_2O_4$ composite film using three different methods, namely alternating filtration, spray coating and an in-situ growth process (Fig. 20d). The former two methods offered the flexibility to fabricate the hybrid films with different mass ratios of $NiCo_2O_4$ to $Ti_3C_2T_x$ and it was noted that the mechanical properties deteriorate with increasing $NiCo_2O_4$ content. The in-situ growth process, probably catalysed by Ni and Co cations, induced partial oxidation of $Ti_3C_2T_x$ flakes and

View Article Online
DOI: 10.1039/C6TA08772G

resulted in a comparatively reduced conductivity of the hybrid film. It was established that the activated (through pre-cycling at low rates) spray-coated 50 wt. % $Ti_3C_2T_x$/planar $NiCo_2O_4$ hybrid film (3 µm) displayed the best performance amongst the threes samples as it retained a reversible capacity of ca. 1010 mAh g^{-1} at 1 C after 100 cycles. This performance was attributed to better electrolyte penetration with a higher degree of disorder in arrangement of $Ti_3C_2T_x$ and planer $NiCo_2O_4$ nanoflakes within the film due to spray coating and a large amount of $Ti_3C_2T_x$ (50 wt.%) to facilitate fast electron and ion transfer.[157]

The next most studied MXene after $Ti_3C_2T_x$ is Nb_2CT_x, whereby Naguib *et al.* first demonstrated HF-etched multi-layered Nb_2CT_x's prospect as anode of LIBs as it maintained a reversible capacity of 170 mAh g^{-1} at 1 C, 110 mAh g^{-1} at 10 C; both after 150 cycles.[15] Mashtalir *et al.*, in the same study that reported i-PrA as intercalant to assist in delaminating HF-etched multi-layered Nb_2CT_x, prepared a flexible and free-standing 90 wt. % Nb_2CT_x/MWCNTs composite, which exhibited an unprecedented capacity of 220 mAh g^{-1} at 10 C after 100 cycles.[47] Similar to that of the high-density $Ti_3C_2T_x$ electrode, by cold-pressing HF-etched multi-layered Nb_2CT_x with CB, Kim *et al.* prepared a practical Nb_2CT_x electrode with even higher areal capacity of 6.7 mAh cm^{-2} at C/3.[156] Although Nb_2CT_x anode performance for LIBs, in terms of reversible capacity and high rate performance, is promising, the observed sloping/linear charge-discharge profiles over a large potential range resembles more of electrochemical behaviour of a capacitor than a battery. Byeon *et al.* assembled and tested three prototypical hybrid cells using Nb_2CT_x as either a cathode or an anode and both in a symmetrical setup.[158]

As an experimental LIB anode material, HF-etched multi-layered V_2CT_x displayed a reversible capacity of 210 to 260 mAh g^{-1} at 1 C, 125 mAh g^{-1} at 10 C; both after 150 cycles. However, its appeal as a prospective anode material was greatly diminished for its requirement of high lithiation voltage.[15] A synergistic composite of orthorhombic Nb_2O_5 nanoparticles with $Nb_4C_3T_x$ and amorphous carbon as synthesized by Zhang *et al.*, exhibited a reversible capacity of 195 mAh g^{-1} at 0.25 C after 400 cycles.[63]

Recently, two Mo-based MXenes have also been prepared and examined as anode material for LIBs. Anasori *et al.* identified the resemblance of electrochemical behaviour of $Mo_2TiC_2T_x$ to be quite different to that of $Ti_3C_2T_x$ and with reversible capacity of 145 mAh g^{-1} at 1 C after 160 cycles.[17] Synthesized by Halim *et al.*, the first Mo_2CT_x with an addition of 8 wt. % MWCNTs, reported a reversible capacity of 250 mAh g^{-1} at 5 A g^{-1}, 76 mAh g^{-1} at 10 A g^{-1}, both after 1000 cycles.[32] Table S1 in Supplementary Information shows the list of investigated Ti-, Nb-, V-, and Mo-based MXenes as prospective LIB anode material.

It is noted that device manufacturing requirements such as current collectors, conductive agents, polymeric binders etc. inevitably compromise the eventual volumetric capacities, thus there have been much effort towards preparing free-standing, binder-free MXene electrodes. The gravimetric capacity (normalized to the total electrode mass) is also observed to be negatively affected by a higher thickness or mass loading. Most work to date has been evaluated as LIB electrode in half-cell configuration, with few assembled into full cell to determine their energy and power densities which are in fact more critical for practical applications.

3.4.2 Supercapacitors. Supercapacitors provide alternative energy storage with rapid power density but low energy density as compared to batteries. Therefore, researches have targeted primarily on improving their volumetric capacity, i.e. energy density per volume. Per their charge-discharge mechanisms, supercapacitors are classified as either electrical double-layer capacitors (EDLCs) or pseudocapacitors. The former is based on the reversible accumulation of electrolyte ions at the electrode-electrolyte interfaces without redox reactions, while the latter relies on fast and reversible surface redox reactions, however retaining rectangular-shaped CV curves. In general, pseudocapacitors possess higher volumetric capacitances and lowered cycling stability. MXenes, with their 2D characteristics, large surface areas and highly defined morphology, present themselves as promising electrode materials for supercapacitors.

Lukatskaya *et al.* used electrochemical in-situ X-ray absorption spectroscopy (XAS) to probe the mechanism of high

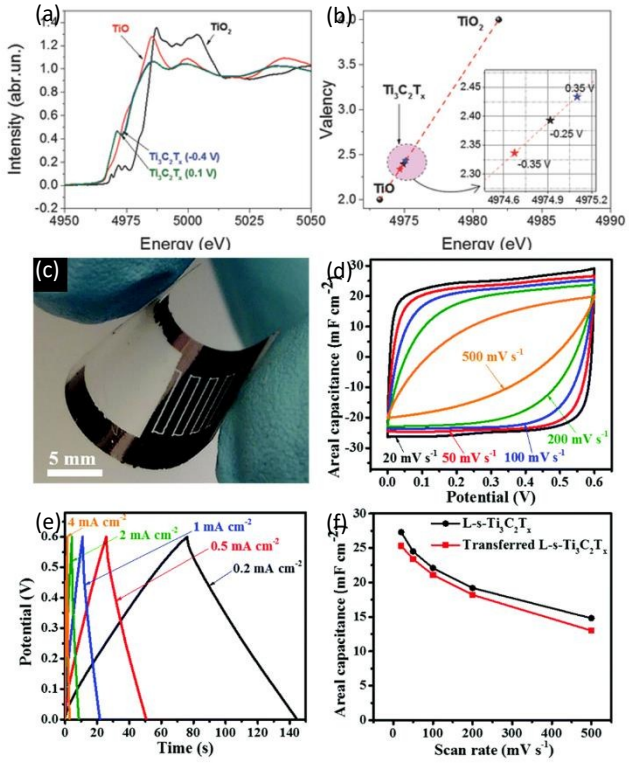

Fig. 21 (a) Ti K-edge XANES spectra of $Ti_3C_2T_x$ at −0.4 V (blue line) and 0.1 V (green line), together with those of TiO (red line) and TiO_2 (black line). (b) Average Ti oxidation state determination in $Ti_3C_2T_x$ at various applied potentials (see inset), using the Ti K-edge energy shift of the reference TiO and TiO_2 compounds [reprinted with permission from ref. 159. Copyright 2015 John Wiley & Sons, Inc.]. (c) Digital photograph showing the transferred L-s-$Ti_3C_2T_x$ MXene MSC on flexible scotch tape, and the corresponding (d) CVs, (e) charge–discharge curves, and (f) variation in areal capacitances with scan rates [reprinted with permission from ref. 169. Copyright 2016 The Royal Society of Chemistry].

View Article Online
DOI: 10.1039/C8TA04778E

capacitance of $Ti_3C_2T_x$ in 1 M H_2SO_4 aqueous electrolyte (Fig. 21a). Changes in Ti oxidation state of $Ti_3C_2T_x$ are detected during charge/discharge, indicative that the predominant electrochemical behaviour of $Ti_3C_2T_x$ is pseudocapacitive (which produces rectangular-shaped CVs. More importantly, the average Ti oxidation state in $Ti_3C_2T_x$, by first approximation, is closer to +2 than +4 (Fig. 21b).[159]

Xu *et al.* adopted a classic molecular dynamic simulation to examine a representative $Ti_3C_2(OH)_2$ electrode, with a slit nanopore, in room temperature ionic liquid and ascertained that charge storage is a combination of fast counter-ion insertion and counter-ion/co-ion exchange. Electrolyte ions are shown to spontaneously wet the $Ti_3C_2(OH)_2$ slit nanopore even in the absence of external potential. Additionally, cyclic variation of spatial distribution of ions and orientation of cation dipoles within the pore during charging/discharging help screened external electric potential. Ions are theoretically observed to be significantly accelerated and have more ordered dipole orientation within $Ti_3C_2(OH)_2$ electrode with a narrower slit (analogous to layer distance).[160]

Ghidiu *et al.* pioneered the work to preparation of a clay-like paste of HCl/LiF etched $Ti_3C_2T_x$ with intercalated water and ions from that could be conveniently used to assemble flexible and freestanding film. When evaluated in a three-electrode configuration in 1 M H_2SO_4 electrolyte at scan rate of 2 mV s^{-1}, these as-prepared films displayed high volumetric capacitance of 900 F cm^{-3} in the absence of faradaic redox reaction.[30] Comparatively, Dall'Agnese *et al.* attempted surface chemistry modifications to replace –F in HF-etched $Ti_3C_2T_x$ with hydroxyl groups and delaminated multi-layered $Ti_3C_2T_x$ that were pre-intercalated with DMSO; and the prepared electrode only registered a moderate volumetric capacitance of 520 F cm^{-3} under similar testing conditions.[80] Hu *et al.* via a facile dropping-mild baking (DMB) method to prepare electrode of $Ti_3C_2T_x$ films on nickel foam with excellent gravimetric capacitance of 499 F g^{-1} (albeit low active material loading and tested in a two-electrode configuration), provided some food for thought to alternative fabrication of MXene-based energy storage devices.[161]

In view of the inclination of delaminated $Ti_3C_2T_x$ stacks restacking and limiting full access of electrolyte ions to their surfaces during electrode preparation, Zhao *et al.* introduced a simple procedure of repeated, alternating filtration of $Ti_3C_2T_x$ suspension and SWCNTs dispersion and obtained a volumetric capacitance of 390 F cm^{-3} at 2 mV s^{-1}. Although $MgSO_4$, a less toxic and affordable neutral electrolyte, offers a broader operating voltage window, its poorer conductivity limits the measured capacitance.[55]

In line with the idea to incorporate interlayer spacers, Boota *et al.* managed in situ polymerization of PPy and alignment of PPy chains between $Ti_3C_2T_x$ layers and attained a more conductive, pseudocapacitive composite with exceptional volumetric capacitance close to 1000 F cm^{-3} at 5 mV s^{-1}.[56] Zhu *et al.* electrophoretically deposited HF-etched $Ti_3C_2T_x$ onto fluoride-doped tin oxide (FTO) substrate for 30 s, and subsequently immersed in an electrochemical polymerizing electrolyte and polymerized for 600 s to fabricate an electrochemically optimized free-standing PPy/ $Ti_3C_2T_x$ film with volumetric and gravimetric capacitances of 291 F cm^{-3} and 485 F g^{-1}, respectively at 1 mA cm^{-2} and excellent cyclic stability with ca. 100 % capacitance retention after 20 000 cycles.[162]

Lin *et al.* prevented the restacking of delaminated $Ti_3C_2T_x$ stacks by means of a $Ti_3C_2T_x$ hydrogel film and recorded a gravimetric capacitance of 62 F g^{-1}.[163] Dall'Agnese *et al.* extended the capacitance testing of $Ti_3C_2T_x$/MWCNTs in organic electrolyte, and attained a moderate capacitance of 245 F cm^{-3} at 2 mV s^{-1}.[164] Yan *et al.* alternatively measured the capacitance of $Ti_3C_2T_x$/MWCNTs in an alkaline electrolyte of 6 M KOH and recorded a capacitance of 393 F cm^{-3} at 5 mV s^{-1}.[165] Through partial oxidation of $Ti_3C_2T_x$, Zhu *et al.* synthesized a TiO_2/ $Ti_3C_2T_x$ composite with a gravimetric capacitance of 143 F g^{-1} at 5 mV s^{-1}.[71] Rakhi *et al.* and Tang *et al.* have coincidentally explored different forms of MnO_2 as interlayer spacers for $Ti_3C_2T_x$ and attained improved electrochemical performances.[166, 167] Wang *et al.* synthesized a 38 wt. % delaminated HF-etched $Ti_3C_2T_x$/nickel-aluminium layered double hydroxide composite by a liquid phase deposition with outstanding specific capacitance of 1061 F g^{-1} at current density of 1 A g^{-1}.[168]

Progressively, towards the development of flexible energy storage devices, Peng *et al.* fabricated an all-$Ti_3C_2T_x$ solid-state interdigital prototype microsupercapacitor (MSC) by solution spray-coating of large size (3–6 μm laterally) HCl/LiF eteched $Ti_3C_2T_x$ as the current collector, followed by spray-coating small size HCl/LiF etched $Ti_3C_2T_x$ (ca. 1 μm) with more defects and edges on top as the electroactive layer (Fig. 21c-f). The interdigital pattern was carved by a photoresist-free direct laser cutting method and then meticulously filled with a PVA/H_2SO_4 gel electrolyte. The all-$Ti_3C_2T_x$ device, with comparatively lower contact resistance than those with platinum current collectors, recorded areal and volumetric capacitances of ca. 27 mF cm^{-2} and ca. 357 F cm^{-3}, respectively, at a scan rate of 20 mV s^{-1} and demonstrated exceptional cyclic stability with a 100 % capacitance retention after 10 000 cycles at scan rate of 50 mV s^{-1}.[169]

Kurra *et al.* adopted a scalable and cost-efficient Meyer rod coating of HF-etched $Ti_3C_2T_x$ and HCl/LiF etched $Ti_3C_2T_x$ slurries on commercially available A4 printing paper. These flexible fabricated devices, when supported on a flat plastic or glass substrate, were capably carved by laser patterning. The HCl/LiF etched $Ti_3C_2T_x$ microsupercapacitor (ca. 125 μm), with larger interlayer spacing and better conductivity, showed an areal capacitance of 25 mF cm^{-2} and 10.5 mF cm^{-2}, respectively, at scanning rates of 20 mV s^{-1} and 1000 mV s^{-1}. Its HF-etched counterpart (ca. 125 μm) only recorded areal capacitance of 6.2 mF cm^{-2} and 4.2 mF cm^{-2}.[170]

Li *et al.* assembled a conventional sandwich-type all-solid-state supercapacitor with a PVA/H_3PO_4 soaked glass fiber membrane inserted between two pieces of 75 wt. % HF-etched $Ti_3C_2T_x$/electrochemically exfoliated graphene nanocomposite film electrode. This device delivered a volumetric capacitance of 184 F cm^{-3} at current density of 0.2 A cm^{-3} and retained 85.2 % of initial volumetric capacitance after 2500 cycles. A flexible interdigital microsupercapacitor was fabricated by spray-coating the same composition of HF-etched

View Article Online
DOI: 10.1039/C6TA06772G

$Ti_3C_2T_x$/electrochemically exfoliated graphene solution onto a polyethylene terephthalate (PET) substrate through a mask. This fabricated device measured an areal capacitance of 3.26 mF cm^{-2} and volumetric capacitance of 33 F cm^{-3} at 5 mV s^{-1}.[171]

Although Ti_2CT_x has a higher calculated gravimetric capacitance than $Ti_3C_2T_x$, $Ti_3C_2T_x$ is still the most studied pseudocapacitive MXene for its superior electronic conductivity and chemical stability.[14] There are growing interest in Nb- and Mo-based MXenes as well for they potentially possess an even larger capacitance.[17, 32, 64] Table S2 in Supplementary Information summarizes the use of various MXenes in as electrode material for supercapacitor.

It is noteworthy that capacitance values are dependent on various parameters, such as constitutes of composites, electrolytes, scan rate, current load, mass ratio and cell configuration, therefore mere numerical comparison of capacitance should be taken with a pinch of salt.

3.4.3 Beyond LIBs and supercapacitors. As various cations (Li^+, Na^+, Mg^{2+}, K^+, NH_4^+ and Al^{3+}) have been observed to spontaneously intercalate in between $Ti_3C_2T_x$ layers, $Ti_3C_2T_x$ has been earmarked as potential Na-, K-, Mg-and Al-ion batteries/capacitors.[26, 87, 99, 104] Beyond Li, other elements offer more abundancy and possibly greater gravimetric capacity due to multi-electron redox chemistry. Yang *et al.* predicted the theoretical Na^+ storage capacity of various M_2CT_x via DFT computations and derived at capacities from 190-288 mAh g^{-1}. Wang *et al.* assessed HF-etched multi-layered Ti_2CT_x as a negative electrode for Na-ion hybrid capacitor and recorded a reversible capacity of 175 mAh g^{-1} at 20 mA g^{-1} at the end of 100 cycles in a half-cell configuration and configured it into a prototype Na-ion full cell as well.[172]

Xie *et al.* first reported $Ti_3C_2T_x$ to have an experimental reversible capacity of 80 mAh g^{-1} at 100 mA g^{-1} after 120 cycles in a Na-ion half-cell configuration as well as calculated its theoretical capacity to be 268 mAh g^{-1}, assuming single Na adsorption layer.[99] Evidently, with a different interlayer distance input, Er *et al.* derived at a different theoretical capacity of 351.8 mAh g^{-1} for Na^+ on $Ti_3C_2T_x$; and Yu presented a theoretical value exceeding 367.7 mAh g^{-1}.[87, 173] Wang *et al.* recorded HF-etched $Ti_3C_2T_x$ with a reversible Na^+ ion storage capacity of 68.3 mAh g^{-1} at 200 mA g^{-1} even after 1000 cycles, demonstrating its long-term cycling stability and experimentally observed the formation of double Na-atomic layers amongst the $Ti_3C_2T_x$ interlayers, thus reaffirming the possibility of multi-layer adsorption (Fig. 22a-f).[174] Kajiyama *et al.* related a small portion of Na^+ being trapped within the structure of $Ti_3C_2T_x$ even after full desodiation to an increase of interlayer distance from 9.7 Å to 12.5 Å; together with the penetrated solvent molecules, they beneficially swelled the interlayer spaces of $Ti_3C_2T_x$ during initial cycles of sodiation.[175] Xie *et al.* experimented with a self-assembled porous multi-layered $Ti_3C_2T_x$/MWCNTs composite that measured a high volumetric capacity of 421 mAh cm^{-3} at 20 mA g^{-1}.[57] Another MXene, V_2CT_x, was paired with hard carbon and assembled into full cell, achieving a capacity of 50 mAh g^{-1}.[176]

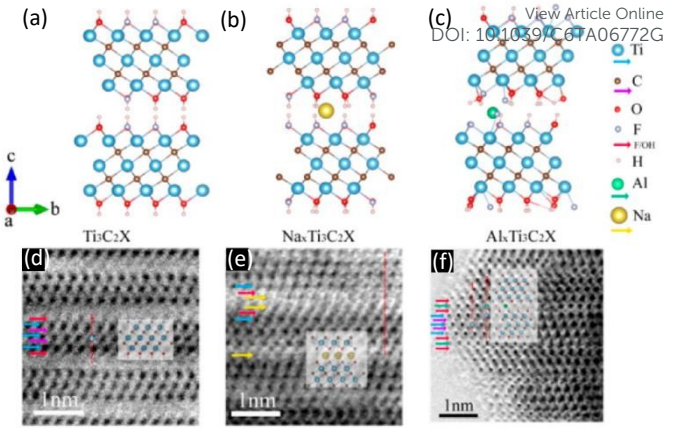

Fig. 22 Optimized geometries of Ti_3C_2X (a), $Na_xTi_3C_2X$ (b), $Al_xTi_3C_2X$ (c) from side view. The DFT calculations were performed with a modified model based on experimental results and indicated that the Na ions can easily diffuse in Ti_3C_2X. (d) Annular bright-field (ABF) image of Ti_3C_2X observed along the *a*/*b* axis. Two C atomic layers (labelled with purple arrows) interleave into three Ti-atomic layers (labelled with blue arrows) with a sequence of Ti(s)–C–Ti(c)–C–Ti(s), forming an edge-shared TiC_6 octahedral stacking. The functional groups such as O and/or F atoms (labelled with red arrows) prefer to stay on top of the Ti(c) atoms, instead of the topmost sites of the C atoms on both sides of the Ti_3C_2 layer. (e) ABF image of Ti_3C_2X electrodes upon Na intercalation with cutoff potential of 0.0 V. Inset shows that Na ions are intercalated into Ti_3C_2X from the surface, fully occupying the interlayers and remained on top of the C atoms rather than on top of the Ti(s) or Ti(c) atoms in the Ti_3C_2X layer. Moreover, double Na-atomic layers (labelled with double yellow arrows) are observed in one interlayer of the fully intercalated sample. (f) ABF image of Ti_3C_2X upon Al intercalation. Intercalation of the Al ions (labelled with green arrows) induces horizontal sliding of the Ti_3C_2X monolayer [reprinted with permission from ref. 174. Copyright 2015 American Chemical Society].

Zhao *et al.* loaded HF-etched multi-layered $Ti_3C_2T_x$ via an impregnation process at 155 °C for 24 h, and evaluated its performance as a lithium-sulfur (Li-S) battery cathode. This pioneering Li-S cathode retained a high reversible capacity of 970 mAh g^{-1} at 200 mA g^{-1} even after 100 cycles.[177] Interestingly, Liang *et al.* loaded 70 wt. % of sulfur into delaminated HF-etched Ti_2CT_x and measured a reversible capacity of 723 mAh g^{-1} at C/2 after 650 cycles. The strong interaction between polysulfides and surface Ti atoms was attributed to mitigation of the loss of active material, and consequential good cycling performance.[178] Recently, Lin *et al.* incorporated delaminated HCl/LiF-prepared $Ti_3C_2T_x$ into a glass fiber membrane for Li-S batteries via simple vacuum filtration. Highly active surfaces of $Ti_3C_2T_x$ chemically bonded with lithium polysulfides (LiPSs) via strong metal-sulfur interactions, thereby suppressing the dissolution of LiPSs. The performance of commercial bulk S cathode was greatly improved to a high reversible capacity of 591 mAh g^{-1} at 1.5 A g^{-1} after 100 cycles.[179] Bao *et al.* synthesized a hierarchical structure of 20 wt. % HF-etched $Ti_3C_2T_x$/Mesoporous C by a single-step pyrolysis of $Ti_3C_2T_x$/MOF-5 at 900 °C for 3 h in argon and subsequent HF etching to remove ZnO. $Ti_3C_2T_x$/MOF-5 was obtained from solvothermal synthesis of a 40 mL DMF mixture, containing 10 mg of $Ti_3C_2T_x$, 0.6 mmol of zinc nitrate hexahydrate, 0.2 mmol of terephthalic

acid and 0.085 mL triethylamine, at 105 °C for 24 h. The $Ti_3C_2T_x$/Mesoporous C/S composite cathode, from heating $Ti_3C_2T_x$/Mesoporous C and elemental sulfur at 155 °C for 10 h in Ar, attained a high reversible capacity of 704.6 mAh g^{-1} at current density of 837.5 mA g^{-1} (C/2) after 300 cycles. Its good electrochemical performance was attributed to effective trapping of LiPSs by active hydrophilic surfaces of $Ti_3C_2T_x$ surfaces as well as delay of outward diffusion of LiPSs due to strong physical adsorption by the mesoporous matrix of the nanocomposite.[180]

3.5 Electrocatalysts

Electrolytic/solar water splitting, involving oxygen evolution reaction (OER) ($2H_2O \rightarrow 4\,e^- + 4H^+ + O_2$) and hydrogen evolution reaction (HER) ($2H^+ + 2e^- \rightarrow H_2$), is one important clean energy technology. However, like oxygen reduction reaction (ORR) at the cathode of fuel cells which requires the use of expensive noble metal catalyst, its commercial uptake is limited, hence there are extensive efforts towards the development of highly efficient and cost-effective non-precious metal electrocatalysts.

Ma *et al.* assembled a robust free-standing hybrid film of delaminated HF-etched $Ti_3C_2T_x$ and exfoliated graphitic carbon nitride (g-C_3N_4) nanosheets by vacuum filtration. As a working electrode for OER, this $Ti_3C_2T_x$- g-C_3N_4 hybrid exhibited a sharp onset potential at 1.44 V (vs. reversible hydrogen electrode (RHE)) and a low operating potential of 1.65 V to deliver a 10.0 mA cm^{-2} in 0.1 M KOH (Fig. 23a-c). Its excellent performance was attributed to Ti-N_x motifs acting as electroactive sites, its high surface area from hierarchically porous structure contributing to a high electrochemical double layer capacitance and its hydrophilicity and high porosity enabling good wettability of active surfaces to allow rapid transport of reactants and removal of reaction products. This freestanding hybrid film was also examined as a trial air cathode in rechargeable zinc (Zn)-air battery and at current density of 20 mA cm^{-2}, it registered discharging (ORR) at 0.87 V and charging at 2.55 V.[76]

Wang *et al.* hydrothermally synthesized rutile $TiO_2/Ti_3C_2T_x$ composites at 95 °C for 4 h and identified an optimal $Ti_3C_2T_x$ content of 5 wt. % which recorded a 400 % enhancement in photocatalytic HER at ca. 17.8 μmol h^{-1} $g_{catalyst}^{-1}$ as compared to pure rutile TiO_2. By strategically encapsulating $Ti_3C_2T_x$ with rutile TiO_2, the intimate contact allowed sufficient light absorption by TiO_2, efficient charge transfer from TiO_2 to $Ti_3C_2T_x$, formed a depletion layer at the $Ti_3C_2T_x$-TiO_2 interface (Schottky barrier) (Fig. 23d) which facilitated electron-hole separation and improved photocatalytic activity. Adopting an identical synthesis approach, TiO_2/Ti_2CT_x and TiO_2/Nb_2CT_x composites with 5 wt. % loading of MXenes were prepared. TiO_2/Nb_2CT_x composite demonstrated the best performance as co-catalysts for photocatalytic HER with the weakest photoluminescence emission peak because Nb_2CT_x has the highest work function amongst the MXenes used in this work whereas $TiO_2/Ti_3C_2T_x$ displayed the lowest hydrogen evolution rate.[72]

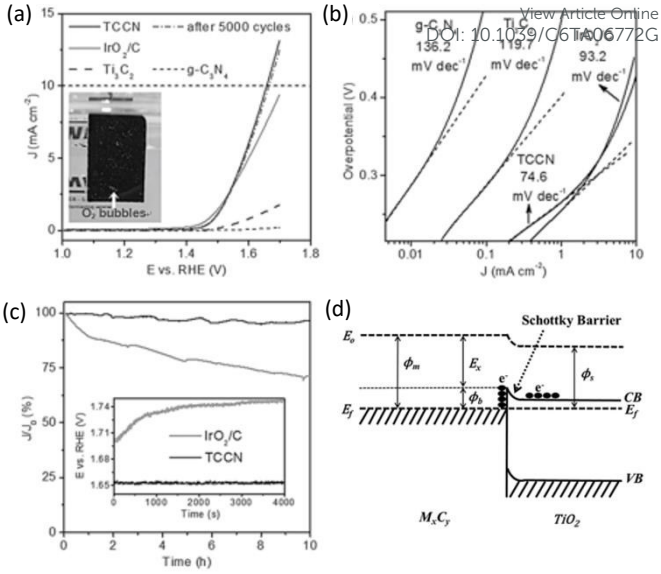

Fig. 23 (a) Polarization curves, (b) Tafel plots of TCCN, IrO_2/C, Ti_3C_2, and g-C_3N_4 in an O_2-saturated 0.1 m KOH solution (scan rate: 0.5 mV s^{-1}). Inset in panel a) optical image of TCCN directly used as the OER electrode operating at 1.70 V with generated bubbles on the surface indicating the formation of O_2 gas. Dash line in (a) Polarization curve of TCCN after 5000 potential cycles (scan rate: 100 mV s^{-1}). (c) Chronoamperometric response at a constant potential of 1.65 V ($E_{j=10}$ of TCCN). Inset shows chronopotentiometric response at a constant current density of 10.0 mA cm^{-2} of TCCN as compared to that of IrO_2/C [reprinted with permission from ref. 76. Copyright 2015 John Wiley & Sons, Inc.]. (d) Schematic for formation of Schottky Barrier at the MXene/TiO_2 interface [reprinted with permission from ref. 72. Copyright 2016 John Wiley & Sons, Inc.].

Seh *et al.* presented a combined theoretical and experimental study of Ti_2CT_x and Mo_2CT_x as independent electrocatalysts for HER. First, the hydrogen adsorption free energy (ΔG_H) of various M_2XT_x was derived by DFT calculations and presented as a volcano plot. Mo_2C and Ti_2C, both with =O on the basal plane as catalytically active sites, were calculated to have a theoretical overpotential of 48 mV and 358 mV respectively. Experimentally, HF-etched Mo_2CT_x, as evaluated in a three-electrode electrochemical cell using a rotating disk electrode apparatus at 1600 rpm in 0.5 M H_2SO_4, maintained a stable HER activity after ca. 30 cycles, reaching current density of 10 mA cm^{-2}_{geo} at an overpotential of 305 mV whereas HF-etched Ti_2CT_x recorded an initial overpotential of 609 mV to reach 10 mA cm^{-2}_{geo} and its HER activity deteriorated further upon continued cycling. Expectedly, delaminated HF-etched Mo_2CT_x, with increased proportion of exposed basal planes, recorded improved HER activity and supported the theory of basal planes as the most probable surfaces for Mo_2CT_x's catalytic activity.[181]

Ling *et al.*, using projector augmented wave method, identified poor HER catalytic activity of pure V_2CO_2 was due to high H binding strength and elucidated that through strain engineering and introduction of high catalytic transition metal (Fe, Co, and Ni) onto the surface of V_2CO_2, the H–O binding strength can indeed be weakened and thus improve the HER performance.[182]

View Article Online DOI: 10.1039/C8TA06772G

By screening 48 MXenes using ab initio calculations, Guo *et al.* shortlisted two yet-to-be-synthesized but stable MXenes, Zr_2CO_2 and Hf_2CO_2, with good optical absorption in the wavelength from 300 to 500 nm and high and directionally anisotropic carrier mobility as candidate single photocatalyst for efficient water splitting to produce hydrogen.[183]

Zhang *et al.* synthesized an urchin-shaped alkalization-intercalated HF-etched $Ti_3C_2/Ag/Ag_{0.9}Ti_{0.1}$ bimetallic nanowire composite by mixing AgNO3, NaOH-treated $Ti_3C_2T_x$ and PVP at room temperature. This nanocomposite, recorded exceptional electrocatalytic activity for ORR, with onset potential of 0.921 V and half-wave potential of 0.782 V. The layered conductive $Ti_3C_2T_x$ provided effective electron pathway for the transfer of electron from Ti or C to Ag and numerous favourable oxygen adsorption sites. The Ti-doping of Ag nanowires, increased the concentration of defects or vacancies, which provided even more oxygen adsorption sites. These Ti-doped Ag nanowires could also act as a bifunctional catalyst to catalyse different ORR steps.[77]

Xie *et al.* explored the use of HF-etched $Ti_3C_2T_x$ as more active and durable support for platinum (Pt) nanoparticles cathode catalyst for proton exchange membrane fuel cells. The 20 wt. % Pt/ $Ti_3C_2T_x$ was prepared by refluxing a homogeneous mixture, containing ethylene glycol, 320 mg of $Ti_3C_2T_x$, 240 mg of trisodium citrate dehydrate and 160 mg of chloroplatinic acid, at 160 °C for 2 h in N_2. The numerous –OH and –F groups on HF-etched $Ti_3C_2T_x$ served as anchor points that facilitated well dispersion and strong binding of Pt nanoparticles. It was also suggested that the strong Pt-$Ti_3C_2T_x$ interaction could have altered the electronic structure of Pt nanoparticles prevented the oxidation and subsequent dissolution of Pt catalyst.[184]

4. Conclusions and Outlook

In summary, we have provided an overview of the progress in synthesis, characterization and applications of the new family of 2D early transition metal carbides, carbonitrides and nitrides, by using different fluoride compounds as etchants under various conditions. Two of the most mature synthesis routes to layered carbides and carbonitrides are HF etching and HCl/LiF etching,
each brings about multi-layered MXenes with different morphologies and surface chemistries. Although only weak residual forces hold and prevent HF-etched multi-layered MXenes from readily separating into individual layers, a mere sonication procedure without preceding intercalation of species between the layers can only result in low yield of single/few-layered MXenes.

Most recently, with a modified HCl/LiF etching procedure with an increased molar ratio of LiF to Ti_3AlC_2 of 7.5:1 instead of 5:1, while other aspects of the procedure (in 6 M HCl solution at 35°C for 24 h) remained identical to that reported by Ghidiu *et al.*, delaminated $Ti_3C_2T_x$ flakes have been reportedly obtained without sonication and their yield can be further improved with a more concentrated HCl etchant solution. These delaminated $Ti_3C_2T_x$ flakes are observed to be 4–15 µm laterally, have well-defined and clean edges and exhibit no visible pin holes. Because a myriad of cations is observed to spontaneously intercalate MXenes, the implications are far reaching and influential as seen with delaminating stacked MXenes, preparation of MXene composites and their various potential applications.

Importantly, clay-like (hydrated), HF-etched multi-layered $Ti_3C_2T_x$ can only be prepared when intercalant source, LiCl, is present as part of the etchant solution—rather than as a later addition. Evidently, new reducing agents, etchants, and intercalants, for fluoride-free MXene synthesis protocol, to control desired chemical species to bind on the surface of MXene's and fine-tune the properties and expand their potential applications, are to be explored.

Experimentally, in most polymeric-based composites, beyond the ubiquitous single/few layers of DMSO-intercalated HF-etched $Ti_3C_2T_x$ fillers, incorporation and studies of other experimentally viable, exfoliated single/few-layered MXenes as fillers in polymer composites remain bewildering unexplored. Detailed investigations of mechanism of matrix-filler interfacial interaction(s), quantification and characterization of enhanced mechanical properties of polymeric composites with inclusions of different MXene-based fillers, variation in processing pathways to manipulate stacking of fillers within polymeric matrices can provide invaluable insights and contribute to the development of future applications.

As the most well-studied MXene, $Ti_3C_2T_x$ and its composites have been explored as candidates for the sequestration of heavy metal pollutants and absorption of dyes and radionuclide. Also, they could be used as biocide in water treatment, which has demonstrated promising results. Experimentally, much work remains to be conducted to fully understand the difference in absorption of various ions, when deploying in a more complex but realistic environmental setup. To evaluate the reliability and lifespan of the proposed systems, more comprehensive studies are required to clarify the actual mechanism and reversibility of absorption and release ions/molecules/pollutants/radionuclide by $Ti_3C_2T_x$ and investigate the degradation in performance after repeated usage. One such example reported up to date is the first use of HF-etched multi-layered $Ti_3C_2T_x$ as a novel intercalation electrode for desalination via capacitive deionization (CDI).

By varying the synthesis conditions, fundamentally different $Ti_3C_2T_x$, in terms of the degree of exfoliation and delamination (i.e., number of atomic layers) and the proportion of surface terminations, and consequently electromagnetic wave absorption or shielding performance, have been discussed. More interestingly, surface modification to the MXene, use of other members in the MXenes family or MXene-based composites with the inclusion of magnetic nanostructures all deserve to be further explored.

The use of MXene-based composites, with different filler(s), such as metal oxides with higher specific capacity, for energy storage applications, are inevitable, due to the inherent moderate theoretical capacity of MXenes. Incorporation of interlayer spacers, such as CNTs or PPy, to provide additional electron conductive pathways and maintain interlayer spaces that promote electrolyte ion access and transportation, has

been successful in enhancing overall electrochemical performances of the materials. It remains intriguingly challenging to alternatively attain a hierarchical structure with intimate contact and well-distribution of exposed non-Ti additive component(s) amongst the carbide MXene matrix. As the first nitride MXene, $Ti_4N_3T_x$ has been recently prepared, so that we anticipate the incorporation of the more conductive nitride MXene, with higher theoretical specific capacity as the default composite matrix instead of carbide MXene for high energy and power density applications and especially so if the more lightweight Ti_2N (487 mAh g^{-1}), can be experimentally synthesized. More in-situ characterizations are necessary for mechanistic studies of the exact lithium/sodium ion storage and reaction pathways.

From experimental characterizations, existing idealized and hypothetical models have been identified to be inadequate and limited in accurate property predictions of multi-layered or intercalated MXene stacks. Therefore, ensuing models should accommodate interlayer interactions, such as van der Waals forces and hydrogen bonding, for more realistic computations of these inherently complex MXenes. Our current incomplete understanding of the surface chemistry of the MXenes, i.e., the exact species bond to the MXene surfaces during synthesis and their precise contribution to the overall stoichiometry, adds to the difficulty of the already challenging theoretical studies. Indispensably, modelling remains vital to discovering novel and unexpected properties (such as directionally anisotropic carrier mobility), screening yet-to-be-synthesized MXenes with attractive properties (such as room-temperature ferromagnetism and semi conductance), thus guiding experimental efforts.

Several few-layered MXenes have been found to be potential candidates as transparent conductors, while various multi-layered MXenes have carved their niches in environmental remediation. MXene-based composites have opened a new pathway to the advancement in various energy storage systems, due to the possible synergistic effect in agglomeration prevention, facilitating electronic conductivity, improving electrochemical stability, enhancing pseudocapacitance and minimizing the shortcomings of individual components. Regardless of the advancement of these 2D layered MXenes and their composites in transparent conductors, environmental remediation, electromagnetic wave absorption and shielding, electrocatalysts, Li-ion batteries (LIBs), supercapacitors and other electrochemical storage systems, more works, such as understanding the exact mechanisms behind certain properties and precise engineering the surface chemistries to attain desired performances, remain to be conducted in the near future.

Acknowledgements

K. Zhou would like to acknowledge the funding support of AcRF Tier 1 project (RG128/14), MOE, Singapore. P. S. Lee acknowledged the funding award no. NRF-NRFI2016-05. We would like to thank Prof. Y. Gogotsi for his valuable suggestions to our manuscript.

Reference

View Article Online
DOI: 10.1039/C6TA06772G

1. M. Naguib, M. Kurtoglu, V. Presser, J. Lu, J. Niu, M. Heon, L. Hultman, Y. Gogotsi and M. W. Barsoum, *Advanced Materials*, 2011, **23**, 4248-4253.
2. M. W. Barsoum, *MAX phases: properties of machinable ternary carbides and nitrides*, John Wiley & Sons, 2013.
3. B. Anasori, J. Halim, J. Lu, C. A. Voigt, L. Hultman and M. W. Barsoum, *Scripta Materialia*, 2015, **101**, 5-7.
4. H. B. Zhang, Y. C. Zhou, Y. W. Bao, M. S. Li and J. Y. Wang, *Journal of the European Ceramic Society*, 2006, **26**, 2373-2380.
5. M. W. Barsoum, T. El-Raghy and M. Ali, *Metallurgical and Materials Transactions A*, 2000, **31**, 1857-1865.
6. M. W. Barsoum, *Progress in Solid State Chemistry*, 2000, **28**, 201-281.
7. Z. Sun, D. Music, R. Ahuja, S. Li and J. M. Schneider, *Physical Review B*, 2004, **70**, 092102.
8. J. Emmerlich, D. Music, P. Eklund, O. Wilhelmsson, U. Jansson, J. M. Schneider, H. Högberg and L. Hultman, *Acta Materialia*, 2007, **55**, 1479-1488.
9. Z. M. Sun, *International Materials Reviews*, 2011, **56**, 143-166.
10. M. Naguib, V. N. Mochalin, M. W. Barsoum and Y. Gogotsi, *Advanced Materials*, 2014, **26**, 992-1005.
11. J.-C. Lei, X. Zhang and Z. Zhou, *Frontiers of Physics*, 2015, **10**, 276-286.
12. Y. Xiao, J.-Y. Hwang and Y.-K. Sun, *Journal of Materials Chemistry A*, 2016, **4**, 10379-10393.
13. P. Kumar, H. Abuhimd, W. Wahyudi, M. Li, J. Ming and L.-J. Li, *ECS Journal of Solid State Science and Technology*, 2016, **5**, Q3021-Q3025.
14. M. Naguib, O. Mashtalir, J. Carle, V. Presser, J. Lu, L. Hultman, Y. Gogotsi and M. W. Barsoum, *ACS Nano*, 2012, **6**, 1322-1331.
15. M. Naguib, J. Halim, J. Lu, K. M. Cook, L. Hultman, Y. Gogotsi and M. W. Barsoum, *Journal of the American Chemical Society*, 2013, **135**, 15966-15969.
16. M. Ghidiu, M. Naguib, C. Shi, O. Mashtalir, L. M. Pan, B. Zhang, J. Yang, Y. Gogotsi, S. J. L. Billinge and M. W. Barsoum, *Chemical Communications*, 2014, **50**, 9517-9520.
17. B. Anasori, Y. Xie, M. Beidaghi, J. Lu, B. C. Hosler, L. Hultman, P. R. C. Kent, Y. Gogotsi and M. W. Barsoum, *ACS Nano*, 2015, **9**, 9507-9516.
18. J. Yang, M. Naguib, M. Ghidiu, L.-M. Pan, J. Gu, J. Nanda, J. Halim, Y. Gogotsi and M. W. Barsoum, *Journal of the American Ceramic Society*, 2016, **99**, 660-666.
19. R. Meshkian, L.-Å. Näslund, J. Halim, J. Lu, M. W. Barsoum and J. Rosen, *Scripta Materialia*, 2015, **108**, 147-150.
20. J. Zhou, X. Zha, F. Y. Chen, Q. Ye, P. Eklund, S. Du and Q. Huang, *Angewandte Chemie*, 2016, **128**, 5092-5097.
21. O. Mashtalir, M. Naguib, B. Dyatkin, Y. Gogotsi and M. W. Barsoum, *Materials Chemistry and Physics*, 2013, **139**, 147-152.
22. F. Chang, C. Li, J. Yang, H. Tang and M. Xue, *Materials Letters*, 2013, **109**, 295-298.
23. Z. Sun, S. Li, R. Ahuja and J. M. Schneider, *Solid State Communications*, 2004, **129**, 589-592.
24. B. Chen, F. Chang, J. Yang, H. Tang and C. Li, *Crystal Research and Technology*, 2014, **49**, 813-819.

25. J. Halim, M. R. Lukatskaya, K. M. Cook, J. Lu, C. R. Smith, L.-Å. Näslund, S. J. May, L. Hultman, Y. Gogotsi, P. Eklund and M. W. Barsoum, *Chemistry of Materials*, 2014, **26**, 2374-2381.
26. M. R. Lukatskaya, O. Mashtalir, C. E. Ren, Y. Dall'Agnese, P. Rozier, P. L. Taberna, M. Naguib, P. Simon, M. W. Barsoum and Y. Gogotsi, *Science*, 2013, **341**, 1502-1505.
27. A. Feng, Y. Yu, Y. Wang, F. Jiang, Y. Yu, L. Mi and L. Song, *Materials & Design*, DOI: http://dx.doi.org/10.1016/j.matdes.2016.10.053.
28. L. Wang, H. Zhang, B. Wang, C. Shen, C. Zhang, Q. Hu, A. Zhou and B. Liu, *Electronic Materials Letters*, 2016, **12**, 702-710.
29. X. Xie, Y. Xue, L. Li, S. Chen, Y. Nie, W. Ding and Z. Wei, *Nanoscale*, 2014, **6**, 11035-11040.
30. M. Ghidiu, M. R. Lukatskaya, M.-Q. Zhao, Y. Gogotsi and M. W. Barsoum, *Nature*, 2014, **516**, 78-81.
31. O. Mashtalir, M. Naguib, V. N. Mochalin, Y. Dall'Agnese, M. Heon, M. W. Barsoum and Y. Gogotsi, *Nat Commun*, 2013, **4**, 1716.
32. J. Halim, S. Kota, M. R. Lukatskaya, M. Naguib, M.-Q. Zhao, E. J. Moon, J. Pitock, J. Nanda, S. J. May, Y. Gogotsi and M. W. Barsoum, *Advanced Functional Materials*, 2016, **26**, 3118-3127.
33. Q. Ye, P. Xiao, W. Liu, K. Chen, T. Chen, J. Xue, S. Du and Q. Huang, *RSC Advances*, 2015, **5**, 70339-70344.
34. I. R. Shein and A. L. Ivanovskii, *Computational Materials Science*, 2012, **65**, 104-114.
35. P. Urbankowski, B. Anasori, T. Makaryan, D. Er, S. Kota, P. L. Walsh, M. Zhao, V. B. Shenoy, M. W. Barsoum and Y. Gogotsi, *Nanoscale*, 2016, **8**, 11385-11391.
36. J. A. Lane, U. S. A. E. Commission and E. United Nations International Conference on the Peaceful Uses of Atomic, Reading, Mass.
37. M. A. Hope, A. C. Forse, K. J. Griffith, M. R. Lukatskaya, M. Ghidiu, Y. Gogotsi and C. P. Grey, *Physical Chemistry Chemical Physics*, 2016, **18**, 5099-5102.
38. J. Halim, K. M. Cook, M. Naguib, P. Eklund, Y. Gogotsi, J. Rosen and M. W. Barsoum, *Applied Surface Science*, 2016, **362**, 406-417.
39. K. J. Harris, M. Bugnet, M. Naguib, M. W. Barsoum and G. R. Goward, *The Journal of Physical Chemistry C*, 2015, **119**, 13713-13720.
40. T. Zhang, L. Pan, H. Tang, F. Du, Y. Guo, T. Qiu and J. Yang, *Journal of Alloys and Compounds*, DOI: http://dx.doi.org/10.1016/j.jallcom.2016.10.127.
41. F. Shahzad, M. Alhabeb, C. B. Hatter, B. Anasori, S. Man Hong, C. M. Koo and Y. Gogotsi, *Science*, 2016, **353**, 1137-1140.
42. A. Lipatov, M. Alhabeb, M. R. Lukatskaya, A. Boson, Y. Gogotsi and A. Sinitskii, *Advanced Electronic Materials*, DOI: 10.1002/aelm.201600255, 1600255-n/a.
43. M. Ghidiu, J. Halim, S. Kota, D. Bish, Y. Gogotsi and M. W. Barsoum, *Chemistry of Materials*, 2016, **28**, 3507-3514.
44. O. Mashtalir, M. R. Lukatskaya, A. I. Kolesnikov, E. Raymundo-Pinero, M. Naguib, M. W. Barsoum and Y. Gogotsi, *Nanoscale*, 2016, **8**, 9128-9133.
45. M. Naguib, R. R. Unocic, B. L. Armstrong and J. Nanda, *Dalton Transactions*, 2015, **44**, 9353-9358.
46. O. Mashtalir, K. M. Cook, V. N. Mochalin, M. Crowe, M. W. Barsoum and Y. Gogotsi, *Journal of Materials Chemistry A*, 2014, **2**, 14334-14338.
47. O. Mashtalir, M. R. Lukatskaya, M.-Q. Zhao, M. W. Barsoum and Y. Gogotsi, *Advanced Materials*, 2015, **27**, 3501-3506.
48. H. Wang, J. Zhang, Y. Wu, H. Huang, G. Li, X. Zhang and Z. Wang, *Applied Surface Science*, 2016, **384**, 287-293.
49. S. Mahouche-Chergui, S. Gam-Derouich, C. Mangeney and M. M. Chehimi, *Chemical Society Reviews*, 2011, **40**, 4143-4166.
50. X. Zhang, J. Xu, H. Wang, J. Zhang, H. Yan, B. Pan, J. Zhou and Y. Xie, *Angewandte Chemie International Edition*, 2013, **52**, 4361-4365.
51. Z. Ling, C. E. Ren, M.-Q. Zhao, J. Yang, J. M. Giammarco, J. Qiu, M. W. Barsoum and Y. Gogotsi, *Proceedings of the National Academy of Sciences*, 2014, **111**, 16676-16681.
52. M. Naguib, T. Saito, S. Lai, M. S. Rager, T. Aytug, M. Parans Paranthaman, M.-Q. Zhao and Y. Gogotsi, *RSC Advances*, 2016, **6**, 72069-72073.
53. X. Wu, L. Hao, J. Zhang, X. Zhang, J. Wang and J. Liu, *Journal of Membrane Science*, 2016, **515**, 175-188.
54. B. Aïssa, A. Ali, K. A. Mahmoud, T. Haddad and M. Nedil, *Applied Physics Letters*, 2016, **109**, 043109.
55. M.-Q. Zhao, C. E. Ren, Z. Ling, M. R. Lukatskaya, C. Zhang, K. L. Van Aken, M. W. Barsoum and Y. Gogotsi, *Advanced Materials*, 2015, **27**, 339-345.
56. M. Boota, B. Anasori, C. Voigt, M.-Q. Zhao, M. W. Barsoum and Y. Gogotsi, *Advanced Materials*, 2016, **28**, 1517-1522.
57. X. Xie, M.-Q. Zhao, B. Anasori, K. Maleski, C. E. Ren, J. Li, B. W. Byles, E. Pomerantseva, G. Wang and Y. Gogotsi, *Nano Energy*, 2016, **26**, 513-523.
58. Z. Lin, D. Sun, Q. Huang, J. Yang, M. W. Barsoum and X. Yan, *Journal of Materials Chemistry A*, 2015, **3**, 14096-14100.
59. J. Luo, X. Tao, J. Zhang, Y. Xia, H. Huang, L. Zhang, Y. Gan, C. Liang and W. Zhang, *ACS Nano*, 2016, **10**, 2491-2499.
60. M. Naguib, O. Mashtalir, M. R. Lukatskaya, B. Dyatkin, C. Zhang, V. Presser, Y. Gogotsi and M. W. Barsoum, *Chemical Communications*, 2014, **50**, 7420-7423.
61. H. Ghassemi, W. Harlow, O. Mashtalir, M. Beidaghi, M. R. Lukatskaya, Y. Gogotsi and M. L. Taheri, *Journal of Materials Chemistry A*, 2014, **2**, 14339-14343.
62. Z. Li, L. Wang, D. Sun, Y. Zhang, B. Liu, Q. Hu and A. Zhou, *Materials Science and Engineering: B*, 2015, **191**, 33-40.
63. C. Zhang, S. J. Kim, M. Ghidiu, M.-Q. Zhao, M. W. Barsoum, V. Nicolosi and Y. Gogotsi, *Advanced Functional Materials*, 2016, **26**, 4143-4151.
64. C. Zhang, M. Beidaghi, M. Naguib, M. R. Lukatskaya, M.-Q. Zhao, B. Dyatkin, K. M. Cook, S. J. Kim, B. Eng, X. Xiao, D. Long, W. Qiao, B. Dunn and Y. Gogotsi, *Chemistry of Materials*, 2016, **28**, 3937-3943.
65. J. Li, Y. Du, C. Huo, S. Wang and C. Cui, *Ceramics International*, 2015, **41**, 2631-2635.
66. R. B. Rakhi, B. Ahmed, M. N. Hedhili, D. H. Anjum and H. N. Alshareef, *Chemistry of Materials*, 2015, **27**, 5314-5323.
67. S. Lai, J. Jeon, S. K. Jang, J. Xu, Y. J. Choi, J.-H. Park, E. Hwang and S. Lee, *Nanoscale*, 2015, **7**, 19390-19396.
68. B. Ahmed, D. H. Anjum, M. N. Hedhili, Y. Gogotsi and H. N. Alshareef, *Nanoscale*, 2016, **8**, 7580-7587.
69. Y. Gao, L. Wang, A. Zhou, Z. Li, J. Chen, H. Bala, Q. Hu and X. Cao, *Materials Letters*, 2015, **150**, 62-64.
70. F. Wang, C. Yang, M. Duan, Y. Tang and J. Zhu, *Biosensors and Bioelectronics*, 2015, **74**, 1022-1028.
71. J. Zhu, Y. Tang, C. Yang, F. Wang and M. Cao, *Journal of The Electrochemical Society*, 2016, **163**, A785-A791.

72. H. Wang, R. Peng, Z. D. Hood, M. Naguib, S. P. Adhikari and Z. Wu, *ChemSusChem*, 2016, **9**, 1490-1497.
73. C. Peng, X. Yang, Y. Li, H. Yu, H. Wang and F. Peng, *ACS Applied Materials & Interfaces*, 2016, **8**, 6051-6060.
74. Q. Zhang, J. Teng, G. Zou, Q. Peng, Q. Du, T. Jiao and J. Xiang, *Nanoscale*, 2016, **8**, 7085-7093.
75. C. E. Ren, M.-Q. Zhao, T. Makaryan, J. Halim, M. Boota, S. Kota, B. Anasori, M. W. Barsoum and Y. Gogotsi, *ChemElectroChem*, 2016, **3**, 689-693.
76. T. Y. Ma, J. L. Cao, M. Jaroniec and S. Z. Qiao, *Angewandte Chemie International Edition*, 2016, **55**, 1138-1142.
77. Z. Zhang, H. Li, G. Zou, C. Fernandez, B. Liu, Q. Zhang, J. Hu and Q. Peng, *ACS Sustainable Chemistry & Engineering*, 2016, DOI: 10.1021/acssuschemeng.6b01698.
78. G. Zou, Z. Zhang, J. Guo, B. Liu, Q. Zhang, C. Fernandez and Q. Peng, *ACS Applied Materials & Interfaces*, 2016, **8**, 22280-22286.
79. J. Chen, K. Chen, D. Tong, Y. Huang, J. Zhang, J. Xue, Q. Huang and T. Chen, *Chemical Communications*, 2015, **51**, 314-317.
80. Y. Dall'Agnese, M. R. Lukatskaya, K. M. Cook, P.-L. Taberna, Y. Gogotsi and P. Simon, *Electrochemistry Communications*, 2014, **48**, 118-122.
81. Q. Peng, J. Guo, Q. Zhang, J. Xiang, B. Liu, A. Zhou, R. Liu and Y. Tian, *Journal of the American Chemical Society*, 2014, **136**, 4113-4116.
82. M. Khazaei, M. Arai, T. Sasaki, M. Estili and Y. Sakka, *Physical Chemistry Chemical Physics*, 2014, **16**, 7841-7849.
83. I. R. Shein and A. L. Ivanovskii, *Superlattices and Microstructures*, 2012, **52**, 147-157.
84. A. N. Enyashin and A. L. Ivanovskii, *Journal of Solid State Chemistry*, 2013, **207**, 42-48.
85. S. Wang, J.-X. Li, Y.-L. Du and C. Cui, *Computational Materials Science*, 2014, **83**, 290-293.
86. H. Lashgari, M. R. Abolhassani, A. Boochani, S. M. Elahi and J. Khodadadi, *Solid State Communications*, 2014, **195**, 61-69.
87. D. Er, J. Li, M. Naguib, Y. Gogotsi and V. B. Shenoy, *ACS Applied Materials & Interfaces*, 2014, **6**, 11173-11179.
88. Q. Hu, D. Sun, Q. Wu, H. Wang, L. Wang, B. Liu, A. Zhou and J. He, *The Journal of Physical Chemistry A*, 2013, **117**, 14253-14260.
89. Q. Hu, H. Wang, Q. Wu, X. Ye, A. Zhou, D. Sun, L. Wang, B. Liu and J. He, *International Journal of Hydrogen Energy*, 2014, **39**, 10606-10612.
90. M. Khazaei, M. Arai, T. Sasaki, M. Estili and Y. Sakka, *Science and Technology of Advanced Materials*, 2014, **15**, 014208.
91. M. Kurtoglu, M. Naguib, Y. Gogotsi and M. W. Barsoum, *MRS Communications*, 2012, **2**, 133-137.
92. Y. Lee, S. B. Cho and Y.-C. Chung, *ACS Applied Materials & Interfaces*, 2014, **6**, 14724-14728.
93. S. Zhao, W. Kang and J. Xue, *Applied Physics Letters*, 2014, **104**, 133106.
94. A. N. Enyashin and A. L. Ivanovskii, *The Journal of Physical Chemistry C*, 2013, **117**, 13637-13643.
95. L.-Y. Gan, Y.-J. Zhao, D. Huang and U. Schwingenschlögl, *Physical Review B*, 2013, **87**, 245307.
96. Z. Ma, Z. Hu, X. Zhao, Q. Tang, D. Wu, Z. Zhou and L. Zhang, *The Journal of Physical Chemistry C*, 2014, **118**, 5593-5599.
97. Q. Tang, Z. Zhou and P. Shen, *Journal of the American Chemical Society*, 2012, **134**, 16909-16916.
98. A. N. Enyashin and A. L. Ivanovskii, *Computational and Theoretical Chemistry*, 2012, **989**, 27-32.
99. Y. Xie, Y. Dall'Agnese, M. Naguib, Y. Gogotsi, M. W. Barsoum, H. L. Zhuang and P. R. C. Kent, *ACS Nano*, 2014, **8**, 9606-9615.
100. M. Khazaei, M. Arai, T. Sasaki, C.-Y. Chung, N. S. Venkataramanan, M. Estili, Y. Sakka and Y. Kawazoe, *Advanced Functional Materials*, 2013, **23**, 2185-2192.
101. Y. Xie and P. Kent, *Physical Review B*, 2013, **87**, 235441.
102. Y. Xie, M. Naguib, V. N. Mochalin, M. W. Barsoum, Y. Gogotsi, X. Yu, K.-W. Nam, X.-Q. Yang, A. I. Kolesnikov and P. R. C. Kent, *Journal of the American Chemical Society*, 2014, **136**, 6385-6394.
103. S. Zhao, W. Kang and J. Xue, *The Journal of Physical Chemistry C*, 2014, **118**, 14983-14990.
104. C. Eames and M. S. Islam, *Journal of the American Chemical Society*, 2014, **136**, 16270-16276.
105. G. R. Berdiyorov, *AIP Advances*, 2016, **6**, 055105.
106. P. Srivastava, A. Mishra, H. Mizuseki, K.-R. Lee and A. K. Singh, *ACS Applied Materials & Interfaces*, 2016, DOI: 10.1021/acsami.6b08413.
107. L. H. Karlsson, J. Birch, J. Halim, M. W. Barsoum and P. O. Å. Persson, *Nano Letters*, 2015, **15**, 4955-4960.
108. X. Sang, Y. Xie, M.-W. Lin, M. Alhabeb, K. L. Van Aken, Y. Gogotsi, P. R. C. Kent, K. Xiao and R. R. Unocic, *ACS Nano*, 2016, **10**, 9193-9200.
109. D. Magne, V. Mauchamp, S. Celerier, P. Chartier and T. Cabioc'h, *Physical Chemistry Chemical Physics*, 2016, **18**, 30946-30953.
110. H. Pan, *Journal of Materials Chemistry A*, 2015, **3**, 21486-21493.
111. J. He, P. Lyu and P. Nachtigall, *Journal of Materials Chemistry C*, 2016, DOI: 10.1039/C6TC03917K.
112. L. Hu, X. Wu and J. Yang, *Nanoscale*, 2016, **8**, 12939-12945.
113. Y. Zhou, K. Luo, X. Zha, Z. Liu, X. Bai, Q. Huang, Z. Guo, C.-T. Lin and S. Du, *The Journal of Physical Chemistry C*, 2016, **120**, 17143-17152.
114. S. Zhao, W. Kang and J. Xue, *Journal of Materials Chemistry C*, 2015, **3**, 879-888.
115. X. Zhang, X. Zhao, D. Wu, Y. Jing and Z. Zhou, *Nanoscale*, 2015, **7**, 16020-16025.
116. Z. H. Fu, Q. F. Zhang, D. Legut, C. Si, T. C. Germann, T. Lookman, S. Y. Du, J. S. Francisco and R. F. Zhang, *Physical Review B*, 2016, **94**, 104103.
117. Z. Guo, J. Zhou, C. Si and Z. Sun, *Physical Chemistry Chemical Physics*, 2015, **17**, 15348-15354.
118. C. Xu, L. Wang, Z. Liu, L. Chen, J. Guo, N. Kang, X.-L. Ma, H.-M. Cheng and W. Ren, *Nat Mater*, 2015, **14**, 1135-1141.
119. X.-H. Zha, J. Yin, Y. Zhou, Q. Huang, K. Luo, J. Lang, J. S. Francisco, J. He and S. Du, *The Journal of Physical Chemistry C*, 2016, **120**, 15082-15088.
120. D. Cakr, C. Sevik, O. Gulseren and F. M. Peeters, *Journal of Materials Chemistry A*, 2016, **4**, 6029-6035.
121. M. Ashton, K. Mathew, R. G. Hennig and S. B. Sinnott, *The Journal of Physical Chemistry C*, 2016, **120**, 3550-3556.
122. L. Li, *Computational Materials Science*, 2016, **124**, 8-14.
123. M. Khazaei, A. Ranjbar, M. Arai and S. Yunoki, *Physical Review B*, 2016, **94**, 125152.
124. C. Si, K.-H. Jin, J. Zhou, Z. Sun and F. Liu, *Nano Letters*, 2016, **16**, 6584-6591.

125. B. Anasori, C. Shi, E. J. Moon, Y. Xie, C. A. Voigt, P. R. C. Kent, S. J. May, S. J. L. Billinge, M. W. Barsoum and Y. Gogotsi, *Nanoscale Horizons*, 2016, **1**, 227-234.
126. Y. Lee, Y. Hwang and Y.-C. Chung, *ACS Applied Materials & Interfaces*, 2015, **7**, 7163-7169.
127. X. Zhang, Z. Ma, X. Zhao, Q. Tang and Z. Zhou, *Journal of Materials Chemistry A*, 2015, **3**, 4960-4966.
128. J. Yang, X. Luo, S. Zhang and L. Chen, *Physical Chemistry Chemical Physics*, 2016, **18**, 12914-12919.
129. H.-W. Wang, M. Naguib, K. Page, D. J. Wesolowski and Y. Gogotsi, *Chemistry of Materials*, 2016, **28**, 349-359.
130. J. L. Nina, W. B. Michel and M. R. James, *EPL (Europhysics Letters)*, 2013, **101**, 57004.
131. A. Yadav, A. Dashora, N. Patel, A. Miotello, M. Press and D. C. Kothari, *Applied Surface Science*, 2016, **389**, 88-95.
132. L. M. Azofra, N. Li, D. R. MacFarlane and C. Sun, *Energy & Environmental Science*, 2016, **9**, 2545-2549.
133. Y. Gao, L. Wang, Z. Li, A. Zhou, Q. Hu and X. Cao, *Solid State Sciences*, 2014, **35**, 62-65.
134. J. Yang, B. Chen, H. Song, H. Tang and C. Li, *Crystal Research and Technology*, 2014, **49**, 926-932.
135. X. Zhang, M. Xue, X. Yang, Z. Wang, G. Luo, Z. Huang, X. Sui and C. Li, *RSC Advances*, 2015, **5**, 2762-2767.
136. H. Zhang, L. Wang, Q. Chen, P. Li, A. Zhou, X. Cao and Q. Hu, *Materials & Design*, 2016, **92**, 682-689.
137. A. D. Dillon, M. J. Ghidiu, A. L. Krick, J. Griggs, S. J. May, Y. Gogotsi, M. W. Barsoum and A. T. Fafarman, *Advanced Functional Materials*, 2016, **26**, 4162-4168.
138. K. Hantanasirisakul, M.-Q. Zhao, P. Urbankowski, J. Halim, B. Anasori, S. Kota, C. E. Ren, M. W. Barsoum and Y. Gogotsi, *Advanced Electronic Materials*, 2016, **2**, 1600050-n/a.
139. M. Mariano, O. Mashtalir, F. Q. Antonio, W.-H. Ryu, B. Deng, F. Xia, Y. Gogotsi and A. D. Taylor, *Nanoscale*, 2016, DOI: 10.1039/C6NR03682A.
140. A. Ali, A. Belaidi, S. Ali, M. I. Helal and K. A. Mahmoud, *Journal of Materials Science: Materials in Electronics*, 2016, **27**, 5440-5445.
141. T. Hu, H. Zhang, J. Wang, Z. Li, M. Hu, J. Tan, P. Hou, F. Li and X. Wang, *Scientific Reports*, 2015, **5**, 16329.
142. J. Guo, Q. Peng, H. Fu, G. Zou and Q. Zhang, *The Journal of Physical Chemistry C*, 2015, **119**, 20923-20930.
143. Y. Ying, Y. Liu, X. Wang, Y. Mao, W. Cao, P. Hu and X. Peng, *ACS Applied Materials & Interfaces*, 2015, **7**, 1795-1803.
144. L. Wang, L. Yuan, K. Chen, Y. Zhang, Q. Deng, S. Du, Q. Huang, L. Zheng, J. Zhang, Z. Chai, M. W. Barsoum, X. Wang and W. Shi, *ACS Applied Materials & Interfaces*, 2016, **8**, 16396-16403.
145. C. E. Ren, K. B. Hatzell, M. Alhabeb, Z. Ling, K. A. Mahmoud and Y. Gogotsi, *The Journal of Physical Chemistry Letters*, 2015, **6**, 4026-4031.
146. G. R. Berdiyorov, M. E. Madjet and K. A. Mahmoud, *Applied Physics Letters*, 2016, **108**, 113110.
147. K. Rasool, M. Helal, A. Ali, C. E. Ren, Y. Gogotsi and K. A. Mahmoud, *ACS Nano*, 2016, **10**, 3674-3684.
148. K. C. Smith and R. Dmello, *Journal of The Electrochemical Society*, 2016, **163**, A530-A539.
149. P. Srimuk, F. Kaasik, B. Kruner, A. Tolosa, S. Fleischmann, N. Jackel, M. C. Tekeli, M. Suss, M. Aslan and V. Presser, *Journal of Materials Chemistry A*, 2016, DOI: 10.1039/C6TA07833H.
150. Y. Qing, W. Zhou, F. Luo and D. Zhu, *Ceramics International*, 2016, **42**, 16412-16416. View Article Online DOI: 10.1039/C6TA06772G
151. M. Han, X. Yin, H. Wu, Z. Hou, C. Song, X. Li, L. Zhang and L. Cheng, *ACS Applied Materials & Interfaces*, 2016, **8**, 21011-21019.
152. M. D. Levi, M. R. Lukatskaya, S. Sigalov, M. Beidaghi, N. Shpigel, L. Daikhin, D. Aurbach, M. W. Barsoum and Y. Gogotsi, *Advanced Energy Materials*, 2015, **5**.
153. M. Ashton, R. G. Hennig and S. B. Sinnott, *Applied Physics Letters*, 2016, **108**, 023901.
154. M. Naguib, J. Come, B. Dyatkin, V. Presser, P.-L. Taberna, P. Simon, M. W. Barsoum and Y. Gogotsi, *Electrochemistry Communications*, 2012, **16**, 61-64.
155. H. Zhang, H. Dong, X. Zhang, Y. Xu and J. Fransaer, *Electrochimica Acta*, 2016, **202**, 24-31.
156. S. J. Kim, M. Naguib, M. Zhao, C. Zhang, H.-T. Jung, M. W. Barsoum and Y. Gogotsi, *Electrochimica Acta*, 2015, **163**, 246-251.
157. M.-Q. Zhao, M. Torelli, C. E. Ren, M. Ghidiu, Z. Ling, B. Anasori, M. W. Barsoum and Y. Gogotsi, *Nano Energy*, 2016, **30**, 603-613.
158. A. Byeon, A. M. Glushenkov, B. Anasori, P. Urbankowski, J. Li, B. W. Byles, B. Blake, K. L. Van Aken, S. Kota, E. Pomerantseva, J. W. Lee, Y. Chen and Y. Gogotsi, *Journal of Power Sources*, 2016, **326**, 686-694.
159. M. R. Lukatskaya, S.-M. Bak, X. Yu, X.-Q. Yang, M. W. Barsoum and Y. Gogotsi, *Advanced Energy Materials*, 2015, **5**, 1500589-n/a.
160. K. Xu, X. Ji, B. Zhang, C. Chen, Y. Ruan, L. Miao and J. Jiang, *Electrochimica Acta*, 2016, **196**, 75-83.
161. M. Hu, Z. Li, H. Zhang, T. Hu, C. Zhang, Z. Wu and X. Wang, *Chemical Communications*, 2015, **51**, 13531-13533.
162. M. Zhu, Y. Huang, Q. Deng, J. Zhou, Z. Pei, Q. Xue, Y. Huang, Z. Wang, H. Li, Q. Huang and C. Zhi, *Advanced Energy Materials*, 2016, **6**, 1600969-n/a.
163. Z. Lin, D. Barbara, P.-L. Taberna, K. L. Van Aken, B. Anasori, Y. Gogotsi and P. Simon, *Journal of Power Sources*, 2016, **326**, 575-579.
164. Y. Dall'Agnese, P. Rozier, P.-L. Taberna, Y. Gogotsi and P. Simon, *Journal of Power Sources*, 2016, **306**, 510-515.
165. P. Yan, R. Zhang, J. Jia, C. Wu, A. Zhou, J. Xu and X. Zhang, *Journal of Power Sources*, 2015, **284**, 38-43.
166. R. B. Rakhi, B. Ahmed, D. Anjum and H. N. Alshareef, *ACS Applied Materials & Interfaces*, 2016, **8**, 18806-18814.
167. Y. Tang, J. Zhu, C. Yang and F. Wang, *Journal of Alloys and Compounds*, 2016, **685**, 194-201.
168. Y. Wang, H. Dou, J. Wang, B. Ding, Y. Xu, Z. Chang and X. Hao, *Journal of Power Sources*, 2016, **327**, 221-228.
169. Y.-Y. Peng, B. Akuzum, N. Kurra, M.-Q. Zhao, M. Alhabeb, B. Anasori, E. C. Kumbur, H. N. Alshareef, M.-D. Ger and Y. Gogotsi, *Energy & Environmental Science*, 2016, **9**, 2847-2854.
170. N. Kurra, B. Ahmed, Y. Gogotsi and H. N. Alshareef, *Advanced Energy Materials*, 2016, DOI: 10.1002/aenm.201601372, n/a-n/a.
171. H. Li, Y. Hou, F. Wang, M. R. Lohe, X. Zhuang, L. Niu and X. Feng, *Advanced Energy Materials*, 2016, DOI: 10.1002/aenm.201601847, 1601847-n/a.
172. E. Yang, H. Ji, J. Kim, H. Kim and Y. Jung, *Physical Chemistry Chemical Physics*, 2015, **17**, 5000-5005.
173. Y.-X. Yu, *The Journal of Physical Chemistry C*, 2016, **120**, 5288-5296.

View Article Online
DOI: 10.1039/C6TA06772G

174. X. Wang, X. Shen, Y. Gao, Z. Wang, R. Yu and L. Chen, *Journal of the American Chemical Society*, 2015, **137**, 2715-2721.
175. S. Kajiyama, L. Szabova, K. Sodeyama, H. Iinuma, R. Morita, K. Gotoh, Y. Tateyama, M. Okubo and A. Yamada, *ACS Nano*, 2016, **10**, 3334-3341.
176. Y. Dall'Agnese, P.-L. Taberna, Y. Gogotsi and P. Simon, *The Journal of Physical Chemistry Letters*, 2015, **6**, 2305-2309.
177. X. Zhao, M. Liu, Y. Chen, B. Hou, N. Zhang, B. Chen, N. Yang, K. Chen, J. Li and L. An, *Journal of Materials Chemistry A*, 2015, **3**, 7870-7876.
178. X. Liang, A. Garsuch and L. F. Nazar, *Angewandte Chemie International Edition*, 2015, **54**, 3907-3911.
179. C. Lin, W. Zhang, L. Wang, Z. Wang, W. Zhao, W. Duan, Z. Zhao, B. Liu and J. Jin, *Journal of Materials Chemistry A*, 2016, **4**, 5993-5998.
180. W. Bao, D. Su, W. Zhang, X. Guo and G. Wang, *Advanced Functional Materials*, DOI: 10.1002/adfm.201603704, n/a-n/a.
181. Z. W. Seh, K. D. Fredrickson, B. Anasori, J. Kibsgaard, A. L. Strickler, M. R. Lukatskaya, Y. Gogotsi, T. F. Jaramillo and A. Vojvodic, *ACS Energy Letters*, 2016, **1**, 589-594.
182. C. Ling, L. Shi, Y. Ouyang, Q. Chen and J. Wang, *Advanced Science*, 2016, **3**, 1600180-n/a.
183. Z. Guo, J. Zhou, L. Zhu and Z. Sun, *Journal of Materials Chemistry A*, 2016, **4**, 11446-11452.
184. X. Xie, S. Chen, W. Ding, Y. Nie and Z. Wei, *Chemical Communications*, 2013, **49**, 10112-10114.